

# DFT modelling of oxide materials for hydrogen permeable membranes

**Bork, Nicolai Christian**

*Publication date:*
2010

*Document Version*
Publisher's PDF, also known as Version of record

Ph.D. thesis

# DFT modelling of oxide materials for hydrogen permeable membranes

by Nicolai Bork

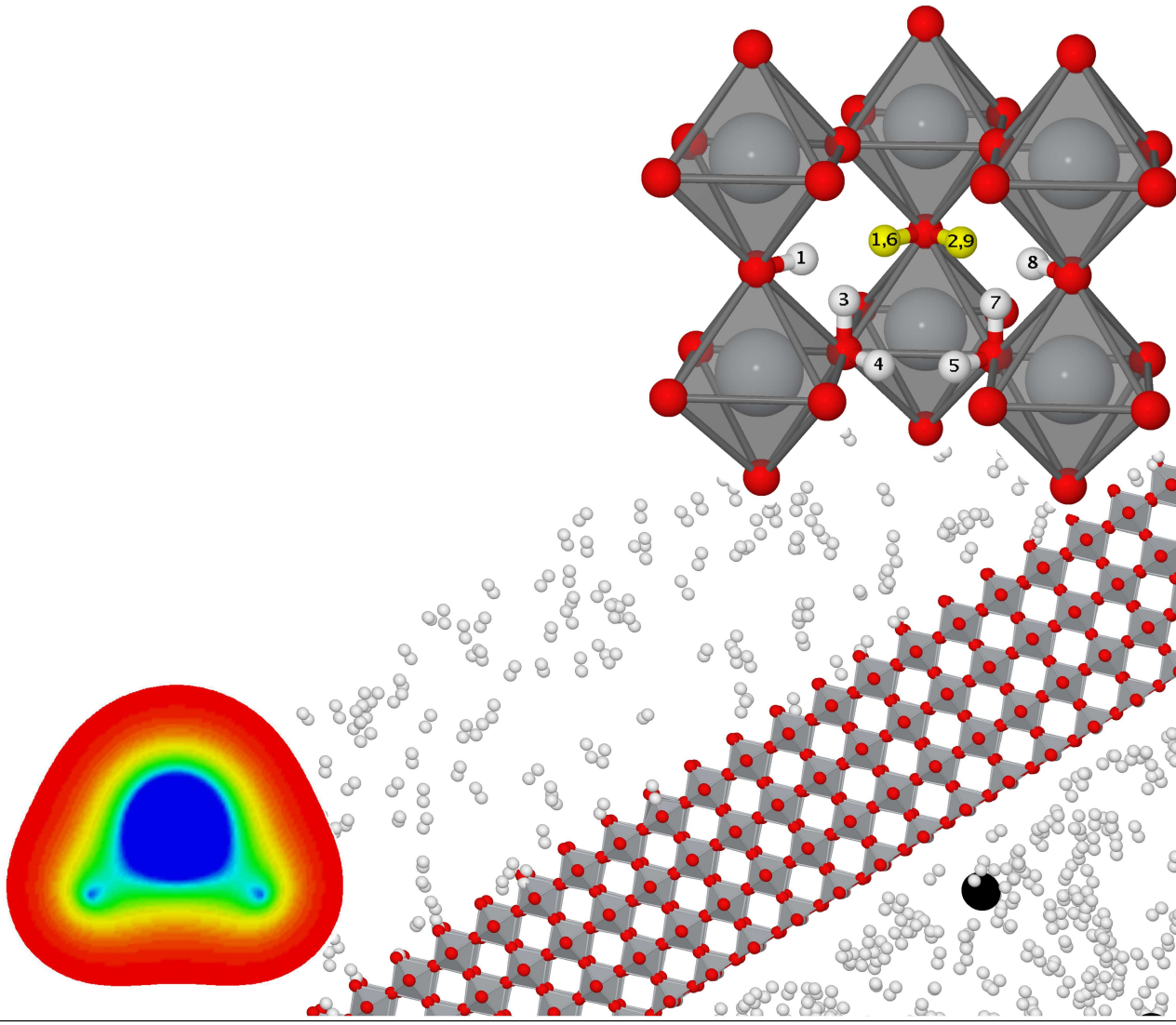


**September 2010**

Technical University of Denmark

Risø DTU
National Laboratory for Sustainable Energy

# Contents

## 0.1 Preface

This thesis is submitted in candidacy for the Ph.D. degree from the Technical University of Denmark (DTU). The work has been carried out at the Fuel Cells and Solid State Chemistry Division at the National Laboratory for Sustainable Energy, Risø DTU and at the Center for Atomic-scale Materials Design (CAMD) at the Department of Physics, DTU.

The work has been supervised by Ph.D. Senior Scientist Tejs Vegge and Senior Scientist Nikolaos Bonanos at Risø DTU and by Ph.D. Associate Professor Jan Rossmeisl at CAMD and has been funded by Risø DTU as part of the "Initiative for Hydrogen Permeable Membranes."

The results presented would not have been achieved without the help and assistance of numerous friends and colleagues. I would mainly thank all of my supervisors for their help and support, especially my main supervisor Tejs Vegge has provided vital guidance and inspiration.

Further I would like to thank Henrik Bentzer for numerous scientific discussions on the field of solid state chemistry. I hope that you have benefited as much as I.

I would also like to thank all the members of the Energy Storage Group at Risø DTU. Special thanks to Johannes Voss, Adem Tekin, Jens S. Hummelshøj and Nonni Bergmann. I would also like to thank F.W. Poulsen, Mogens Mogensen, Federico C. Vallejo, Karinh Eurenius, Rolf Berg and Jean Claude Grivel for fruitful scientific discussions and assistance.

I would finally like to thank Professor Hannes Jónsson from the University of Reykjavik, Iceland for assistance during my stay.

## 0.2 Abstract

The current focus on renewable energy systems has increased research in proton conducting membranes. The most promising applications include electrolyte in proton conducting solid oxide fuel cells and hydrogen gas separation membranes. Despite much research, no oxide based proton conductor has been introduced commercially mainly due to too low protonic fluxes. We have utilized the explicit atomic modelling in density functional theory (DFT) to develop new methods for intelligent and selective materials design and to investigate fundamental properties of hydrogen in oxides.

Motivated by a successful trend study targeting materials for hydrogen storage we have screened a number of perovskites and have found a strong correlation between mobility and concentration of the OH defect. Utilizing this correlation we demonstrate the possibility of suggesting dopant and dopant concentration for a given material for the best possible trade-off between hydrogenic mobility and concentration. We predict good diffusion properties for the mixed perovskite $Sr_{0.5}Ca_{0.5}TiO_3$.

Further, we have studied the interaction between various defects, most importantly two H defects. We find that elastic lattice interactions stabilize the double H defect which we demonstrate contribute significantly to the hydrogen flux at typical membrane working conditions.

Another study yielded excellent agreement between experimental end theoretical results enabling a precise description of the atomic configurations found in Ca doped $Sm_2Sn_2O_7$ again by utilizing interactions between the various defects.

Finally, we investigated the charge distribution and atomic charges of a series of hydrogenated oxides. We found the H species partially charged by ca. $+0.5\ e$ when bound to an oxygen as $OH_O$. This is contrary to the general referring to the dissolved H species as a proton. It is more in accordance with an effective H charge of ca. $0.25\ e$ found in the double H system. An $H_O$ species was however found in $Sm_2Sn_2O_7$ charged by ca. $-0.45\ e$. This may help to explain recent experimental finding suggesting hydride diffusion at elevated temperatures.

The presented results contibute significantly towards a more detailed understanding of and control over the various defects and defect interactions relevant for proton conducting membranes.

## 0.3 Dansk resumé

Den nuværende fokus på vedvarende energisystemer har afstedkommet forøget forskning i protonledende membraner til brug som enten elektrolytter i brændselsceller eller som membranmateriale til oprensning af hydrogen gas. På trods af megen forskning er ingen oxid baseret protonleder blevet introduceret kommercielt, hovedsageligt på grund af for lave protoniske fluxe.

Vi har benyttet den eksplicitte atomare modellering i tæthedsfunktional teori til udvikling af nye metoder til intelligent og selektivt materialedesign samt til at undersøge fundamentale egenskaber for hydrogen i oxider.

Motiveret af et succesfuldt trendstudie målrettet materialer til hydrogenlagring har vi screenet et antal perovskiter og fundet en stærk korrelation mellem mobilitet og koncentration af OH defekten. Ved at bruge denne korrelation har vi demonstreret muligheden for at forudsige egnede dopant og dopant koncentration for et givent materiale for at opnå den bedst mulige opvejning af hydrogenisk mobilitet og koncentration. Vi forudsiger gode diffusions egenskber for den blandede perovskit $Sr_{0.5}Ca_{0.5}TiO_3$.

Ydermere har vi studeret interaktionen mellem forskellige defekter, mest omfattende mellem to H defekter. I modsætning til tidligere antagelser finder vi at elastisk gitter interaktion stabiliserer dobbel H defekten. Vi demonstrerer at denne defekt vil bidrage betydeligt til den totale hydrogen flux under typiske applikations betingelser.

Et andet studie gav fremragende overensstemmelse mellem eksperimentelle og teoretiske resultater, hvilket muliggjorde en præcis beskrivelse af den atomare konfiguration i Ca dopet $Sm_2Sn_2O_7$.

Endeligt undersøgte vi ladningsfordelingen og de atomare ladninger i en serie af hydrogenerede perovskiter. Vi fandt H defekten delvist ladet med ca. $+0.5\ e$ hvis bundet til et oxygen som $OH_O$. Dette i modsætning til den generelle reference til den absorberede H specie som en proton, men mere på linje med en effektiv H ladning på ca. $0.25\ e$ fundet i dobbel H systemet. En $H_O$ specie blev dog fundet i $Sm_2Sn_2O_7$ ladet med ca. -0.45 $e$. Denne kan hjælpe med at forklare nylige eksperimentelle resultater der antyder hydrid diffusion ved høje temperaturer.

De præsenterede resultater udgør et betydeligt bidrag mod en mere detaljeret forstelse af og kontrol over de forskellige defekter og defekt interaktioner relevanter for proton ledende membramer.

# Chapter 1

# Introduction

## 1.1 Motivation

The demand for energy is continuously increasing all over the world and for a long time, energy has been a major political concern. Energy consumption is arguably a prerequisite for securing a high standard of living as seen from Figure 1.1 and even though some countries use energy more efficiently than others, no countries at the top of the human development index are using less than ca. 4 MWh per capita per year. Due to the rapid development of many second world countries, most noticeably India and China,[1] energy consumption will inevitably continue to grow as more and more people are getting access to electricity and motorized transportation. Hereby the living standards of hundreds of millions of people are being drastically improved by a, per capita, modest increase of energy consumption.

The effect on many global systems will nevertheless inevitably be drastic and research into energy technologies, which may reduce the negative effects of the increased energy consumption, is therefore of great interest. In the industrialized world the main motivations for conducting energy related research are related to two such subjects, namely energy stability and climate changes.

### Energy Stability

The concern over energy stability has both global and national aspects. For decades the so called "peak oil" situation has been feared [3, 4] where the global oil production begins to decline despite rising demands. Forecasting

[1] 2009 growth rates: China: 8.7 %. India: 6.5 %.

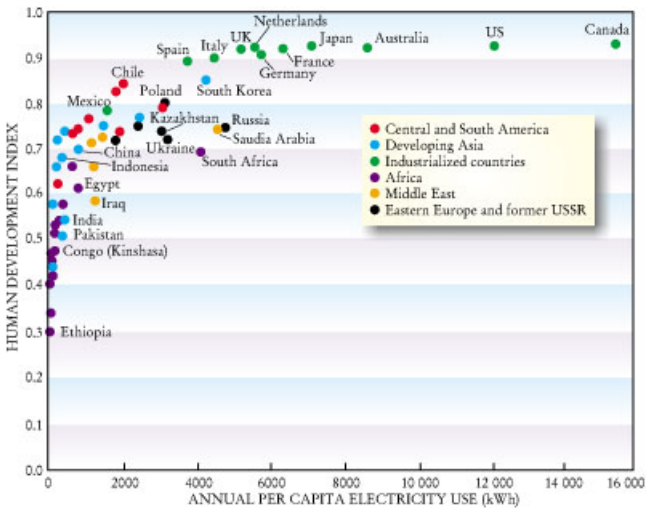


Figure 1.1: *Energy vs. human development index, a measure of well-being used by the United Nations. Energy is identified as a prerequisite for human development and demands are expected to increase as more countries develop. Figure adopted from Benka.*[1, 2]

peak oil is extremely difficult (see Figure 1.2) and undoubtedly subject to political bias, but should oil production peak in the near future serious conflicts will be a likely consequence. Although other non-renewable energy sources such as coal and uranium may not be immediately depletable,[2] the lack of readily available liquid fuels will have a significant impact on the energy price.

Also at national level energy stability is a concern. Countries without natural energy resources are forced to import energy with significant economic consequences. Such countries are also vulnerable to political and economical pressure from the suppliers e.g. seen during the 1970's energy crisis and more recent in eastern Europe - clearly an undesirable situation for any nation.

### Climate Change

Climate changes are presently one of the most debated subjects both in the scientific literature and in the media, since global warming is seen as a great threat to the ecosystems and economic stability or the world.[6]

[2]Estimated depletion times.[5] Coal : 200 years. Uranium: 50 years.

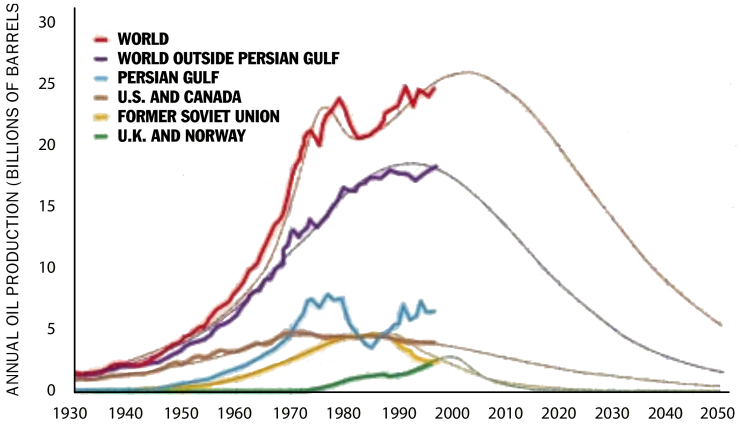


Figure 1.2: *The original predictions of the oil production rate by Campbell and Laherrere demonstrating the predicted Gaussian form of the energy production curve.*[4]

Recently, the average global temperature seemed to have risen by ca. 0.1 °C pr decade (see Figure 1.3) and even though the climate system is enormously complicated, most attention has been directed towards anthropogenic forcings mainly from $CO_2$ emissions. To prevent further $CO_2$ emissions, the heavy dependence on fossil fuels must be broken and the entire energy sector must be renewed.

## 1.2 The hydrogen economy

As fossil fuels have proven problematic, alternative energy sources have gained popularity. Renewable energy sources including wind, wave and solar energy are obvious candidates since the annual amount of solar energy hitting the Earth, ca. $4\times10^{24}$ J, is vastly higher than the annual energy consumption, ca. $5\times10^{20}$ J. However, the low energy density makes utilization difficult and renewable energy is currently 2-10 times more expensive than fossil energy.[7] One of the most significant problems is how to store the produced electrical energy.[8] Since batteries are both expensive and short-lived,[9] hydrogen has been proposed as the main energy carrier in a fossil fuel free society.[10]

Hydrogen may be produced using various methods depending on the energy source. If electrical, the most obvious choice it through electrolysis

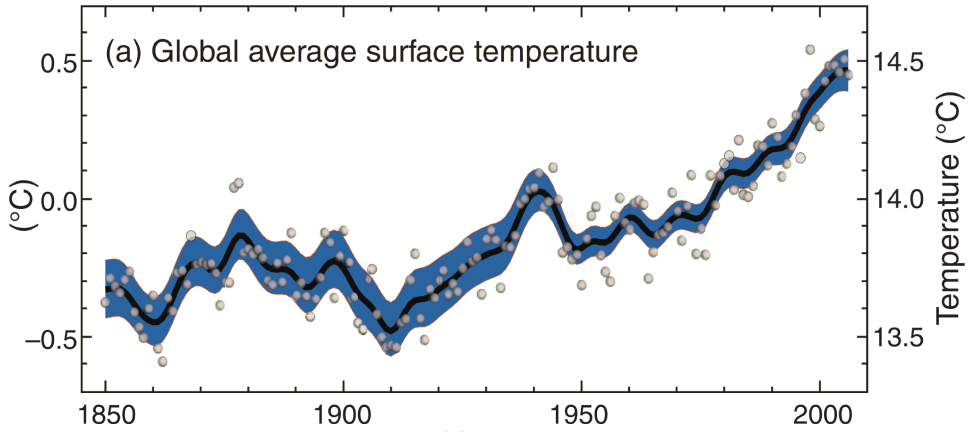


Figure 1.3: *Development of global mean temperature in the last 150 years [6] showing an increase of mean temperature of ca. 0.1 °C pr. decade.*

of water since this carbon free hydrogen source is cheap and readily available. A significant amount of research is directed at optimizing this process through development of catalysts.

If renewable energy is unavailable in sufficient amounts, hydrogens may be synthesised from coal or biomass through gassification[11] and/or the water-gas shift reaction;[12]

$$\mathrm{C} + \mathrm{H_2O} \rightarrow \mathrm{CO} + \mathrm{H_2} \tag{1.1}$$

$$\mathrm{CO} + \mathrm{H_2O} \rightarrow \mathrm{CO_2} + \mathrm{H_2}. \tag{1.2}$$

The produced $CO_2$ may be captured and stored[13] or used to resynthesize hydrocarbons.[14, 15] Even though hydrogen produced via fossil fuels might not be $CO_2$ neutral, this may an important intermediate hydrogen production path since a complete shift to renewables may be impractical.

## 1.3 Fuel cells

The produced hydrogen may be refined further to liquid fuels, e.g. ethanol or dimethyl ether[14, 15] or used as a fuel by itself. At standard temperature and pressure the energy density of gaseous hydrogen is very low[3] and hence impractical e.g. for transportation purposes. Pressurizing or

[3]Hydrogen gas: 0.01079 MJ/l. Gasoline: 34.2 MJ/l.

liquefying molecular hydrogen is both expensive and pose potential safety hazards, and although energy densities up to 10 MJ/l can be reached, the large containing systems prevent these storage methods from fulfilling DOE requirements.[4][16]

In stead it may be advantageous to store the hydrogen as a complex salt, e.g. amonia ($Mg(NH_4)_6Cl_2$) or borohydride ($MgBH_4$), but developing a recyclable material with fast kinetics and suitable temperature range for absorption and desorption (50-150 °C) has proven difficult.[17] However stored, hydrogen may be used in a conventional combustion engine, but due to the low energy efficiencies of these, more attention is given to fuel cell based applications.

Various types of fuel cells exist with different advantages and disadvantages. The polymer based proton exchange fuel cells (PEM) have been used for decades in specialized applications including spacecrafts and submarines, but more recently the usability has been demonstrated in a variety of automotive and stationary applications.[18] Most PEM fuel cells are designed around a Nafion electrolyte[19] and display efficiencies up to 60 %, but deteriorate above 100 °C and the internal disposal of liquid water is a problem.

While maintaining a high fuel efficiency, oxide ion conducting solid oxide fuel cells (SOFC's) accept a large variety of fuels including hydrogen, ammonia and liquid hydrocarbons, and operate at much higher temperatures (500-800 °C) whereby liquid water formation is avoided.[20, 21] Oxide ion conducting SOFC's do, however, have inherent disadvantages from fuel dilution with water and other combustion products with decreased efficiently as consequence. Mixing fuel and combunstion products ($CO_2$ and $H_2O$) typically lead to a ca. 200-400 mV drop in Nernst voltage and a corresponding loss of efficiently. Further, the high temperatures required prevent small scale utilization such as personal transportation. The first industrial scale SOFC production was opened in 2009 in Lyngby, Denmark.[5]

The proton conducting SOFC's are conceptually superior to the oxide ion conducting SOFC due to the separation of fuel and oxidation products, while the advantages of high operation temperatures are maintained.[22] A schematic illustration of a proton conducting fuel cell and electrolysis cell is shown in Figure 1.4. These are still not commercially competitive due to the poor flux properties.[23, 24]

[4] United States Department of Energy

[5] See also www.topsoefuelcell.com

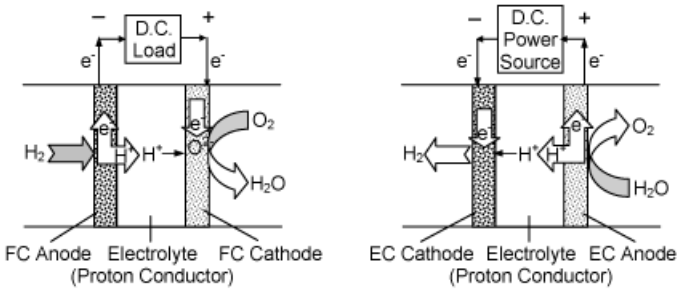


**(a)** Fuel cell mode **(b)** Electrolysis cell mode

Figure 1.4: *Schematic illustration of a proton conducting fuel cell and a proton conducting electrolysis cell. A given system performing well in one mode will often perform well in the other due to the reverse, but otherwise identical processes.[25]*

## 1.4 Gas separation membranes

In most proposed systems a purification of the produced hydrogen gas is necessary as this may be heavily polluted e.g. by CO, $CO_2$, $NO_x$ and $SO_x$. Several technologies for hydrogen gas separation membranes are currently under consideration (see Table 1.1), but since the produced hydrogen is intended for fuel cells, the dense membrane technologies are receiving most attention as the purified hydrogen gas is virtually pollutant free. This is vital since pollutants, especially $SO_x$ and to lesser degree $NO_x$, deteriorate most fuel cells hereby reducing both lifetime and performance.[26] Other methods for separation are possible, but membranes have significant advantages in terms of simplicity, operating continuity and efficiency.[27]

Both metallic and solid oxide membranes are possible, but the metallic based membranes are currently superior with respect to operating temperature and hydrogen flux. The best metallic membranes are however all based on rare and expensive metals e.g. palladium and silver and thus very expensive. Current palladium prices are in excess of 500 $ per ounce. Attention has therefore been drawn to solid oxides, though not as efficient as metallic membranes, being significantly cheaper. See Ockwig and Nenoff[28] or Adhikari and Fernando[29] for extensive reviews.

The main motivation for conducting research into hydrogen gas separation membranes is targeting the renewable energy sector, but other niche applications are possible such as an electrochemical sensoring of hydrogen and water or possible usage for H/D/T isotope separation,[30] e.g. for fuel

Table 1.1: *Overview of possible materials for hydrogen gas separation membranes. †: $10^{-3} mol/m^2 s$ at dP=1 bar. From Kluiters [27].*

| | Micro Porous Ceramics | Dense Metallic | Porous Carbon | Dense Ceramics |
|---|---|---|---|---|
| T (°C) | 200-600 | 300-600 | 500-900 | 600-900 |
| $H_2$ selectivity | 5-139 | >1000 | 4-20 | >1000 |
| $H_2$ flux† | 60-300 | 60-300 | 10-200 | 6-80 |
| Stability | Poor stability in $H_2O$ | Phase transition | Brittle oxidising | Stability in $CO_2$ |
| Poisoning | | $H_2S$, HCl CO | Strong adsorbing vapours | $H_2S$ |
| Materials | Simple oxides Zeolites | Palladium alloys | Carbon | Perovskites, Phosphates |

in fusion power plants.

The main hindrance for application of solid oxide hydrogen separation membranes is the low flux through the membrane. Even at large pressure differences, high temperatures and optimized membrane geometries, the best fluxes of today are significantly lower than required for industrial utilization.[6]

The overlap between research in materials for solid oxide hydrogen gas permeable membranes and proton conducting SOFC's is large, due to the many similarities e.g. with respect to operating temperatures, poisoning issues, cost efficiency and diffusion mechanism. The main difference is the electronic conductivity properties; an electronic conductor is required for gas separation whereas an electronic insulator is required in a fuel cell electrolyte.

The research presented in this thesis was originally targeting gas separation membranes, but since methods for electronic transport calculations have been unavailable most attention have been given to ionic transport mechanisms and ionic relations. Most results are therefore relevant for either applications.

[6] See however www.hysep.com for commercialized metallic membranes for hydrogen gas separation.

## 1.5 Thesis outline

The articles and results constituting this thesis are based on theoretical investigations of defect chemistry in solid oxides with strong emphasis on hydrogen. Primarily perovskite structured oxides, $ABO_3$, have been investigated as these are particularly well suited for the applied theoretical methods, but also because several perovskites are amongst the best candidates for an applied solid oxide proton conductor due to reasonable stability and flux properties.

In Chapter 2 the current knowledge and perceptions about hydrogen in solid oxides will be outlined. An introduction to the Kröger-Vink notation used throughout the thesis and the articles is also given.

In Chapter 3 follows a description of the theoretical models used. First, a general introduction to quantum mechanics, whereafter the Born-Oppenheimer approximation and the force theorem are presented. An introduction to density functional theory (DFT) follows, shortly outlining the theoretical basis and the Kohn-Sham method. The exchange-correlation functionals and software packages used are finally described. Temperature is included in the models using statistical mechanics. Based on DFT calculations, methods for determining entropic effects, vibrational frequencies, and reaction paths are presented. Finally, the Bader charge analysis method is outlined.

The main results are presented in Chapters 4 to 6 and discussed with reference to each other. These chapters are not intended to give in-depth presentations of the results. Detailed explanation of motivations, methods, results and conclusions for each subject is given in the 5 appended articles.

In Chapter 4, two screening studies aimed at thermodynamic and kinetic properties are presented. The first study demonstrates the usability of template models and structures to describe general trends. This is utilized and confirmed in the second study where kinetic properties are included. From these results we suggest a suitable candidate material with optimum tradeoff between mobility and concentration of the OH defect.

In Chapter 5, studies on defect-defect interactions are presented. Initially results for hydrogen-hydrogen interactions in oxides are presented, where a net attraction between two hydrogens is found and the mobility and expected lifetime of the novel double H defect is determined. Further, studies on defect interactions of hydrogenated Ca doped $Sm_2Sn_2O_7$ are presented.

Finally in Chapter 6, the results concerning the Bader charge analysis are presented. An approximately 0.50 $e$ OH charge is found which is con-

firmed in all investigated systems including perovskites, pyrochlores and molecules and in a variety of double defect systems. The $H_O$ defect is also investigated where a charge of -0.44 $e$ is found. This importance of this "hydride" is discussed.

The presented results are finally summarized and a short outlook is presented in Chapter 7 where further research topics are suggested. These include electronic transport mechanisms, the double hydrogen defect and the nature of the $H_O$ defect.

# Chapter 2

# Hydrogen in solid oxides

## 2.1 General defect chemistry

During the 20'th century it was discovered that stoichiometric imperfections in crystalline solids were the rule rather than the exception and that a variety of important solid state phenomena were caused or mediated by lattice defects.[31, 32] These include corrosion, fracturing, and solid state diffusion to name just a few.[31, 33, 34] Dependent on a range of conditions lattice imperfections may be present in a large range of concentrations and are thermodynamically favoured relative to the corresponding defect free lattice due to entropy.[35]

At non-zero temperatures, defects are continuously created and annihilated either due to internal disordering of lattice atoms or due to interaction with a surrounding gas or liquid, or another solid phase. Defects may be mono- or polyatomic ranging from vacancies and defect pairs over dislocation defects to grain boundaries including thousands of atoms. Even electrons and holes may be considered as part of the defect structure.

Since defects are mobile and will diffuse through the lattice, chemical equilibrium can often be assumed. Experiments involving heating and cooling may however induce frozen-in out-of-equilibrium distributions which may be important to consider as well.[36, 37, 38]. Assuming equilibrium, the general laws of thermodynamics may be applied enabling the defect chemist to obtain insight based on well known and simple relations; most importantly the law of mass action and the principle of electroneutrality. The law of mass action is given as

$$\frac{\prod a_P}{\prod a_R} = \exp\left(-\frac{\Delta \mathrm{G}}{k_B \mathrm{T}}\right) \tag{2.1}$$

where $a_P$ and $a_R$ are the chemical activities of products and reactants, $\Delta$G is Gibbs free energy and $k_B$ is Boltzmanns constant. The electroneutrality condition is given as

$$\sum z_i c_i = 0 \tag{2.2}$$

where $z_i$ and $c_i$ denote charge and concentration of the i'th species.

Even though the crystalline environment is both dynamic and defective, it is often useful to keep reference to the crystal structure in terms of atomic sites. These may be occupied by an alien atom thereby constituting a substitutional defect or the site may be unoccupied thereby constituting a vacancy. Atoms may also find stable sites not described by the reference lattice. These sites are termed interstitials. Keeping track of the concentrations of structural atoms and defects at varying conditions is the purpose of defect chemistry and to achieve this a suitable system of notation is required.

### 2.1.1 Kröger-Vink notation

Since the chemistry of solids is subject to the same thermodynamic laws as all other branches of chemistry, it may be abstracted by the same symbols and equations as conventional chemistry, but it is often useful to apply a different notation. Most popular is the Kröger-Vink notation[39] which differ from standard chemical notation in three ways;

1. The specific atomic site is appended to the atomic symbol as subscript. A normal atom, $A$, is denoted $A_A$ whereas a substitutional $B$ atom on an A site is denoted $B_A$. An interstitial $A$ atom is denoted $A_i$.

2. Even though all concentrations may be handled using the actual atoms, it is useful to handle the vacancy more explicitly. This defect is denoted v (or V) and is treated as any other element. It may be electrically charged and its concentration may be obtained via the law of mass action and electroneutrality condition.

3. It is often important to keep track of the involved charges which is readily done by using absolute charges. However, also here it is practical to keep the notation as simple as possible and in stead consider changes from ideality. A charge identical to the reference is denoted superscript $x$ while positive and negative charges are denoted by $\bullet$ and $'$, respectively. A structural $A$ atom is thus denoted $A_A^x$ while a

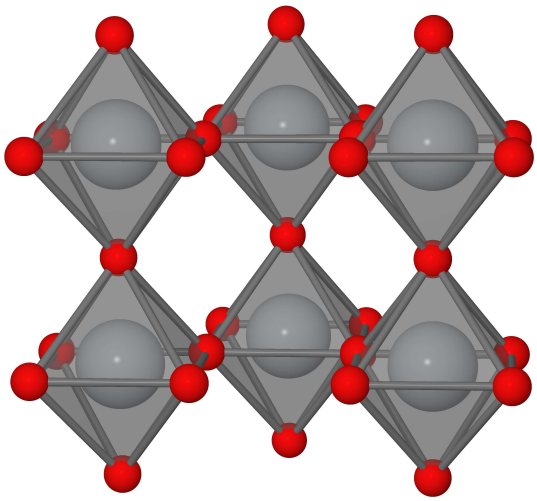

Figure 2.1: *Illustration of the perovskite structure ($ABO_3$). Here, a simple cubic structure is shown, but tetragonal and orthorhombic structures are also common. Grey spheres represent B cations, red spheres represent oxygen atoms while A cations, located in the voids between the octahedra, are omitted for clarity.*

substitutional $B$ atom, if negatively charged compared to the A atom, is denoted $B'_A$.

In this thesis, the hydrogen defect is of special interest. Most often the hydrogen is found bound to a lattice oxygen atom with a bond length close to 1 Å. Even though this strictly is an interstitial site, the term $H_i$ is seldom used. In stead the implicit notation $OH_O$ is most often seen.

As long as the host crystal structure are unchanged by the processes of interest, Kröger-Vink notation is an elegant and intuitive notation. If the material undergoes phase transitions, crystal growth, creep or if the phase is disordered, care should be taken and normal notation may be more advantageous. In the present thesis, these situations are without relevance and Kröger-Vink notation will be applied throughout.

## 2.2 The perovskite structure

As the main work presented in this thesis is performed on perovskite systems, a brief introduction is appropriate.

A material is termed a "perovskite" when it adopts the same general structure as the mineral perovskite ($CaTiO_3$). Oxidic perovskites all adopt the general structure $ABO_3$ where $A$ and $B$ are metals. The smaller $B$ cation is octahedrally coordinated by oxygen and the larger $A$ cations are located between the octahedra. Often found oxidation numbers include $A^{+2}B^{+4}O_3$ and $A^{+3}B^{+3}O_3$. The structure is often cubic with only one chemical unit in the unit cell although larger distorted unit cells, e.g. orthorhombic or tetragonal, also are frequent. The phase preference is often temperature dependent. The perovskite structure is illustrated in Figure 2.1.

Perovskites have been a central material to the development of hydrogen permeable oxides since the research of Iwahara et. al.[40]. This is mainly due to promising flux and stabilities combined with easy modulation of the chemical and electrical properties by structural doping. Even though perovskites currently are not considered amongst the most promising materials, it is the structure of choice for many purposes. Perovskites are used in a variety of applications, e.g. electrodes, semiconductors and solar cells, and numerous properties are well examined due to decades of intense research. Therefore, perovskites serve as a universal reference structure to which others are compared.

## 2.3 The OH defect

Incorporation of hydrogen in crystalline materials is now known to influence a variety of properties, including embrittlement of steel band gap tuning of semiconductors and switchable mirrors and solar collectors of metal-hydrides.[41, 42, 43, 44]

Hydrogen in oxides was initially discovered in the 1950's,[45] but not until the 1980's did research in the field gain popularity when it became evident that hydrogen permeation of doped solid oxides could have possible commercial applications.[24, 40, 46]

### Mechanism for hydrogen uptake

The simplest reaction for formation of hydrogen defects in an oxide is via direct reaction between structural oxygen and gaseous hydrogen.

$$H_2 + 2O_O^x \quad \leftrightarrow \quad 2OH_O^\bullet + 2e'. \tag{2.3}$$

At a given temperature and partial pressure of $H_2$, one is able to obtain the OH defect concentration if the thermodynamics of reaction (2.3) are known

using the principle of electroneutrality and the law of mass action[47]

$$[\mathrm{OH}_\mathrm{O}^\bullet] = n \tag{2.4}$$

$$\exp\left(-\frac{\Delta\mathrm{H}-\mathrm{T}\Delta\mathrm{S}}{k_B\mathrm{T}}\right) = \frac{[\mathrm{OH}_\mathrm{O}^\bullet]^2 n^2}{p_{H_2}[\mathrm{O}_\mathrm{O}^x]^2} \tag{2.5}$$

where $n$ denotes the electronic defect concentration and $p_{H_2}$ the partial pressure of hydrogen.[1] $\Delta$H and $\Delta$S denote enthalpy and entropy.

From several experiments, it is known that the hydrogen uptake reaction is catalyzed by water.[48, 49] An often proposed initial reaction is

$$\mathrm{H_2O} + \mathrm{v}^{\bullet\bullet} + \mathrm{O}^x \leftrightarrow 2\mathrm{OH}^\bullet \tag{2.6}$$

requiring oxygen vacancies. At very high temperatures these may be formed by simple evaporation via

$$2\mathrm{O}^x \leftrightarrow 2\ \mathrm{v}^{\bullet\bullet} + \mathrm{O_2}(g) + 2e' \tag{2.7}$$

but at conditions relevant for applications of proton conducting oxides, the reaction is usually shifted far to the left[2]. For increasing the concentration of oxygen vacancies, structural dopants are introduced intended to destabilize the oxygen stoichiometric structure. For readily doped materials, e.g. perovskites, dopant concentrations up to 30 % and correspondingly high oxygen vacancy concentrations are often reported.[50, 51] The gaseous oxygen from reaction (2.7) may react with gaseous hydrogen thereby closing the catalytic cycle of water.

Even though the net reactions are fairly simple, the actual mechanism may be considerably more complex. Possible steps include gas phase chemistry, gaseous diffusion, evaporation, physisorption, chemisorption, defect interaction, surface chemistry, and bulk diffusion. Little attention has however been given these issues, most likely due to the problems of providing satisfactory bulk conductivities, without which no application of proton conducting oxides can be realized.

### OH defect sites

The site preference of hydrogen in oxides has previously caused some debate. Experimental information of the preferred site is available e.g. from

[1] In this thesis, chemical activities are approximated by concentrations and partial pressures.

[2] Typical enthalpies for reaction 2.7 are above 5 eV.

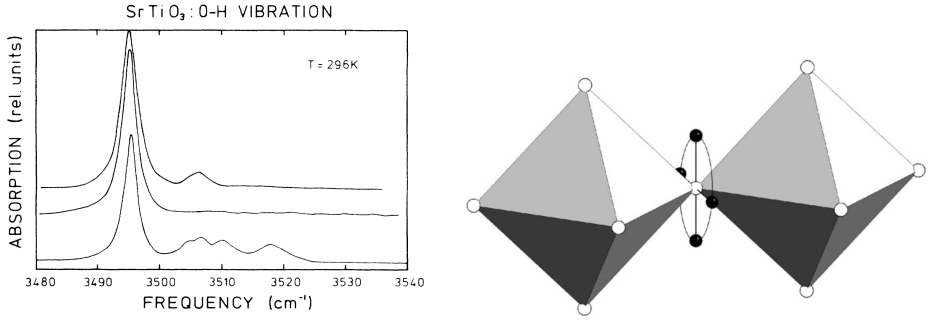


**(a)** **(b)**

Figure 2.2: **(a)** *Infrared spectra of three samples of nominally undoped cubic $SrTiO_3$.[52] The sharp peak at ca. 3500 $cm^{-1}$ is characteristic for the OH stretch vibration in any oxide. The smaller peaks are results of interactions between H and other defects.* ***(b)*** *Schematic illustration of the stable H positions between $BO_6$ octahedra. From Bjørheim et. al. [53]*

infra-red or Raman spectroscopy, and hundreds of spectra have been produced [52, 54]. These consistently show one or more sharp OH and/or OD stretch vibration peaks around 3500 and 2600 $cm^{-1}$ respectively (see Figure 2.2 **(a)**). Generally, the experimental isotopic ratios between $\nu_{OH}$ and $\nu_{OD}$ are close to the theoretical value of $\sim$1.35 confirming the OH/OD origin. Until the development of accurate computer models, especially DFT, it was however difficult unambiguously to relate this information to a specific site.

In undoped materials it has now been realized that OH distances close to 1 Å symmetrically located between neighboring oxygen provide the most stable configuration. See Figure 2.2 **(b)**. [55, 56, 53] Previous suggestions of non-symmetrical H positions or even stable sites inside $BO_6$ octahedra have now largely been abandoned.[57, 58, 59, 60]

Upon introduction of other defects and dopants into the system, the complexity rapidly increases and several symmetry inequivalent oxygen now exist. Consequently, multiple OH peaks are readily observed, red- or blue shifted compared to in dopant free frequency as result of hydrogen-defect interaction [54, 57]. This have been confirmed by theoretical models[57] and *ab initio* calculations.[61, 62] If the second defect is negatively charged, e.g. $Y'_{Zr}$ or $Sc'_{Zr}$, this is readily explained by electrostatic attraction, but also for two positively charged defects the system obtains a lower energy by gathering defects. This may be explained by elastic lattice interactions. See also Chapter 5.

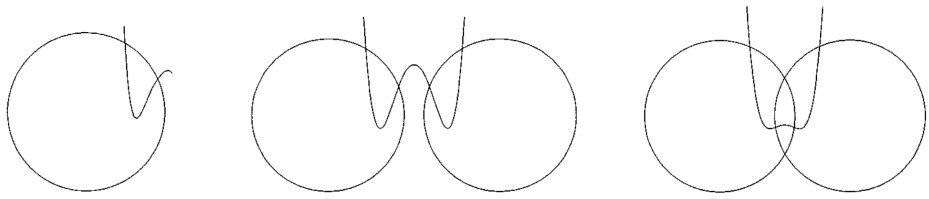


Figure 2.3: **(a)** *Potential energy of a proton and an oxygen ion.* **(b)** *Potential energy of a proton and two oxygen atoms at normal perovskite O-O separation. Note the high energy barrier.* **(c)** *Potential energy of a proton and two oxygen ions when the O-O distance is decreased due to lattice dynamics. The energy barrier is reduced and protonic diffusion is aided. From Kreuer.[67]*

### Diffusion mechanisms

The dynamics of protons in oxides is a key factor to optimize as the main hindrance for application of oxides as membrane material is the low protonic flux. Several different diffusion mechanisms are possible and the dominant mechanism may vary depending on the local environment e.g. surface, bulk or grain boundary.

Since the OH bond distance is ca. 1 Å, it is evident that the proton is deeply embedded in the electron cloud of the host oxygen.[3] See Figure 2.3 **(a)**. A seemingly plausible mechanism for proton transport through transport of entire $OH_O$ defects has therefore been suggested.[64, 65] Even though the activation barriers are similar, this *vehicle mechanism* has convincingly been reputed due to the sign of the charge of the mobile species.[46, 66]

In stead the Grotthuss mechanism is almost exclusively being considered.[68] This mechanism, also referred to as *free proton migration*, is constituted by two elementary processes; rotations of the OH bond and H jumps from one oxygen to another. Often, only jumps between neighbouring oxygen are being considered, but inter-octahedra jumps should also be considered in distorted perovskites.[68] Since H jumps involve a momentary breakage of the OH bond, these are usually associated with a significantly higher activation barrier and thus rate determining. Figure 2.4 is showing the trace of a proton in $BaCeO_3$ illustarting the frequent OH rotation and the rare H jump.

[3] Ionic radius is 1.35 - 1.42 Å dependent of coordination number [63].

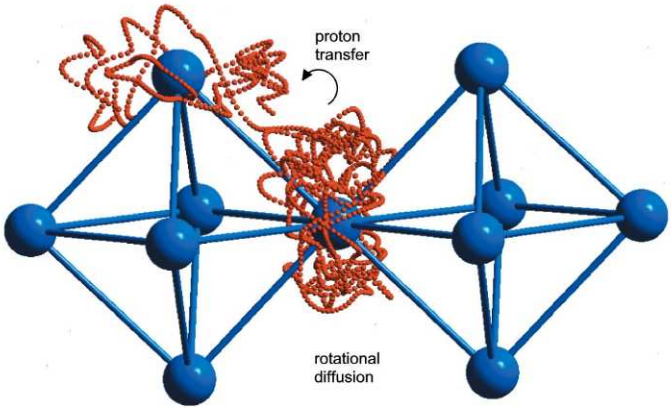


Figure 2.4: *Trace of a proton diffusing in a perovskite, showing the two principal features of proton transport; rotational diffusion and proton jump. Note the numerous OH rotations and only one H jump.[23, 69]*

In cubic and undoped perovskites, only two symmetry inequivalent elementary reactions are present, but as the symmetry is lowered e.g. due to doping, more symmetry inequivalent sites are available and the number of diffusional paths increase. Typically, it is neither possible nor necessary to investigate all paths since the overall diffusional flux, $j$, will be dominated by one or a few paths of particular low energy. This due to the exponential dependence of the activation energy, $E_a$, as

$$j(T) \propto A_0 \exp\left(-\frac{E_a}{k_B T}\right) \tag{2.8}$$

where $A_0$ is the pre-exponential factor, usually close to $10^{13}$ Hz, and $k_B$ Boltzmanns constant. See also section 3.4.4.

For this reason, it was for some time a mystery why proton conduction in perovskites, e.g. $BaCeO_3$, was significantly faster than in other oxides, e.g. $\alpha$-$Al_2O_3$.[4][72] Given the large barrier involved in breaking the OH bond, as illustrated in Figure 2.3 **(b)**, one might expect that structures with small lattice constants and hence smaller O-O separations should yield smaller overall activation barriers.

A more tightly packed lattice is however also more rigid with harder phonon modes, including modes inducing momentary shortenings of the O-O distances. It is now realized that lattice dynamics are very important for

[4]O-O distance: $BaCeO_3$: 3.1 Å. $\alpha$-$Al_2O_3$: 2.5-2.7 Å.[70, 71]

proton diffusion since the momentary shortening of the O-O distances has a significant impact on the barriers for hydrogen diffusion. In soft open lattice structures, including perovskites and pyrochlores, the modes enhancing proton diffusion are softer and greater ionic displacements are seen. Hereby situations corresponding to Figure 2.3 **(c)** are frequent, leading to a higher overall protonic flux.

# Chapter 3

# Theoretical Models

## 3.1 Modelling solid oxide proton conductors

The advantages and possible applications of solid oxide proton conductors have been apparent for decades and the combined experimental and theoretical research has resulted in a huge amount of publications.

Some of the first reported modelling studies of ionic diffusion in solids were in the 70's by Flugare and Huggins[73] and Ajayi et. al.,[74]. Though not specifically concerning protons, these introduced the idea of determining the potential energy as a sum of nuclear Coulomb and electronic overlap terms. In the 80's, after the rediscovery of proton conduction by Iwahara et al.[40], these methods were applied for modelling proton diffusion, e.g. by Mitsui et al. [75]. Most models were however based on rigid lattice approximations and the exclusion of lattice dynamics resulted in activation barriers overestimated by factors of ca. 2-3.

In the 90's, the increased availability of computational power enabled usage of the more flexible and accurate *ab initio* methods.[76, 77, 78] Even though the calculations were rough compared to modern methods, much better results were obtained primarily due to inclusion of lattice dynamics. During that last part of the 90's, significant advances by especially the groups of Kreuer and Islam were seen, much of which still represent benchmark studies.[79, 80, 81]

More recently, *ab initio* methods have been further developed and results are now widely trusted although system sizes are severely limited by computational expense. Studies are therefore continuously targeting subjects where experimental insight may be difficult e.g. defect and dopant interactions,[82, 61, 83] surface structure and chemistry,[84, 85, 86] and

electronic conductivity.[87, 88, 89]

In the next decades *ab initio* methods most likely will be an increasingly trusted tool for prediction of atomic scale properties. The increase in computer power and development of intuitive and easy-to-use software packages will enable also non-specialists to apply *ab initio* methods. Combined experimental and theoretical studies are likely to result in significant advances within development of materials for proton conducting oxides.

## 3.2 Electronic structure methods

The discovery of quantum mechanics (QM) in the early 20'th century marked the beginning of a revolution in the understanding of atomic interactions. QM has during the last decades developed from being an approach for fundamental investigation of the nature of matter to a predictive tool capable of providing insight into atomic and molecular interactions in actual materials.[90]

The following sections will outline the basis on the QM models relevant for the work presented in this thesis. No in-depth presentation is given and the interested reader is referred to the excellent text books of Jensen[91], Helgaker et al.[92], Parr and Yang[93], and Martin.[94] The three former being focused on chemistry, the latter on physics.

### 3.2.1 The Schrödinger equation

At the heart of QM lies the Schrödinger equation,

$$\mathrm{H}\Psi = \mathrm{E}\Psi \tag{3.1}$$

where H is the Hamiltonian operator, E is the energy and $\Psi$ is the wavefunction from which all information about the system can be extracted; most importantly total energy and electronic density.[95]

A many body non-relativistic system consisting of a number of electrons and nuclei is fully described by the many body Hamiltonian,

$$\begin{aligned}\mathrm{H} = &\sum_i \frac{p_i^2}{2m_e} + \sum_I \frac{P_I^2}{2M_I} - \sum_{i,I} \frac{eZ_I}{|\mathbf{r}_i - \mathbf{R}_I|} \\ &+ \sum_{i,\ j>i} \frac{e^2}{|\mathbf{r}_i - \mathbf{r}_j|} + \sum_{I,\ J>I} \frac{Z_I Z_J}{|\mathbf{R}_I - \mathbf{R}_J|}\end{aligned} \tag{3.2}$$

where $m_e$ and $M_I$ are mass of the electron and $I$'th nuclei, $p$ and $\mathbf{r}$ denote the electronic momentum and position, and $P$ and $\mathbf{R}$ nuclear momentum

and position. $e$ and $Z_I$ are the charge on the electron and $I$'th nuclei. More compactly, this is often written as

$$\mathrm{H} = \mathrm{T}_e + \mathrm{T}_n + \mathrm{V}_{en} + \mathrm{V}_{ee} + \mathrm{V}_{nn}. \tag{3.3}$$

The first two terms are the kinetic energy of the electrons and the nuclei while the last two terms are the Coulomb repulsion terms between electrons and nuclei respectively. The third term is the Coulomb attraction between electrons and nuclei.

Offering all information about a system, the wavefunction is in deed attractive but actually solving Eq. (3.1) have not been achieved for other systems than the hydrogen atom. The difficulty arise in the interaction terms of Eq. (3.2), coupling all particles and complicating the Schrödinger equation enormously. For obtaining eigenstates and energies of polyatomic systems, a series of approximations must be employed each simplifying the problem and gradually allowing solutions to increasingly more complex systems.

### 3.2.2 Born-Oppenheimer approximation

The first step towards a solution to the Schrödinger equation is to decouple the motion of the electrons and the nuclei and was proposed already in 1927.[96] Utilizing that the mass of the electron is orders of magnitude smaller than that of any nuclei, it is natural to assume that the motion of the electrons are uncorrelated with the motion of the nuclei. It is thus assumed that the nuclei can be approximated by point charges around which the electrons instantaneously arrange themselves and the Born-Oppenheimer approximation is common for all standard electronic structure methods.

The wavefunction thereby separates into a product of an electronic and a nuclear part,

$$\Psi = \Psi_{elec} \times \Psi_{nuc}. \tag{3.4}$$

Nuclear quantum effects are usually negligible and the nuclei are readily treated classically as point charges. The nuclear part of the total energy is calculated separately from the electronic part and represent only a small fraction of the total computational effort.

The solution to the Schrödinger equation thus lies in solving the eigenvalue problem of the electronic Hamiltonian, $\mathrm{H}_{elec}$, given as

$$\mathrm{H}_{elec} = \mathrm{T}_e + \mathrm{V}_{ee} + \mathrm{V}_{en}, \quad \text{and} \tag{3.5}$$

$$\mathrm{H}_{elec}\Psi_{elec} = E_{elec}\Psi_{elec}. \tag{3.6}$$

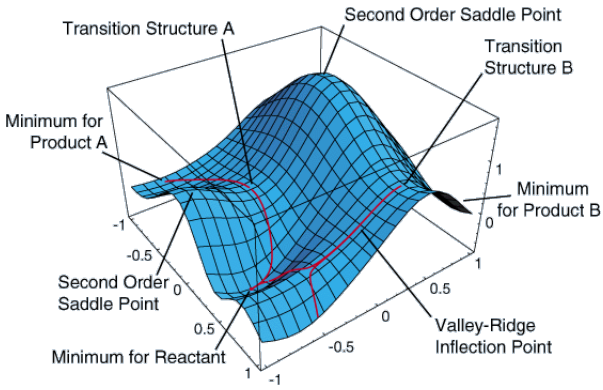


Figure 3.1: *Illustration of potential energy surface showing points of special interest, including minima and saddle points.[97]*

The wavefunction, $\Psi_{elec}$, is the eigenstate describing an electronic state resulting from a given fixed atomic configuration.

By systematically altering the nuclear positions and repeatedly calculating e.g. the energy, one obtains the non-relativistic energy landscape of the system, known as the potential energy surface (PES). On the surface, points of special interest are local minima, minimum energy paths (MEP) between two local minima and transition states being the configuration with the highest energy along a MEP. See Figure 3.1. Although often illustrated as a surface in three dimensions, the PES includes all degrees of freedom of the system of interest plus the energy. Taking a $SrTiO_3$ unit cell as example, the dimensionality of the PES is $3 \cdot 5 + 1 = 16$, requiring a 17 dimentional PES.

## 3.3 Density functional theory

Obtaining the wavefunction through a direct solution of the Schrödinger equation is, despite the simplifications of the Born-Oppenheimer approximation, still severe due to the explicit electron-electron interaction term.

In a simple brute force approach one might attempt to determine each single electron wavefunction by explicit sampling. Assuming we have 10 electrons, as in the water molecule, and we would like to sample each degree of freedom by 5 points we would however end up with $5^{3 \cdot 10} \sim 10^{21}$ gridpoints!

Since even a rough sampling of a small molecule require such enormous

amounts of data, it is obvious that this approach is impractical. Even though there are more clever ways to provide the same information as merely the data sampling, the exponential dependence on the number of electrons is real and severely limiting the system size. This problem is known as the exponential wall.[90]

A way to get around this problem altogether is by an alternative choice of parameters. In stead of explicitly mapping each electronic wavefunction one may use the total electronic density. This is given as

$$\rho(r) = \sum_i |\phi_i|^2 \tag{3.7}$$

where the summation runs over the number of electrons and $\phi_i$ are the single electronic wavefunctions.

The main advantage of this approach is the reduced dimensionality of the equation. In stead of the 3×N dimensions associated with the Schrödinger equation, N being the number of electrons, here, no more than three dimensions are needed regardless of system size.

The fist attempts to use the electronic density as the basic variable were made only shortly after the introduction on quantum mechanics by Thomas and Fermi, and later Dirac.[98, 99, 100] Based on an assumption of non-interacting electrons, significant problems with these models were found, e.g. not predicting bonding, but the basis of DFT was laid. Through the following decades significant progress was seen, e.g. bonding,[101] but with respect to prediction of materials properties of solids or molecules no models were adequate until the early 80's. This was achieved aided by rapid development of both theory and electronic computers. See e.g. Gill [102], Parr and Yang [103] or Kohn et al. [104] for interesting reviews.

Despite decades of research into DFT, the formal justification did not appear until 1964 when Hohenberg and Kohn published the much celebrated first Hohenberg-Kohn theorem.[105] Relying on a Born-Oppenheimer like Hamiltonian

$$\mathrm{H} = \mathrm{T}_e + \mathrm{V}_{ee} + \mathrm{V}_{ne} \ , \qquad \text{but where} \tag{3.8}$$

$$\mathrm{V}_{ne} = \sum_j v(\mathbf{r}_j) \ , \tag{3.9}$$

$v(\mathbf{r})$ being a generalized external potential, the Hohenberg-Kohn theorem proved that the external potential $\nu(\mathbf{r})$ is determined, within an additive constant, by the ground state electronic density $\rho(\mathbf{r})$, i.e.

$$\nu_1 = \nu_2 \Rightarrow \rho_1 = \rho_2. \tag{3.10}$$

Further the second Hohenberg-Kohn theorem proved that for a trial density, $\rho_{trial}(\mathbf{r})$,

$$\mathrm{E}_0 \leq \mathrm{E}_\nu[\rho_{trial}(\mathbf{r})] \tag{3.11}$$

where $\mathrm{E}_\nu$ is the exact ground state functional and $\mathrm{E}_0$ is the exact ground state energy.[105] This being the DFT analog to the variational principle for wavefunctions.[106, 107]

### 3.3.1 Kohn-Sham method

A great improvement in the actual usability of DFT came soon after when Kohn and Sham proposed a new method for obtaining the otherwise unknown external potential.[108] In stead of the early methods of Thomas and Fermi where an explicit formulation of the potential were attempted, the Kohn-Sham scheme relied on iteratively improving the potential self consistently.

The method relies on the partitioning of the many electron wavefunction into single electron wavefunctions, $\phi_j$ with eigenvalues, $\epsilon_j$, in the eigenvalue problem

$$\big[ -\tfrac{1}{2}\nabla^2 + \nu(\mathbf{r}) + \textstyle\int \frac{\rho(\mathbf{r}')}{|\mathbf{r}-\mathbf{r}'|} + \nu_{xc}(\mathbf{r})\big]\phi_j(\mathbf{r}) = \epsilon_j\phi_j(\mathbf{r}), \text{ where} \tag{3.12}$$

$$\nu_{xc}(\mathbf{r}) = \tfrac{\partial E_{xc}[\rho(\mathbf{r})]}{\partial\rho(\mathbf{r})} \ , \tag{3.13}$$

hereby defining the "exchange-correlation" functional, $E_{xc}$.[104]

Following the results of the first Hohenberg-Kohn theorem, this expression is exact given an exact formulation of the $E_{xc}$ functional. This is however unknown and a large amount of research has gone into formulating approximate expressions of the $E_{xc}$ functional, being the only source of error in the Kohn-Sham scheme.

Since the solution to the eigenvalue problem is obtained iteratively, initial trial wavefunctions for the one electron Kohn-Sham wavefunctions must be provided. Solving the Kohn-Sham eigenvalue problem is the single most time consuming process of a typical DFT calculation and a good initial trial density is essential.

### 3.3.2 Pseudopotentials and projector methods

Near the nucleus, the wavefunction is very complex with nodal planes and rapidly alternating values. See Figure 3.2**(a)**. Accurate modelling requires significant computational effort and representing the majority of the total

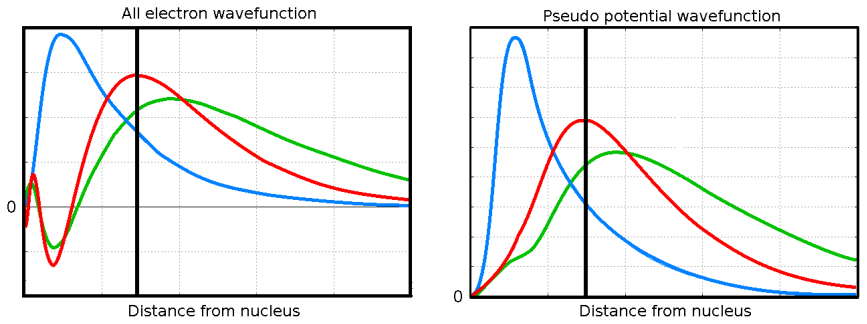


Figure 3.2: *Typical behaviour of* **(a)** *all electron wavefunction and* **(b)** *corresponding pseudo-potential wavefunctions of the s- (red), p- (green), and d-states (blue).[109] The cut-off distance separating core and valence regions is illustrated by the full vertical line corresponding to 2.65* $a_0$.

energy, inaccuracies in this part of the wavefunction may lead to significant errors. The wavefunction close to the nucleus is however largely invariant during the chemical processes of interest, only affecting the valence part of the wavefunction. An alternative description of the core states is via pseudopotentials, whereby a simplified description of the core is used [110]. See Figure 3.2 **(b)**. Due to error cancellation, the resulting errors in total energy are minor if a proper pseudopotential is used while the computational savings are great.

Another method is the projector augmented wave method (PAW).[111] Again the crystal is divided into core and valence regions by appropriate cutoff distances from the nuclei. The smooth part of the wave function, outside the core, is represented by plane waves while inside the core, the wave functions are atomic like. Again, suitable boundary conditions are important and the method is presently amongst the more promising.

### 3.3.3 Functionals

Despite a formal proof of the validity of DFT and an effective scheme for obtaining the density, one still need to determine the actual functional connecting the density and energy (Eqs. (3.12) and (3.13)). As a result of intense research, the development of accurate functionals has been one of the most successful areas within theoretical chemistry in the last decades. Generally speaking, most functionals are developed by incorporating as

much correct physics as possible and parametrizing whatever remains.[1] By explicit inclusion of some properties above others, fine tuning of the functional towards a given area of interest is possible, e.g. surface, bulk or gas phase chemistry or being mainly focused on a specific functional group, a set of transition metals or specific class of chemical reactions.

From the works of Thomas and Fermi, the exact functional linking the uniform electron gas to kinetic electronic energy is known as

$$\mathrm{T}^{TF} = \frac{3}{10}(6\pi^2)^{2/3} \int \rho^{5/3}(r)dr \tag{3.14}$$

which can be derived exactly using the wave functions of a particle in a box.[98, 99] The non-uniformity of real systems can not be treated exactly but must be approximated. The first approximation is the local density approximation (LDA)[108] where the energy depend on the electronic density e.g. simply as

$$\mathrm{E}_{xc}^{LDA} = \int \mathrm{T}^{TF}[\rho] \cdot \rho(r)dr. \tag{3.15}$$

LDA is a great improvement to the homogeneous electron gas approximation and predicting structure within 1-2 % of experiment, but fails for predicting magnetic properties and band gaps and generally overestimate bond strengths.

An improvement to LDA is the generalized gradient approximation (GGA), where the functional depends not just of the electronic density but of the gradient of the density as well. Although computationally more expensive than LDA, currently, GGA is the method of choice due to the much improved accuracy. Structural properties are predicted well within 1 % and energy differences approaching "chemical accuracy" (1 kJ/mol) can be reached.

In this thesis, being focused on solid state chemistry in the bulk of the material, the GGA functionals by Perdew, Burke and Entzerhof (PBE)[112] and Perdew and Wang (PW91)[113] have been chosen since these, in numerous papers, have been shown to perform well.

It is however known that both LDA and GGA functionals have a tendency to over-delocalize electrons. This is not a problem if only energies are of interest, but if e.g. band gaps or atomic charges are of interest the over-delocalization must be dealt with. A recent approach is LDA+U

[1] By parametrizing a part of the energy, DFT, strictly speaking, is no longer a pure *ab initio* method, but rather a semi-empirical method relying on experimental data. Due to the *ab initio* line of thought behind DFT, or perhaps due to the promises of the first Hohenberg-Kohn theorem, DFT is referred to as an *ab initio* method anyway.

based on a Hubbard interaction model.[114, 115] The main idea is to divide the system into localized and delocalized electrons. The localized electrons are described using LDA while the delocalized electrons are described by the Hubbard like interaction term $\mathrm{E}^U = \frac{1}{2}\mathrm{U}\sum_{n_i \neq n_j} n_i n_j$ which is added to the LDA functional. $n$ is denoting d- and f- orbitals and U a tuneable interaction parameter.

Presently, LDA+U yields energies and structures of poorer quality than LDA,[116] but is a good method for reproducing properties relating to excited states or the topology of the electronic density. A disadvantage is the lack of a good approach for determining the parameter U, besides comparison with experimental data e.g. the band gap.

### 3.3.4 Software packages

Since the Kohn-Sham equations cannot be solved analytically, numerical solutions are sought in stead. Numerous *ab initio* software packages are available, often developed with a specific purpose e.g. to describe surfaces, bulk properties, or molecules. Three packages have been used in this study, DACAPO,[117] GPAW[118], and VASP[119]. The DACAPO and GPAW packages have both been developed at CAMD/DTU and are open source packages. The VASP package has been developed at the University of Vienna and is commercially available.

The DACAPO package is based on ultra-soft pseudopotentials and is relatively fast and well tested while the GPAW package, based on the PAW method, still is under development but show promising parallalization performance and has shown good accuracy in band gap determination.

The VASP package, also PAW based, is the oldest and most well established package of the three. Calculations are generally very fast and reliable.

## 3.4 Statistical mechanics

A well known limitation for basic DFT modelling is the inability to describe excited states since the first Hohenberg-Kohn theorem only deals with ground state electronic densities, i.e. systems at 0 K. To describe a given system at non-zero temperatures, statistical mechanics is an obvious choice.

### 3.4.1 Free energy

The free energy is the single most important property for the work presented in this thesis. The Gibbs free energy, G, and enthalpy, H, are as usual defined as

$$\mathrm{G} = \mathrm{H} - \mathrm{TS} \quad \text{and} \tag{3.16}$$

$$\mathrm{H} = \mathrm{U} + \mathrm{pV} \tag{3.17}$$

where U is the internal energy, p is the pressure, V is the volume, T is the temperature and S is the entropy [47]. In the reactions and processes in the present thesis no changes in volume or pressure are treated, implying that the change in Gibbs energy during a reaction is given as usual

$$\Delta\mathrm{G} = \Delta\mathrm{H} - \mathrm{T}\Delta\mathrm{S}, \quad \text{or equivalently} \tag{3.18}$$

$$\Delta\mathrm{G} = \Delta\mathrm{U} - \mathrm{T}\Delta\mathrm{S}. \tag{3.19}$$

where U is obtained from the Kohn-Sham equations. Since the Helmholtz free energy is given as F = G - pV, this and Gibbs free energy are identical in the present thesis.

### 3.4.2 Entropy

Several contributions to the total entropy in a system are possible. For the systems at hand, vibrational and configurational contributions are the most important and will be described in the following. For dilute solution, configurational entropy may be an important contribution whereas vibrational entropy should be considered always.

#### Configurational entropy

The configurational entropy arise from the possibility of a given macrostate to adopt multiple microstates. The more microstates possible the higher the entropy given via the elegantly simple Boltzmann equation,

$$S_{config} = k_B \ln(\Omega) \tag{3.20}$$

where $k_B$ is Boltzmann constant and $\Omega$ is the number of microstates available for the particular macrostate.[120] The number of conformations is determined by the binomial distribution,

$$\Omega = \binom{N_1 + N_2}{N_1} = \frac{(N_1 + N_2)!}{N_!!\ N_2!} \tag{3.21}$$

where $N_1$ and $N_2$ represent number of sites of two species (e.g vacancies and structural atoms) with maximum at $N_1 = N_2$. To avoid the factorials, being difficult to handle for large $N_1$ or $N_2$, Stirlings approximation is often useful,

$$\ln(n!) \approx n\ln(n) - n + 1. \tag{3.22}$$

This lead to the generalized expression

$$S_{config} = -k_B N \sum_i x_i \ln(x_i), \tag{3.23}$$

where $N = \sum_i N_i$ is the total number of sites and $x_i = N_i/N$ is the mole fraction. $i$ is representing the various species [121].

**Vibrational entropy**

The vibrational levels cause an important contribution to the entropy of a system. The entropy is given as

$$S_{vib} = -\frac{\partial \mathrm{F}}{\partial \mathrm{T}}\bigg|_{\mathrm{V,N}} \text{where} \tag{3.24}$$

$$\mathrm{F} = -k_B \mathrm{T} \ln(Q). \tag{3.25}$$

F denotes the Helmholtz free energy and $Q = \sum_i \exp(-\mathrm{E}_i/k_B\mathrm{T})$ denotes the partition function. The vibrational entropy can be deduced as

$$S_{vib} = \sum_{j=0}^{\infty} \left[ \beta h\nu_j \cdot \frac{\exp(-\beta h\nu_j)}{1-\exp(-\beta h\nu_j)} - \ln[1-\exp(-\beta h\nu_j)] \right] \tag{3.26}$$

where $\beta = (k_B T)^{-1}$.[122]

### 3.4.3 Vibrational analysis

It is often of relevance to determine the vibrational frequencies resulting from a given configuration, typically an optimized structure or a transition state. These are readily obtained by evaluating the mass scaled inter-atomic forces given as

$$C_{i,j} = \frac{1}{\sqrt{M_i M_J}} \frac{\partial^2 E}{\partial R_i \partial R_j} \tag{3.27}$$

where $M_i$ and $R_i$ refer to the mass and position of the $i$'th nucleus.[123] Upon diagonalizing this Hessian matrix, the eigenmodes and eigenvectors

are obtained which readily are transformed back to forces. Typically, a finite difference approach is applied for determining the energy derivatives. Assuming a harmonic potential, the forces relate directly to the frequencies as

$$\omega = \frac{1}{2\pi}\sqrt{\frac{k}{\mu}} \tag{3.28}$$

where $k$ is the force constant and $\mu$ is the reduced mass of the oscillator.

### 3.4.4 Transition state theory

Transition state theory (TST) provides a simple way of calculating reaction rate constants once the geometry, energy and frequencies of reactants and transition state have been determined. Since these data can be obtained by standard DFT calculations, this method is widely applied despite some shortcomings.[124]

Four basic assumptions are necessary for the derivations:

1. The Born-Oppenheimer approximation applies.
2. Tunneling effects are insignificant.
3. Thermal equilibrium exist.
4. The transition state is crossed only once per reaction.

Even though tunneling effects may be relevant for many reactions especially involving hydrogen, these are not important at the temperatures relevant for this theses, but the "no recrossing" assumption is often unjustified at elevated temperatures. Due to this, TST obtained rate constant are upper bounds to the true rate constants. Several methods for compensating for the inaccuracies imposed by these assumptions have been developed, but have not been applied in the present thesis. See Hänggi et. al. for a full review.[124]

Considering a generalized reaction with energy barrier $E_a$, as illustrated in Figure 3.3,

$$\mathrm{AB{+}C} \rightleftharpoons \mathrm{ABC\#} \rightarrow \mathrm{A{+}BC}, \tag{3.29}$$

the reaction rate constant, $k^{TST}$, may be evaluated in terms of partition functions, Q, leading to a reaction rate constant

$$k^{TST}(T) = \sigma_{symm}\frac{k_B T}{h}\frac{Q^{ABC\#}}{Q^{AB}Q^{C}} \times \exp\left(\frac{-E_a}{k_B T}\right) \tag{3.30}$$

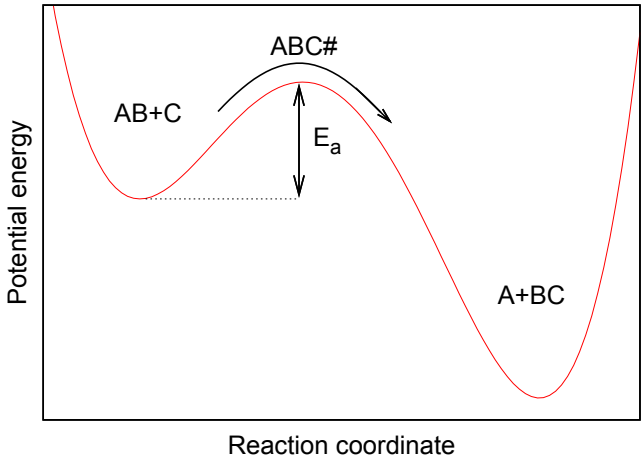


Figure 3.3: *Generalised energy profile of a reaction with an energy barrier of $E_a$. Note the one-way arrow across the transition state, ABC, illustrating the no-recrossing assumption.*

where $E_a$ is the barrier height.

Calculating the partition functions can pose problems, but should the vibrational modes be approximately harmonic, the partition functions may be replaced by the frequencies, $\nu$, as

$$k^{hTST}(T) = \frac{\prod \nu_{AB+C}}{\prod \nu^{\dagger}_{ABC\#}} \times \exp\left(\frac{-E_a}{k_B T}\right) \tag{3.31}$$

where † indicate that the imaginary frequency should be omitted.[125, 126] The harmonic rate constant, $k^{hTST}$, may thus be interpreted as the product of an attempt frequency (to cross the energy barrier) times and a reaction probability. The harmonic approximation is unjustified for high temperature reactions, but under such conditions the no-recrossing requirement makes TST unsuited at all [2]. A general rule of thumb dictates that the harmonic approximation is valid until half of the melting point of the material. Under conditions relevant for this work, hTST is generally justified and will be used throughout.

[2] Neither DFT is then applicable since only electronic ground states should be treated

### 3.4.5 Hellmann-Feynman theorem

As the system grow beyond a few atoms, the dimensionality of the PES become difficult to handle and mapping of the entire surface become impossible. Numerous algorithms developed to locate minima or transition states are however applicable.

The gradient of the surface at a given point is an important property for predicting the location of the minimum or maximum and can be obtained via the Hellman-Feynman theorem.[3][127, 128] This state that the change of energy with respect to a nuclear coordinate $\lambda$, is the expectation value of the derivative of the Hamiltonian, since

$$\frac{\partial E}{\partial \lambda} = \left\langle \frac{\partial \Psi}{\partial \lambda} \middle| H \middle| \Psi \right\rangle + \left\langle \Psi \middle| \frac{\partial \mathrm{H}}{\partial \lambda} \middle| \Psi \right\rangle + \left\langle \Psi \middle| H \middle| \frac{\partial \Psi}{\partial \lambda} \right\rangle \tag{3.32}$$

$$= \left\langle \Psi \middle| \frac{\partial \mathrm{H}}{\partial \lambda} \middle| \Psi \right\rangle + E \frac{\partial}{\partial \lambda} \langle \Psi | \Psi \rangle = \left\langle \Psi \middle| \frac{\partial \mathrm{H}}{\partial \lambda} \middle| \Psi \right\rangle. \tag{3.33}$$

This is solvable within the Born-Oppenheimer approximation since the electronic kinetic energy does not depend on nuclear coordinates (see Eq. (3.14)). The electronic part of $\partial E/\partial \lambda$ can thus be calculated by the interaction of the electron density with point charges and the ionic contribution can be calculated classically.

Determination of energy-derivatives is hereby possible from a single wavefunction, much more efficient than e.g. finite difference approaches where 2 or more wavefunctions are needed.

It should be noted that the Hellmann-Feynman theorem only holds for variational methods, e.g. methods obeying the Rayleigh-Ritz variational principle.[106, 107] This states that a trial wavefunction, $\Psi_{trial}$, yields upper bound energies to the true ground state energy, $E_0$;

$$E_0 = \langle \Psi_{exact} | H | \Psi_{exact} \rangle \leq \langle \Psi_{trial} | H | \Psi_{trial} \rangle \tag{3.34}$$

As consequence, forces are considerably more difficult to accurately determine than energies. Inaccuracies in the wavefunction will lead to second order errors in the energy while leading to first order errors in the forces. Hence, accurate determination of properties from forces, e.g. vibrational frequencies or phonon modes, requires significantly more computational effort.

[3] Also known as the force theorem

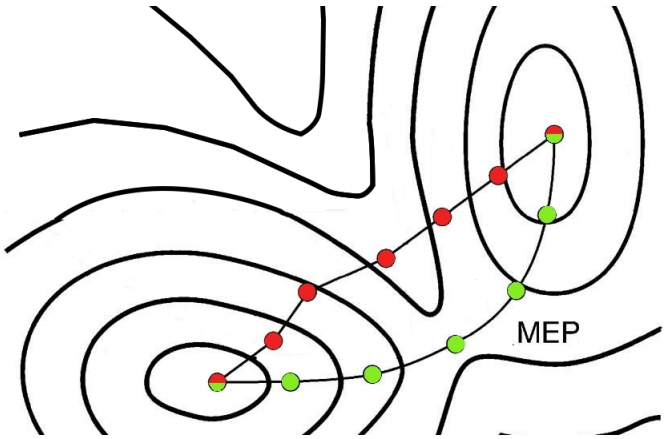


Figure 3.4: *Illustration of the NEB method showing the initial guess path (red) and the relaxed minimum energy path (green). Note the even spacing of the images ensured by the artificial spring forces between them.*

### 3.4.6 Nudged elastic band

Determining the reaction path between two stable configurations, i.e. two local minima, is inherently complex due to the high dimensionality of the potential energy surface (PES). If both reactant and product are known, the problem may elegantly end efficiently be solved using the nudged elastic band method (NEB). A chain of configurations along an initial guess reaction path are constructed and linked by artificial spring forces to ensure a continuous description. Including only forces perpendicular to the band, the entire chain is relaxed with the spring fores preventing all images ending up in the minima.[129, 130] See Figure 3.4.

This will often give a good description of the reaction path with the image highest in energy representing the transition state. Should a more accurate description of the transition state be required, one may choose simply to further optimize this configuration in a separate calculation. This approach is incorporated in the climbing image approach (cNEB).[131] Here, the forces along the reaction path on the likely transition state image are reversed, thereby pushing the image with the highest energy towards the actual transition state.

Even though the NEB method is a fast and reliable method of obtaining a continuous reaction path, one should note that no guarantee is given that the path in fact is the global minimum energy path. The NEB method has no awareness of other ridges in the PES and will identify the local

transition state only. Another drawback is that both reactant and product states must be known prior to the calculation. If no knowledge of these configurations is available, other approaches may be more useful e.g. the dimer method.[132, 133]

## 3.5 Bader charge analysis

The topic of assigning charges to atoms in polyatomic systems has been relevant since the discovery of the electron and the early realization that the concept of charges are critical in many relations. Since much of the current understanding and modelling of electrochemistry is built on the concept of atomic charges, this subject is still highly relevant.

The main problem is the fact that atomic charges neither are observables nor does a universal definition of atomic charge exist. Despite of this, several methods for assigning atomic charges have been developed and even though none of them can be tested against experimental data, some are in deed better than other. The Bader charge analysis is presently the benchmark method for assigning atomic charges in bonded systems since the method is rigid and contrary to most other methods, it has a thorough theoretical base.

The atomic system is partitioned into regions divided by "zero-flux" surfaces, which are minima with respect to the electronic density e.g. points satisfying

$$\nabla\rho(\mathbf{r}) \cdot n(\mathbf{r}) = 0 \tag{3.35}$$

where $\nabla\rho$ and $n$ are the derivative and normal vector to the density $\rho$. See Figure 3.5.

By dividing the system this way a number of regions are found, which, except for a few special exceptions, each contain one nuclei.[134, 135] By this procedure one thus divides the molecule into atoms in a rigorous and unbiased manner based on the electronic density distribution only. In standard LDA and GGA functionals, problems exist in over-delocalizing electrons which may effect the resulting Bader charges. Here, the LDA+U method may be applied since the electron-electron interaction is more explicitly dealt with and the core densities more reliable.

The derivations of the rigidity of the methods are based in field theory and changes in the Lagrange- function operator

$$\delta\mathcal{L}[\Psi, t, \Omega] = \frac{\epsilon}{2}\frac{i}{\hbar}\left\langle\Psi\right|\left[H, G\right]\left|\Psi\right\rangle_{\Omega} + const. \tag{3.36}$$

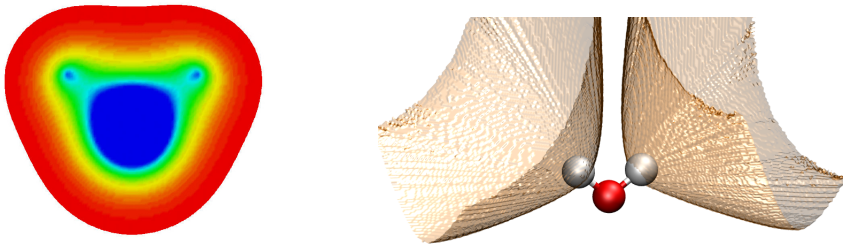

**(a)** **(b)**

Figure 3.5: *Map of the $H_2O$ electronic density and the corresponding Bader volumes*

where $t$ and $\Omega$ denote time and a region in space while $\epsilon$ denote an infinitesimal change and $G$ is an observable. See Bader[136, 137] or Lipkowitz and Boyd[138] for further reading.

## 3.6 Electronic transport theory

Determining the electronic conductivity using *ab initio* methods are significantly more difficult than the ionic conductivity. The electronic conductivity is however of great importance since a fuel cell electrolyte with some electronic conductivity will experience decreased efficiency, as will a gas separation membrane with limited electronic conductivity.

Many approaches towards developing models for electronic transport have been developed. For decades the Marcus model, developed in the 1950's, was the benchmark model for electron transfer reactions. This relied on a purely classical approach for electron transfer in solvated systems (including solid suspensions) and a Born-Oppenheimer like assumption that the electronic transfer is much faster than the corresponding ionic response.[139, 140]

Considering the generalized electron transfer reaction

$$A + B \rightarrow A^+ + B^- \tag{3.37}$$

the electron transfer rate constant is described by a transition state theory like expression, but with a modified activation barrier given as

$$E_a = \frac{(\lambda + \Delta G)^2}{4\lambda} \tag{3.38}$$

where $\Delta G$ is the Gibbs free energy of the reaction and $\lambda$ the reorganization energy. See Marcus for details.[141]

Combining DFT and Marcus theory is difficult due to the inability of basic DFT to treat electronic excitations. This may however be achieved using e.g. time dependent DFT methods. From an initial state, $\Psi_i(t)$, the system is known to evolve in time as

$$i\hbar\frac{\mathrm{d}\Psi_i(t)}{\mathrm{d}t} = \mathrm{H}(t)\Psi_i(t) \tag{3.39}$$

where $\mathrm{H}(t)$ is the time dependent Hamiltonian. This is equivalent to the normal Hamiltonian given in Eq. (3.8), but where the electronic density is depending on all previous densities. These are most often unknown so an initial density must be provided. The initial state, $\Psi_i(t)$, may be expanded into basis functions, $\chi_j$, with time dependent expansion coefficients, $c_j(t)$, as

$$\Psi_i(t) = \sum_j c_j(t)\chi_j. \tag{3.40}$$

For electronic transport methods, localized atomic-like basis functions are suitable. Hereby, the evolution of the system may be followed explicitly from time step $n_0$ to time step $n_1 = n_0 + \delta t$ via the ecpansion coeficients as,

$$c^{n_1}(t) = \sum_k \exp(-\mathrm{iM}\delta t)c_k^{n_0} \tag{3.41}$$

where M is the time evolution matrix.[94] Results are often basis set dependent and computationally very expensive but the method is still under development. Current focus is mainly on molecular or nano-sized junctions between two leads, due to the interest in transistor technologies.[142, 143, 144]

# Chapter 4

# Screening studies

When optimizing a given material towards a given property, an often used method is that of doping or alloying, whereby new stable phases with different thermodynamic and kinetic properties may be produced.[145] Even though this technique has been applied since the bronze ages, large uncertainties in predicting the properties of a given alloy are present. Successful development of a new material, to a large degree depends on chemical and physical intuition of the scientist. Improving the understanding of doping and alloying would enable prediction the properties with higher certainty and thereby provide guidance to the experimentalist with more efficient research as a consequence.

This has been realized early and systematic screening of e.g. alloy ratios has been performed since historical times. With the development of the mathematical and theoretical tools necessary to model atomic interactions, most successfully via quantum mechanics, screening of hundreds of different materials in very short time has become possible. Further development of methods for accurate screening studies may prove a valuable method for most parts of material science.

Examples include Jones et al.[146] where DFT and experiment has been combined to determine surface binding energies as the main descriptors for the kinetics of methane steam reforming. Also combining DFT and experiment, Studt et al.[147] have identified a Ni-Zn catalyst for selective hydrogenation of acetylene, outperforming the usual palladium based catalysts. These examples demonstrate the usability of screening studies, which, although relying on simplified kinetic models and idealized structures, are able to identify the rate limiting elementary reactions and suggest new materials for selectively improving the kinetics of these.

## 4.1 Borohydrides

### 4.1.1 Motivation

Related to the motivation for conducting research into gas separation membranes and electrolytes, solid state hydrogen storage is seen as an important part of a future energy infrastructure independent of fossil fuels.[10, 8, 148, 149] Also here, materials with proper thermodynamic and kinetic properties are absent and significant advances are needed before solid state hydrogen storage will become commercially attractive.

Storing the hydrogen as a simple metal hydride has been extensively examined, but much too high temperatures for hydrogen release are generally needed. Therefore, interest has recently shifted to complex hydrides, e.g. borohydrides ($BH_4^-$) or ammonia ($NH_3$). Many ternary borohydrides[1] have been investigated both theoretically and experimentally, but the large parameter space makes systematic and efficient laboratory studies difficult. See Sakintuna et al.[17] or Orimo et al. for recent reviews [150].

We performed a systematic screening study of 757 structures to discover novel metal borohydrides suitable for hydrogen storage. All structures were investigated using DFT calculations focusing on structural and thermodynamic properties. The results have been published in *Journal of Chemical Physics* and will be outlined in the following. The published paper is appended as Article I and should be consulted for detailed descriptions of motivation, methods and results.

### 4.1.2 Methods

The compositions under investigation had the general formula $M_1M_2(BH_4)_{2-5}$ and are shown in Table 4.1. All possible combinations of coordination of the $BH_4$ groups to the metallic cations were investigated resulting in 757 different structures. These were believed to include all possible compositions of this general formula with high volumetric and gravimetric hydrogen density as required for mobile applications.

A general idea of this study was to include as many structures as possible, but since most of the relevant structures are unknown or too large for screening purposes, template structures were used in stead. A previous study had demonstrated the possibility of obtaining good estimates of free energies with small model structure as long as the local coordination of the borohydride groups was correct.[151] Careful measures were taken to

[1] $M_1M_2(BH_4)_{2-5}$, where $M_1$ and $M_2$ are metals

Table 4.1: *Investigated compositions in the screening study. The structures have the general formula $M_1M_2(BH_4)_X$. All combinations of trigonal planar, tetragonal and octahedral coordination of the $BH_4$ groups to the metals were investigated.*

| $M_1$ | $M_2$ | X |
|---|---|---|
| Li, Na, K | Li, Na, K, Ni, Pd, Cu, Ag | 2 |
| Li, Na, K | Li, Na, K, Mg, Al, Ca, Sc-Zn, Y-Mo, Ru-Cd | 3-4 |
| Li, Na, K | Ti, Zr | 5 |

ensure the quality of the template structures since the quality of the study would rely on these. These are shown in Figures 1 and 2 in Article I. The pre-determined template structures provided an initial guess for the structure of a given compound and after systematic structural optimization the relevant properties could be extracted.

The first requirement for a hydrogen storage material was stability towards decomposition to the parent borohydrides i.e. the reaction

$$\mathrm{LiSc(BH_4)_4} \longrightarrow \mathrm{Li(BH_4)} + \mathrm{Sc(BH_4)_3} \tag{4.1}$$

should be entropic. If a given compound had positive $\Delta E_{alloy}$ this material was not considered as a promising candidate, $\Delta E_{alloy}$ being the free energy difference of reaction (4.1).

The second requirement for hydrogen storage materials was proper thermodynamics for hydrogen release. If too strongly bound, excessive heating will be required for hydrogen release but if too weakly bound, the high equilibrium pressure will impose possible safety issues. The route for hydrogen release is however vastly different from material to material often involving several intermediate metastable structures, e.g. hydrides or boranes. Detailed decomposition analysis for each of the 757 structures was much too extensive so only complete decomposition to elementary metals and boron was considered, here illustrated for $\mathrm{LiSc(BH_4)_4}$,

$$\mathrm{LiSc(BH_4)_4} \longrightarrow \mathrm{Li} + \mathrm{Sc} + 4 \cdot \mathrm{B} + 8 \cdot \mathrm{H_2}. \tag{4.2}$$

A value for $\Delta E_{decomp} = -0.2$ eV/$\mathrm{H_2}$ was considered optimal, but materials deviating of up to $\pm 0.1$ eV/$\mathrm{H_2}$ were considered promising.

### 4.1.3 Results

Of the 757 initial structures only 22 were stable towards the binary borohydrides ($\Delta E_{alloy} < 0$) and their gravimetric hydrogen densities are illustrated as function of $\Delta E_{decomp}$ in Figure 4.1.

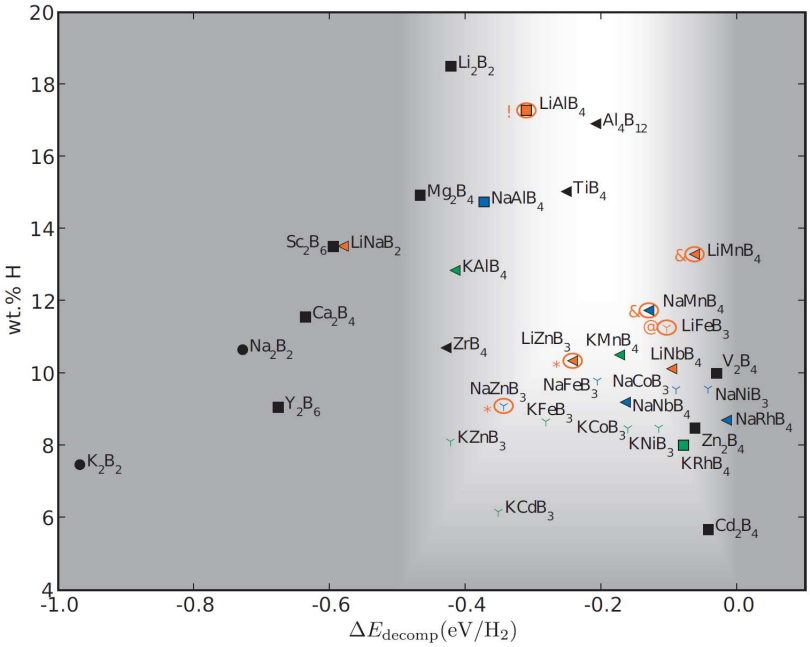


Figure 4.1: *Gravimetric hydrogen densities of the 22 stable alloys as well as the binary reference compounds. In the data point labels, "B" is shorthand for the $BH_4$ group. Full symbol explanation is available in Article 1.*

From Figure 4.1 it is apparent that few of the binary structures posses proper thermodynamics for hydrogen uptake/release, most being too stable. However many of the ternary materials are in the right thermodynamic window illustrated as the non-shaded region.

Many of these materials have been investigated previously, including $LiAl(BH_4)_4$,[152] $(Li/Na)Mn(BH_4)_{3-4}$[153] and $(Li/Na)Zn(BH_4)_{3-4}$.[154] Several novel materials were however also found which remain to be synthesized and tested, including alloys of Co, Cd, Nb, and Rh.

### 4.1.4 Conclusions

Materials for solid state hydrogen storage are important for the future energy infrastructure but novel materials are needed. Large theoretical screening studies have previously been avoided since many of the involved structures are large and decomposition pathways complex or unknown. This study demonstrated the usability of simplified template structures where the local coordiantion was correct, being applied to a large number of possible materials.

Screening of 757 ternary structures with the general formula $M_1M_2(BH_4)_X$, revealed 22 stable structures of which ∼10 were predicted to posses attractive thermodynamics for hydrogen release and uptake. Amongst these, a few novel ternary materials, including alloys of Co, Cd, Nb, and Rh, were identified and are obvious candidates for further investigated both theoretically and experimentally.

## 4.2 Solid oxides

### 4.2.1 Motivation

Inspired by the results presented in the previous study, a similar study aimed at proton conductivity in solid oxides was performed.

Since the rediscovery of proton diffusion in oxides almost 30 years ago,[40] hundreds of materials have been investigated but none have shown satisfactory flux properties. The approach of most of these studies have been to guess a materials composition that may perform well whereafter this has been synthesised, characterized and tested. Even though this approach is useful and most of our current knowledge has been obtained this way, it is also very time consuming. Since the parameter space is large, countless hours are spent on materials inferior to already known compositions.

Correlations and descriptors, such as the Brøndsted-Evans-Polany effect, [155] are thus highly desirable as these may aid the experimentalist in selecting suitable materials, dopants, and doping levels. We performed a screening study aimed at discovering correlations suitable for this purpose. The main results have been published in *Physical Review B* and the article is appended as Article II wherein all details are presented.

### 4.2.2 Methods

Since the aim of this study was not only thermodynamic but also kinetic properties, limitations in the choice of materials were necessary. In cubic and dopant free perovskites, all oxygen atoms are equivalent and no two H jumps and no two OH rotations are different. This is opposed to doped or non-cubic structures where numerous different elementary reactions are possible and necessary for extended diffusion. Therefore, only undoped cubic and pseudo-cubic materials could be included in this study and only $A^{\mathrm{II}}B^{\mathrm{IV}}\mathrm{O}_3$ type materials were considered. The chosen compounds are listed in Table I in Article II.

From the initial structural optimizations and subsequent NEB calculations, a variety of properties were extracted. These included O-H distances and frequencies, H binding energies, energy barriers and pre-factors along with various other properties including electronegativity, ionic radii and Goldschmidt tolerance factors.[156] Amongst these properties correlations were sought.

### 4.2.3 Results

Considering the net reaction for hydrogen uptake

$$^1/_2\ \mathrm{H}_2(g) + \mathrm{O}_\mathrm{O}^x \rightarrow \mathrm{OH}_\mathrm{O}^\bullet + \mathrm{e}'. \tag{4.3}$$

a strong correlation between the thermodynamics this and the two activation barriers of diffusion was found. See Figure 4.2. Relying on the strength of this correlation, future screening studies can calculate thermodynamic properties only while still obtaining kinetic information, thereby significantly reducing the computational effort. Hereby inclusion of many more materials and compositions will be possible as demonstrated in the borohydrides study.

This inverse proportionality between mobility and concentration has been found in other studies [61, 62, 155] and is an important point to emphasize. The task of optimizing the overall protonic flux through the membrane is therefore a task of finding the optimal tradeoff between mobility and concentration.

Since properties such as flux or conductivity scale approximately linear both with protonic concentration, $[\mathrm{OH_O}]$, and total rate constant, $k(\mathrm{T})$, the product of these, $\Gamma$, was the simplest way of comparing the diffusional properties of the materials in question;

$$\Gamma(T) = k_{eff}(T) \cdot [\mathrm{OH_O}]. \tag{4.4}$$

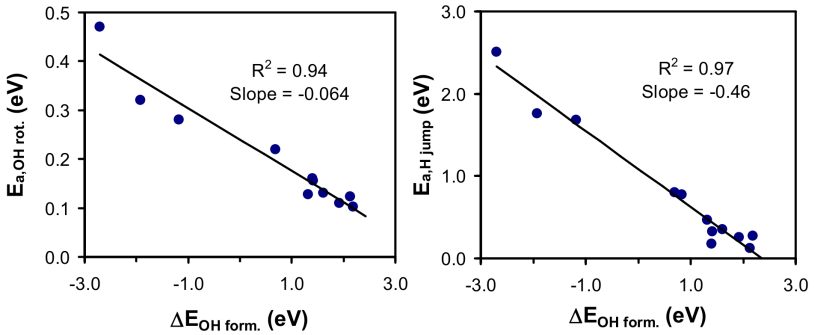


Figure 4.2: *Correlations between thermodynamics of reaction (4.3) ($\Delta E_{OHform}$) and energy barriers for the two Grotthuss type diffusional steps ($E_{a,OHrot.}$ and $E_{a,Hjump}$). Note the high coefficient of determination.*

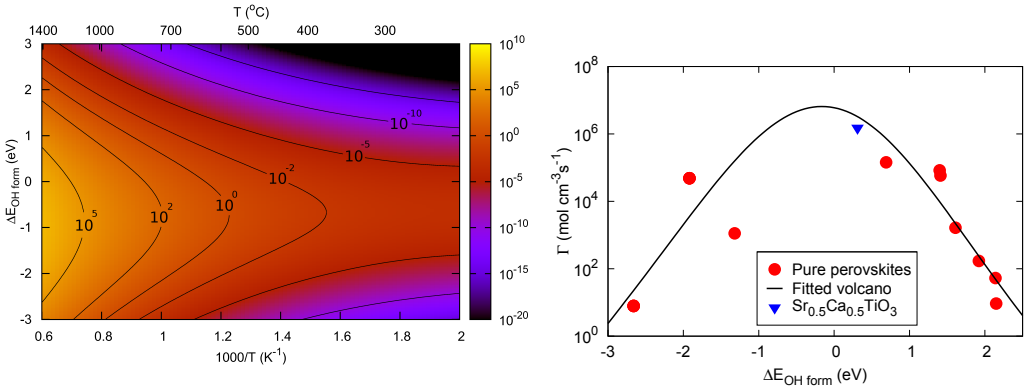


**(a)** **(b)**

Figure 4.3: **(a)** *Plot of $\Gamma = k_{eff}(T) \cdot [OH_O]$, as function of temperature and $\Delta E_{OHform}$.* **(b)** *Plot of $\Gamma$ as function of $\Delta E_{OHform}$ at $T = 800\,^{\circ}C$. The alloyed perovskite, $Sr_{0.5}Ca_{0.5}TiO_3$ (blue triangle), has more than one order of magnitude higher protonic flux than any of the pure perovskites.*

Both protonic concentration and diffusion rate constant could readily be determined based on the DFT calculations (see sections 2.3 and 3.4).

A plot of $\Gamma$ as function of temperature and $\Delta E_{OHform}$ is presented in figure 4.3 **(a)**. Opposed to many experimental studies, no optimum in temperature was found indicating that the correlation may not hold for very high temperatures.[23, 157] This may be due to insufficient description of entropic effects driving the dissolved protons out of the material at high temperatures. An optimum value for $\Delta E_{OHform}$ was however apparent, optimally balancing protonic concentration and mobility. At temperatures relevant for hydrogen permeable membranes (300 - 800°C) the maximum is found around $\Delta E_{OHform}$ = -0.5 eV and it is noticeable that none of the materials investigated are found in this desirable region.

Even though the thermodynamic properties of a given material are given, these are often possible to modify through careful doping. Improving the tradeoff between mobility and concentration by tuning the thermodynamics of reaction (4.3) towards $\Delta E_{OHform}$ = -0.5 eV thus seemed a viable approach for optimizing the hydrogen permeation properties. To test this hypothesis we performed calculations on a 1:1 mixed $CaTiO_3$ $SrTiO_3$ perovskite since the average $\Delta E_{OHform}$ was 0.04 eV close to the optimum. The material has previously been investigated but to our knowledge not with respect to proton conductivity. $\Delta E_{OHform}$ was calculated to ca. 0.3 eV and the proton transport frequency was determined and is plotted in Figure 4.3 **(b)** for T = 800 °C. We note that the scaling relations seem to hold for this material as well, which is predicted to have significantly higher proton flux than any of the pure materials.

To verify these results and to test the suggested mixed perovskite, a series of 12.5 % Al doped $Sr_xCa_{1-x}TiO_3$ perovskites are currently being synthesised. After synthesis the proton conductivity of the materials will be investigated using the conductivity relaxation technique whereby estimates of both mobility and concentration of the $OH_O$ defects can be obtained [158, 159]. No experiments have however been completed in time for this thesis.

Preliminary calculations of Al doped $Sr_xCa_{1-x}TiO_3$ system show that the formation energy of the hydrogen defect, scale linearly with the value of $x$ and that it is possible to adjust $x$ to match the desired value for $\Delta E_{OHform}$ (see Figure 4.4). It is however also seen that an Al doping of 12.5 % is too high, since the hydrogen formation energy is lower than the ca. -0.5 eV optimum for all values of $x$.

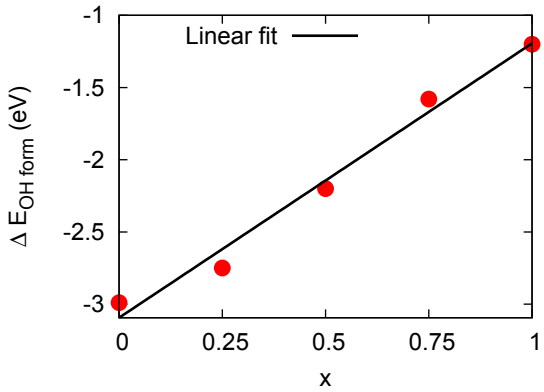


Figure 4.4: *Hydrogen defect formation energies from reaction (4.3) as function of $x$ in $Sr_xCa_{1-x}Ti_{0.875}Al_{0.125}O_3$.*

### 4.2.4 Conclusions

Based on 11 simple perovskites we performed a screening study aimed at linking simple descriptors to hydrogen diffusion rates. We found that energy barriers of diffusion and binding energy of the proton correlate strongly and we demonstrate how this may be used in predicting proton conductivities based on thermodynamic properties only. Since thermodynamic properties are significantly easier to determine than kinetic properties, this relation may be used in future screening studies.

The inverse correlation between mobility and concentration is important to empathise. It is thus not possible to have high protonic mobility and concentration simultaneously. Materials optimizing should be performed with respect to this tradeoff. We demonstrate the possibility of designing materials with optimal thermodynamic and kinetic properties by materials mixing. We investigated a 1:1 mixture of $SrTiO_3$ and $CaTiO_3$ and this material is predicted to posses a good tradeoff between mobility and protonic concentration and is currently being investigated further.

# Chapter 5

# Defect interactions

To effectively design screening studies as well as correctly interpret the obtained results, a thorough understanding of the materials and relevant defect chemistry is important.

It is generally assumed that defects interact primarily through Coulomb interactions and since most defects are charged and the Coulomb force is strong, this assumption is natural and justified. It is therefore generally accepted that defects with charge of same sign repel each other and disperse in the material. Defects of opposite charge are assumed to attract each other and exist as pairs for shorter or longer periods of time. Uncharged defects have been given little attention as they, under this assumption, do not effect the electrochemical properties of the material and further are difficult to detect. Many defect interaction studies have been published, e.g. [160, 161, 162, 163], but few attempts to obtain a more fundamental understanding of defect-defect interactions relevant to hydrogen in oxides have been made.[164]

Due to the explicit atomic modelling inherent in DFT, this method is well suited for studying defect clusters and direct insight is readily available. Here, two studies are presented targeting defect interactions and in both systems, clustering of defects with charge of same sign is observed. We explain this as result of elastic lattice interactions similar to the phononic stabilization of electronic Cooper pairs [165]. Further, defect interactions have been used to determine the most stable proton sites in Ca doped $Sm_2Sn_2O_7$ pyrochlore by comparison of DFT calculations with infrared spectra.

## 5.1 The H-H defect

### 5.1.1 Motivation

Regarding the H defect, consensus has settled that the actual diffusing species in most cases is the proton as discussed in Section 2.3.[1] Though sparsely investigated, the proton most is often assumed created via reaction between water, a structural oxygen and an oxygen vacancy through

$$H_2O(g) + O_O^x + V_O^x \rightarrow 2\ OH_O^\bullet + 2\ e'. \tag{5.1}$$

Although formed pairwise, the expected strong Coulomb repulsion and the high mobility of bulk protons, are assumed quickly to force the OH defects apart. No studies on the actual mechanism have however been published.

We studied the interaction between two hydrogen defects in perfect $SrTiO_3$ aimed at providing a thorough description of the kinetic and thermodynamic properties of interacting hydrogen defects in this well known material. The main results or our studies have been submitted to *Physical Chemistry Chemical Physics*. The article is appended as Article III.

### 5.1.2 Methods

The H-H interaction was investigated by calculating and comparing the energies of the pure $SrTiO_3$ crystal to single and double H defective systems. Although we were able to treat all possible configurations of two H in the 2×2×2 supercell, this was unsuitable for determining the thermodynamic properties. The defect interaction was too long-ranging and energies did not converge with increasing H-H separation (see Figure 5.1). The 3×3×3 supercell, being 50 % larger in each direction, was adequate for consistent thermodynamics but the increased number of possible H-H configurations prevented a complete investigation.

Due to computational expense, 2×2×2 supercells were used for the kinetic calculations and tests showed that the kinetic properties of one H in 2×2×2 and 3×3×3 supercells were almost identical. See Table 1 in Article III.

[1] See however Chapter 6

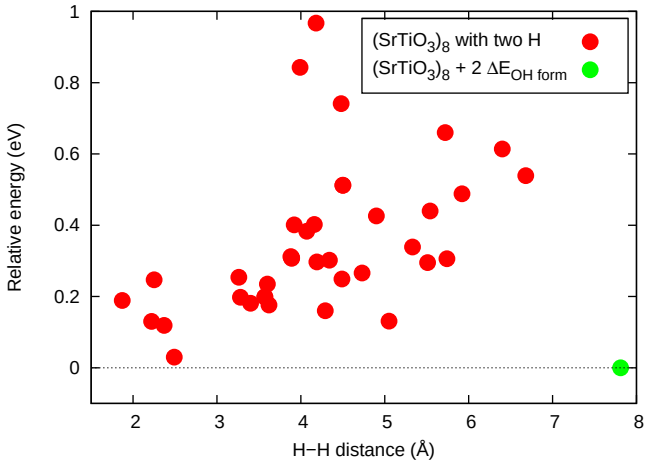


Figure 5.1: *Energy of all configurations of $(SrTiO_3)_8$ with 2 $OH_O$ defects relative to the defect free energy plus the energy of two single defects. The energy of the doubly hydrogenated system does not converge with increasing H-H separation as required.*

### 5.1.3 Results

The energies of the double hydrogen systems relative to that of two single hydrogen defects, corresponding to the reaction

$$\mathrm{H}_{single} + \mathrm{H}_{single} \rightarrow (\mathrm{H}\text{ - }\mathrm{H})_{double}, \tag{5.2}$$

were plotted as function of H-H separation showing significant stabilization of the double defect (see Figure 5.2 **(a)**). As seen from the figure, the two hydrogen defects are attracting each other and the most stable H-H distance is surprisingly small (ca. 2.3 Å). See Figure 3 in Article III.

To investigate the nature of the apparent attraction, static lattice calculations were performed (see Figure 5.2 **(b)**). In this case no attractive interaction was found and we conclude that the repulsive electrostatic potential of the hydrogen ions is smaller than the attractive elastic interaction resulting from lattice deformation. This lead to an overall attractive interaction. This is similar to the attractive interaction responsible for electronic Cooper pairs which are stabilized by electron-phonon interactions.[165]

For a given diffusional path to be important, two requirements must be met: The population of the involved conformations must be high and the activation barriers between these conformations must be low. A complete investigation on the mobility of the double defect was impossible, but

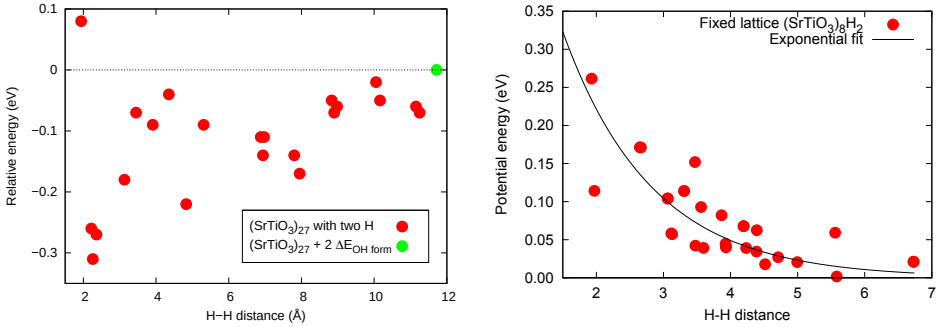


**(a)** **(b)**

Figure 5.2: *Energy of the double hydrogen defective systems as function of hydrogen separation. All internal degrees of freedom are relaxed in figure* **(a)** *while the lattice is kept fixed in* **(b)**. *The figures thus separate lattice effects from electrostatic effects.*

two diffusional paths of particular low energy were investigated. Besides involving low energy conformations, the two paths were relatively simple involving just 6 and 8 elementary jumps and rotations and are the most probable pathways. These are illustrated in Figure 4 in Article III. The following NEB and TST calculations showed that at moderate to high temperatures, single and double defects have comparable mobilities. At lower temperatures the single defects are noticeably less mobile due to slightly higher activation barriers (see Figures 5 and 6 in Article III).

Even though Figure 5.2 **(a)** clearly shows that a double defect is more stable than a two isolated defects this is without including entropic effects. Both vibrational end configurational effects were estimated and shown to have a significant impact on the thermodynamics leading to destabilization of the double defect at temperatures beyond 300 - 400 °C, i.e. reversing reaction (5.2).

According to reaction (5.1), protonic defects are created together and due to the short permeation time of an operating membrane these will contribute to the total flux, even though destabilized by entropy. The importance of the double defect was estimated using a simple random diffusion model and counting the number of jumps the double defect would perform before breakup into two defects. The results are shown in Figure 5.3.

At elevated temperatures the double defect exists just a few hundred jumps and will only be found near the high pressure side of the membrane where it has been created. At lower temperatures the lifetime of the double

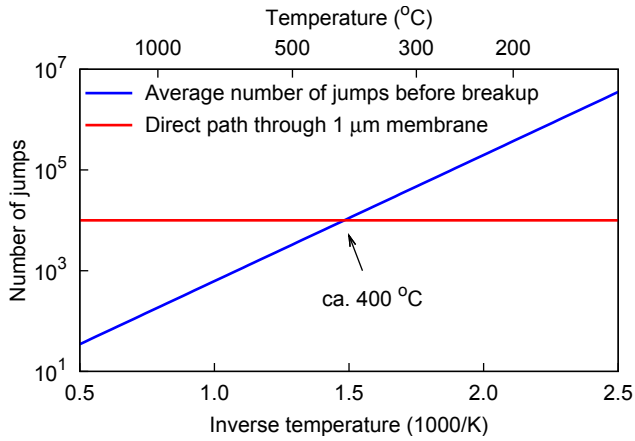


Figure 5.3: *Plot of stability of the double H defect towards thermal breakup. The number of jumps before breakup are plotted of function of temperature. The number of jumps required to diffuse directly through a 1 μm membrane are illustrated for comparison.*

defect increase and at ca. 400 °C the average double H lives long enough to permeate a 1 $\mu$m thick membrane, corresponding to current benchmark thicknesses.[166]

### 5.1.4 Conclusions

The investigation of the interaction between hydrogen defects revealed that a net attraction is present. The attractive force is exclusively a lattice effect since static lattice calculations show a net Coulomb repulsion consistent with previous assumptions.

The double defect can diffuse as an whole and two paths were investigated. Both were more efficient for hydrogen diffusion than the single hydrogen diffusion paths, although the differences were small at usual operating temperatures.

Despite being stabilized at low temperatures, the low concentration of hydrogen defects significantly destabilize the double defects due to configurational entropy. Should the double defect break up e.g. due to thermal fluctuations, the probability of recombining is negligible. However, since the defects are created together, the double defect will exist for some time after membrane penetration and a simple model showed that at temperatures lower than 400 °C, the double defect will dominate the total flux.

We conclude that double H defects further should be investigated both

experimentally and theoretically since the role of these may be important for designing novel materials and understanding experimental results.

## 5.2 The pyrochlore system

### 5.2.1 Motivation

Even though interaction between hydrogen defects may be important, it is clear that interaction between hydrogen and other defects are predominant in usual experimental setups where samples are thicker and dopants are present. As a result of collaboration with Dr. K. Eurenius from the University of Tokyo and Dr. C. Knee from the University of Gothenburg, the defect structures and interactions in Ca doped $Sm_2Sn_2O_7$ pyrochlore were investigated. Many pyrochlores are promising candidates for solid state proton conducting membranes,[167, 168] and the main results have been submitted to *Solid State Ionics*. The article is appended as Article IV.

The OH vibrational frequency is well suited for probing the local structure around the OH defect due to the sharpness of the peak and even minor changes in the local environment are readily observable. Assigning particular peaks to particular conformations has previously been attempted based on empirical relations between O-H and O-O distances,[169] but using DFT, results of much better quality have been achieved.[170, 171]

A Fourier transform infrared spectrum of protonated $Sm_{1.92}Ca_{0.08}Sn_2O_{7-\delta}$, shown in Figure 5.4 **(b)** clearly showing the several distinct OH peaks suggesting several occupied protonic sites. Further evidence is the shifting of the peaks upon deuteration (Figure 5.4 **(a)**). The ratio between the peaks of ∼1.35 is close to the theoretical isotopic ratio of ∼1.38.[54]

### 5.2.2 Results

Many possible conformations of Ca dopant, oxygen vacancy and proton were examined. Both the oxygen vacancy and proton were found attracted by the Ca dopant as expected due to their charges, and the dopant-dopant distances were ca. 3.5 and 2.5 Å respectively (see Figures 1 and 3 in Article IV). Including all three defects in the same system, no repulsive interaction was found (see Figure 2 in Article IV). Since the net charge on the Ca dopant and oxygen vacancy is similar to the charge on the $OH_O$ defect[2] the stabilization could not be explained by Coulomb interaction. In stead,

[2]See also Chapter 6

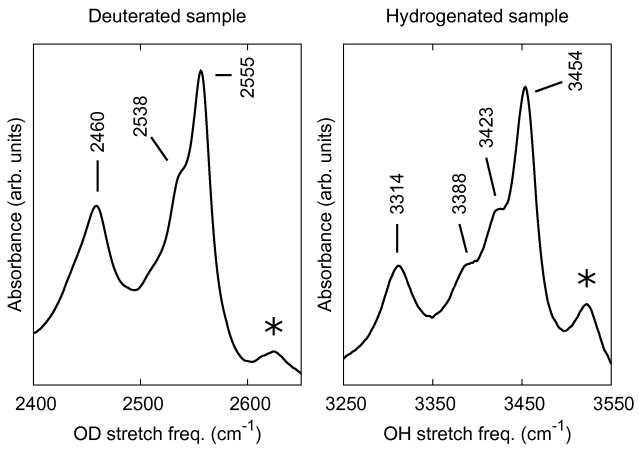


Figure 5.4: *Infrared absorbance spectra of* $Sm_{1.92}Ca_{0.08}Sn_2O_{7-\delta}$. $*$ *indicate modes not linked to O-H/O-D vibrations. The ratios between the corresponding OH and OD frequencies are as expected close of 1.38. Data from Ref. [172].*

similar to the stabilization of the double H defect, elastic lattice effects were the cause of attraction.

The vibrational frequencies and intensities of the most stable conformations were hereafter calculated. From the data in Table 5.1 it is clear that the main peaks at 3454 and 3314 $cm^{-1}$ can be attributed to the two most stable structures in the Ca doped system. Both the magnitude of the

Table 5.1: *Calculated intensities (at 300 °C) and OH stretch frequencies (in* $cm^{-1}$*) of the most stable proton sites. See Article IV for full table caption.*

| Defect structure | Int.$_{DFT}$ | $\nu_{DFT}$ | Int.$_{FTIR}$ | $\nu_{FTIR}$ |
|---|---|---|---|---|
| Undoped $OH_O$ | $\sim 0$ | 3350 | - | - |
| $Ca_{Sm}OH(1)_O$ | 73 % | 3463 | 65 - 70 % | 3454 |
| $Ca_{Sm}OH(2)_O$ | 27 % | 3322 | 30 - 35 % | 3314 |
| $Ca_{Sm}OH(3)_O$ | $< 1$ % | 3262 | - | - |
| $Ca_{Sm}OH(4)_O$ | $< 1$ % | 3331 | ($< 3$ %) | (3388) |
| $Ca_{Sm}V_OOH_O$ | $\sim 0$ | 3290 | - | - |
| $Ca_{Sm}V_OOH_O$ | $\sim 0$ | 4131 | - | - |

frequencies as well as the intensities of the peaks were in accordance with this assignment.

### 5.2.3 Conclusions

By combining DFT and spectroscopy, we were able to determine the structure of Ca doped $Sm_2Sn_2O_7$ under assumed working conditions. The structures were in all cases stabilized by defect-defect interactions in accordance with our previous results. The OH stretch frequencies for the most stable protonic sites were calculated and were in good agreement with the main peaks of the spectrum, with respect to both frequency and intensity.

# Chapter 6

# Charge analysis

## 6.1 Motivation

The electronic transport properties of a proton conducting material are imporitaint since these determine the application. Models for electronic transport properties were however not avaliable until late is this work and were therefore not utilized. In stead we studied the atomic charge distributions of several systems with good results which has yielded some information about the electronic response to ionic diffusion as well as describing the local charge density around the OH defect.

Hydrogenic defects in oxides are most commonly thought of as protons or hydroxides, but other charges are possible. Hydrides have been suggested e.g. in mayenite ($Ca_{12}Al_{14}O_{33}$), $SiO_2$, ZnO and MgO,[173, 174, 175] and recently an apparent hydride conductivity in several doped and undoped oxides has been measured.[176, 177, 178, 179] Even the existence of nascent uncharged H has been suggested.[175, 180]

Although atomic charge is not an observable, it is a practical and well recognised tool for predicting structures and properties within solid state chemistry. With the advances of electronic structure methods e.g. DFT, predicting atomic charges based on the electronic density has become possible and offer improved flexibility compared to predictions based on the periodic table.

Using the Bader charge analysis, the atomic charges of the $OH_O$, H-H and $H_O$ defects have been investigated and will be discussed in the following. The results concerning the $OH_O$ defect have been submitted to *Journal of Applied Physics*, appended as Article V, while results concerning the $H_O$ defect are included in Article IV.

Table 6.1: *Bader charges on H in OH in various materials (a.u.). † denote data from this study.*

| Solid oxide | $SrTiO_3$ | $BaNbO_3$ | $CaTiO_3$ | $SrZrO_3$ |
|---|---|---|---|---|
| Charge on H | $0.56^{\dagger}$ | $0.54^{\dagger}$ | $0.57^{\dagger}$ | $0.60^{\dagger}$ |
| Molecule | $H_2O$ | $H_2O_2$ | HCOOH | $CH_3COOH$ |
| Charge on H | 0.567[135] | 0.547[182] | 0.580[183] | 0.579[183] |

## 6.2 Methods

The known issue of most GGA functionals of over-delocalizing the electronic density was a possible problem, since the Bader charge analysis is dependent on an accurate description of the electronic density. Since the LDA+U method has been developed to target this (see section 3.3.3), this was natural to apply as test of the validity of the GGA results. LDA+U calculations are computationally more demanding and GGA has therefore been selected as the primary functional so that the charge development during OH rotations and H jumps could be followed closely.

Determining an appropriate value for the U parameter is easily done if the band gap is known. The indirect band gap for $SrTiO_3$ is experimentally known to 3.2 eV,[181] but the PBE functional yield a value of just 1.7 eV. Upon increasing values for U, the calculated band gap increase approximately linearly. The 3.2 eV band gap is obtained with U = 8.5 eV, which is considered as the most accurate choise for the present purpose.

## 6.3 Results

### The OH defect

Singly protonated structures of $SrTiO_3$, $BaNbO_3$, $CaTiO_3$ and $SrZrO_3$ were relaxed and the atomic Bader charges determined using PBE (see Table 6.1). In the case of $SrTiO_3$ the results were tested using LDA+U, but no significant discrepancies were found. The charges on the hydrogenic species were determined to ca. 0.56 $e$ differing significantly from the integer charges often assumed, but similar to hydrogen charges in molecules.

It was evident that the electron and proton originating from the hydrogen not are completely dissociated but that the proton associate the largest part of the added electron. Further, it was clear that the closest oxygen was attracting a large part of the remaining electron density. Adding the

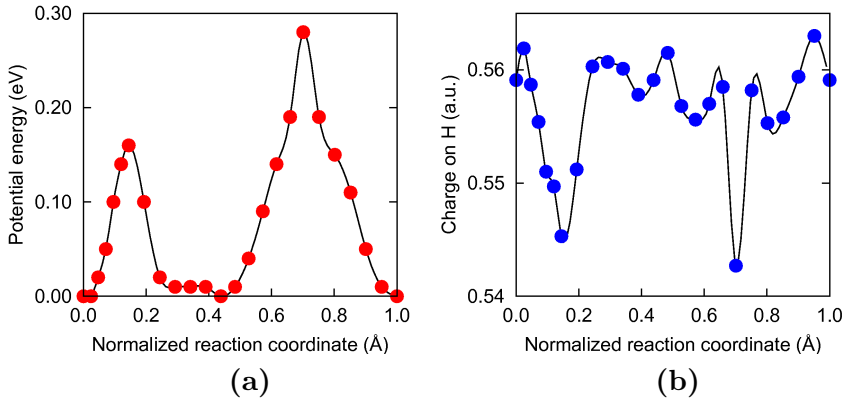


Figure 6.1: **(a)** *Potential energy of OH rotation and H jump.* **(b)** *Hydrogenic Bader charges during OH rotation and H jump. In both figures, points indicate NEB images.*

charges we found that the OH defect was best described as $\mathrm{OH}_{\mathrm{O}}^{0.50\bullet}$ and the formation of the defect occurring through

$$\mathrm{H_2O}(g) + 2\ \mathrm{O}_{\mathrm{O}}^{x} \rightarrow 2\ \mathrm{OH}_{\mathrm{O}}^{0.50\bullet} + e^{-} + 1/2\ \mathrm{O_2}(g). \tag{2}$$

The remaining 0.5 $e$ electron density was distributed amongst the remaining atoms decaying exponentially from the proton (see Figure 1 in Article V).

We further investigated the charge of the hydrogen during two processes of interest, namely OH vibration and H diffusion. We found that the hydrogenic charges vary by ca. 15 to 20 % during ground state and first excited state OH vibrations, but the majority of the charge is transferred to and from the nearest oxygen. The charge on the OH defect is thus very stable at $(0.50 \pm 0.01)\ e$.

During diffusion changes in hydrogenic charges are of similar magnitude. As seen from Figure 6.1 charges are 2-3 % lowered at the transition states, but at no point is a "naked" proton found.

### The H-H defect

The proposed H-H defect was investigated in the same manner both in the most stable conformation and during diffusion. It was found that the introduction of the second hydrogen only has a small effect on the hydrogenic charges. The charge of the moving H were lowered by up to 6 % at the transition states while the charge on the stationary H was negligibly affected (see Figure 6.2).

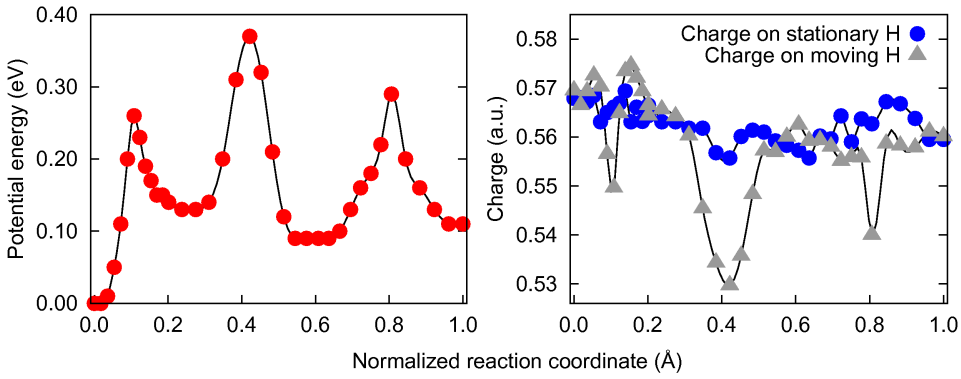


Figure 6.2: **(a)** *Potential energy surface of the "6 step path" double H diffusion (see Figure 4 in Article III).* **(b)** *Bader charges on the moving and stationary H. In both figures, points indicate NEB images.*

### The $H_O$ defect

During the investigation of the Ca doped $Sm_2Sn_2O_7$ structure the $H_O$ defect was found. See Figure 6.3. This has previously been suggested at candidate for non-protonic H sites. We determined the Bader charge of this species to -0.44 $e$ confirming the negative charge.

Although the defect is unstable in the vicinity of a dopant, it is stabilized by ca. 0.70 eV compared to isolated OH and $v_O$ defects, i.e.

$$OH_O + V_O \longrightarrow O_O + H_O. \tag{6.1}$$

These results are thus in accordance with experiments, finding hydrides at high temperatures and at reducing conditions [178, 179]. These conditions lead to increasing concentration of lone oxygen vacancies, a prerequisite for $H_O$ formation.

Although the discovery of the negatively charged H defect in an oxide is interesting, no transport mechanism has been investigated. Therefore, we are unable to tell whether the experimentally observed hydride conductivity is a result of this defect and thereby solve the discrepancy.

## 6.4 Conclusions

The Bader charge analysis method has been applied to several of the systems investigated in this thesis. We find significant differences between

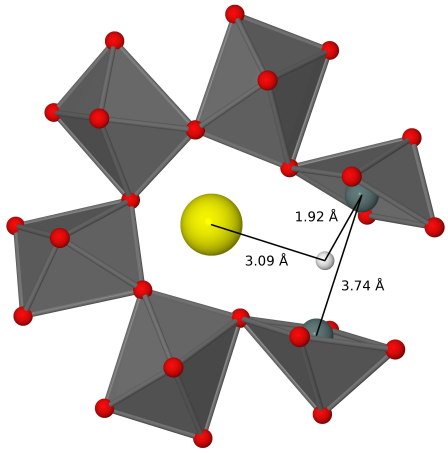


Figure 6.3: *Most stable conformation of a proton and an oxygen vacancy in $Sm_2Sn_2O_7$. The Sn-H bonds are 1.92 Å in comparison with normal Sn-O distances of ca. 2.1 Å. The charge on the $H_O$ species is -0.44 e. Sm: Yellow, Sn: Grey (inside octahedra), O: Red, H: White.*

the Bader obtained results and the usual integer charges usually used for prediction of the defect structure of materials.

In most cases we find the proton associated with ca. (0.45±0.02) $e$ of electronic charge suggesting a $H^{0.55\bullet}$ species, but extra charge on the host oxygen leads to a $OH^{0.5\bullet}$ defect.

During vibration and diffusion, the charge varies a few percent. The results have been reproduced in other OH containing systems as well as for the double H defect. The H/ OH defects are thus at all times closely associated with ca. 0.5 $e$ electronic density and we conclude that the charge properties of the H/OH defect, almost exclusively are determined by the bond to the oxygen. This is in accordance with the general picture of a proton deeply imbedded in the electron cloud of the oxygen. The $OH_O$ defect is found to greatly resemble the OH functional group in $H_2O$ and $H_2O_2$.

The $H_O$ defect is very different with a negative charge of - 0.44 $e$. The expected concentration is however neglible, except at extremely reducing conditions.

# Chapter 7

# Summary and outlook

## 7.1 Summary

In the last decades, proton conducting oxides have received increasing attention due to the possibility of applying proton conductors as electrolytes in fuel cells or as gas separation membranes. Motivated by increased fuel efficiency and reduced materials cost, an impressive amount of studies have been published, but no solid oxide proton conductor has yet been introduced commercially, mainly due to too low protonic fluxes.

A major hindrance for the continued research towards improved hydrogen permeation properties of oxides is the lack of a thorough understanding of the atomic scale dynamics and interactions which govern and limit the protonic conductivity. Although much has been learned from experimental work, the progress of *ab initio* modelling has enabled a much more direct insight into the physical interactions at play. With the explicit atomic modelling, focusing on specific structures and properties is possible in contrast to experimental results which often reflect an average of many different effects.

Materials screening has been an acknowledged technique for centuries, but with the advances of precise theoretical models, computational screening has become increasingly useful. Two successful screening studies have been presented. The possibility of using model structures and hereby being able to screen a large number of materials has been demonstrated and used to predict novel material for solid state hydrogen storage. Further, the correlated nature of kinetic and thermodynamic properties has been demonstrated and an optimum trade-off between H mobility and H concentration in oxides was identified. The mixed perovskite $Sr_{0.5}Ca_{0.5}TiO_3$

was determined as a promising candidate with respect to this trade-off.

To successfully conduct reliable screening studies, a thorough understanding of the physics and chemistry of the materials is essential. We have studied the effects of defect-defect interactions in perovskites and pyrochlores focusing mainly on the interaction between H and other defects commonly present in oxides. We found that two H defects, despite the Coulomb repulsion, could form several stable complexes and further that the double H defect was mobile. The cause of the attractive potential was elastic lattice deformations in the vicinity of one H defect facilitating a second H defect. Although thermally destabilized by entropy, the double H defect will contribute significantly to the total hydrogen flux at ambient temperatures. In this study we determined the effective H charge as ca. $+0.25$ $e$, in contrast the $+1$ $e$ charge usually assumed.

Motivated by this discrepancy we investigated a series of systems using the Bader charge analysis determining the OH defect as a ca. 0.5 $e$ charged species. During OH vibration or diffusion the charge may vary a few percent, but no indications of a "naked" proton have been found. Several systems were investigated but the general results were identical. The investigated systems include solid oxides and molecules. The $H_O$ defect was the only exception with a charge of -0.44 $e$.

Finally, we have demonstrated the possibility of combining experimental and theoretical studies with good results. The local environment of the H defect in Ca doped $Sm_2Sn_2O_7$ was probed by FTIR spectroscopy, and the observed peaks were assigned to actual H sites using DFT. We were able to reproduce the magnitude of the frequencies, the peak spacing as well as relative intensities. The most stable defect structures have thereby been determined with high certainty.

## 7.2 Outlook

The presented results have several possible applications with the general purpose of providing insight into the defect chemistry of oxides. Computational screening a large number of different structures and materials has successfully been applied in many systems, but not previously related to protonic conduction. We demonstrate the possibility of applying this technique to proton conduction oxides whereby novel materials or useful trends may be discovered.

$Sr_{0.5}Ca_{0.5}TiO_3$ is suggested as a promising proton conductor due to the well balanced trade-off between H concentration and mobility. Even

though several studies of $Sr_xCa_{1-x}TiO_3$ type materials have been published, no compositions have been tested with respect to proton conductivity. Currently such studies are being performed at Risø DTU, using the conductivity relaxation technique.

Further, the properties of the double H defect are important to understand as this may constitute a significant amount of the total hydrogen flux through a membrane. As previously proposed, the combined dynamics of two H defects may be important in escaping the trapping effect of dopants.[61] Due to the short lifetime of this defect, experiments must be carefully designed with micrometer samples at relatively low temperatures ($< 500$ °C). Also further DFT studies of the double H defect near the surface and near dopants should be conducted as well as studies of the interaction between 3 or more hydrogen.

More research into the electronic properties of H defects are necessary. Even though the continued use of notations such as $H^\bullet$ and $OH^\bullet$ may be useful, the explicit reference to protons may be unfortunate if students or scientists are not aware that the actual species is not a proton. The actual species is greatly resembling OH in other systems e.g. $H_2O$. Our results suggest a species charged by ca. 0.5 $e$, which is unchanged during diffusion. This should not be mistaken for correlated ionic-electronic transport.

*Ab initio* methods have during the last century developed from being a formalism for studying the fundamental nature of matter to a practical and reliable tool in applied sciences. Despite the long history, development is far from terminated and methods such as DFT+U, van der Waals functionals or self interaction correction are likely to be standard in the near future. Hereby errors and uncertainties are futher minizised with increased accurace and insight as consequence.

Investigation of the electronic transport properties of proton conductors is essential to differentiate material optimization towards electrical insulators or conductors depending on application. Presently, advances in electronic transport theory are rapid and new implementations are emerging [184]. Since no implementation was available until late in this work, such studies have not been conducted. *Ab initio* studies of electronic transport are likely to provide significant new insight and should be focused upon in future studies.

# Bibliography


[1] A.D. Pasternak. Global energy futures and human development: a framework for analysis. *University of California, Lawrence Livermore National Laboratory UCRL-ID-140773. Washington, DC: US DOE*, 2000.

[2] S.G. Benka. Special Issue The Energy Challenge. *Physics Today*, 55:38, 2002.

[3] M. King Hubbert. Nuclear Energy and the Fossil Fuels. *American Petroleum Institute & Shell Development Co.*, (95):9–11 and 21–22, 1956.

[4] C.J. Campbell and J.H. Laherrère. The end of cheap oil. *Scientific American*, 278(3):60–5, 1998.

[5] J. Chow, R.J. Kopp, and P.R. Portney. Energy resources and global development. *Science*, 302(5650):1528, 2003.

[6] S. Solomon, D. Qin, M. Manning, Z. Chen, M. Marquis, K.B. Averyt, M. Tignor, and H.L. Miller. *Climate Change 2007: The Physical Science Basis*. Cambridge University Press, 2007.

[7] S. Jacobsson and A. Bergek. Transforming the energy sector: The evolution of technological systems in renewable energy technology. *Industrial and Corporate Change*, 13(5):815, 2004.

[8] R.F. Service. The Hydrogen Backlash. *Science*, 305:958–961, 2004.

[9] G. Nazri and G. Pistoia. *Lithium Batteries: science and technology*. Springer Netherlands, 2004.

[10] L. Schlapbach and A. Züttel. Hydrogen-storage materials for mobile applications. *Nature*, 414(6861):353–358, 2001.

[11] D.J. Wilhelm, D.R. Simbeck, A.D. Karp, and R.L. Dickenson. Syngas production for gas-to-liquids applications: technologies, issues and outlook. *Fuel processing technology*, 71(1-3):139–148, 2001.

[12] R.J. Smith, M. Loganathan, and M.S. Shantha. A Review of the Water Gas Shift Reaction Kinetics. *International Journal of Chemical Reactor Engineering*, 8(8):4, 2010.

[13] B. Norden, A. Frster, D. Vu-Hoang, F. Marcelis, N. Springer, and I. Le Nir. Lithological and petrophysical core-log interpretation in $CO_2$SINK, the European onshore research storage and verification project. *SPE Reservoir Evaluation Engineering*, pages 179–192, 2010.

[14] S.D. Ebbesen, C. Graves, and M. Mogensen. Production of Synthetic Fuels by Co-Electrolysis of Steam and Carbon Dioxide. *International Journal of Green Energy*, 6(6):646–660, 2009.

[15] J.M. Christensen, P.M. Mortensen, R. Trane, P.A. Jensen, and A.D. Jensen. Effects of $H_2S$ and process conditions in the synthesis of mixed alcohols from syngas over alkali promoted cobalt-molybdenum sulfide. *Applied Catalysis A: General*, 366(1):29–43, 2009.

[16] See e.g. "freedomcar and fuel technical partnership technical goals" at http://www1.eere.energy.gov/vehiclesandfuels/about/partnerships/ freedomcar/fc_goals.html#4.

[17] B. Sakintuna, F. Lamari-Darkrim, and M. Hirscher. Metal hydride materials for solid hydrogen storage: a review. *International Journal of Hydrogen Energy*, 32(9):1121–1140, 2007.

[18] F. Barbir. PEM fuel cells. *Fuel Cell Technology*, pages 27–51, 2006.

[19] K.A. Mauritz and R.B. Moore. State of understanding of Nafion. *Chem. Rev*, 104(10):4535–4586, 2004.

[20] A.B. Stambouli and E. Traversa. Solid oxide fuel cells (SOFCs): a review of an environmentally clean and efficient source of energy. *Renewable and Sustainable Energy Reviews*, 6(5):433–455, 2002.

[21] M. Mogensen and K. Kammer. Conversion of Hydrocarbons in Solid Oxide Fuel Cells. *Annual Review of Materials Research*, 33(1):321–331, 2003.

[22] J. Larminie, A. Dicks, and M.S. McDonald. Fuel cell systems explained. 2003.

[23] K.D. Kreuer. Proton-conducting oxides. *Annual Review of Materials Research*, 33:333–359, 2003.

[24] H. Iwahara, Y. Asakura, K. Katahira, and M. Tanaka. Prospect of hydrogen technology using proton-conducting ceramics. *Solid State Ionics*, 168(3-4):299–310, 2004.

[25] Illustration from http://www.nfcrc.uci.edu.

[26] Y. Nagahara, S. Sugawara, and K. Shinohara. The impact of air contaminants on PEMFC performance and durability. *Journal of Power Sources*, 183:422–428, 2008.

[27] S.C.A. Kluiters. Status review on membrane systems for hydrogen separation. *Energy Center of the Netherlands, Petten, The Netherlands*, 2004.

[28] N.W. Ockwig and T.M. Nenoff. Membranes for hydrogen separation. *Chem. Rev*, 107(10):4078–4110, 2007.

[29] S. Adhikari and S. Fernando. Hydrogen membrane separation techniques. *Ind. Eng. Chem. Res*, 45(3):875–881, 2006.

[30] M. Le Digabel, D. Ducret, C. Laquerbe, P. Perriat, and J.C. Niepce. Application of gas separation membranes to detritiation systems. *Desalination*, 148(1-3):297–302, 2002.

[31] H. Schmalzried. The Advent of Solid-State Thermodynamics, Kinetics and Electrochemistry in the 20'th Century. *Z. Phys. Chem*, 218:1385–1399, 2004.

[32] F.W. Poulsen. Doctoral Dissertation: Methods and limitations in defect chemistry modelling. 2007.

[33] A.M. Stoneham. The theory of defects in solids. *Contemporary Physics*, 20(5):535–545, 1979.

[34] D.M. Smyth. *The defect chemistry of metal oxides.* Oxford University Press.

[35] P. Kofstad and T. Norby. *Defects and Transport in Crystalline Solids.* University of Olso, 2007.

[36] K. Sasaki, J. Claus, and J. Maier. Defect chemistry of oxides in partially frozen-in states: case studies for $ZrO_2$ ($Y2O_3$), $SrZrO_3$ ($Y2O_3$), and $SrTiO_3$. *Solid State Ionics*, 121(1):51–60, 1999.

[37] K. Sasaki and J. Maier. Low-temperature defect chemistry of oxides. I. General aspects and numerical calculations. *Journal of Applied Physics*, 86:5422, 1999.

[38] K. Sasaki and J. Maier. Low-temperature defect chemistry of oxides. II. Analytical relations. *Journal of Applied Physics*, 86:5434, 1999.

[39] F.A. Kröger and H.J. Vink. *in Solid State Physics, Vol. 3.* Academic Press, New York, 1956.

[40] H. Iwahara, T. Esaka, H. Uchida, and N. Maeda. Proton conduction in sintered oxides and its application to steam electrolysis for hydrogen production. *Solid State Ionics*, 3:359–363, 1981.

[41] E. V. Monakhov, A. Yu Kuznetsov, and B. G. Svensson. Zinc oxide: bulk growth, role of hydrogen and schottky diodes. *J. Phys. D*, 42:153001, 2009.

[42] T. Omura. Review - hydrogen embrittlement of steel in corrosive environments and high-pressure gaseous hydrogen environments. *Corr. Eng.*, 58(4):130–136, 2009.

[43] A.T.M. Van Gogh, E.S. Kooij, and R. Griessen. Isotope Effects in Switchable Metal-Hydride Mirrors. *Phys. Rev. Lett.*, 83(22):4614–4617, 1999.

[44] A. Remhof and A. Borgschulte. Thin-Film Metal Hydrides. *ChemPhysChem*, 9(17):2440–2455, 2008.

[45] D.G. Thomas and J.J. Lander. Hydrogen as a donor in zinc oxide. *Journal of Chemical Physics*, 25:1136–1142, 1956.

[46] H. Iwahara, H. Uchida, and N. Maeda. High temperature fuel and steam electrolysis cells using proton conductive solid electrolytes. *Journal of Power Sources*, 7(3):293–301, 1982.

[47] P.W. Atkins. *Physical chemistry 4'th ed.* Cambridge University Press, 1990.

[48] T. Norby and N. Christiansen. Proton conduction in Ca-and Sr-substituted $LaPO_4$. *Solid State Ionics*, 77:240–243, 1995.

[49] S. Kim, K.H. Lee, and H.L. Lee. Proton conduction in $La_{0.6}Ba_{0.4}ScO_{2.8}$ cubic perovskite. *Solid state ionics*, 144(1-2):109–115, 2001.

[50] N. Bork, M. Chen, and F.W. Poulsen. Modelling of oxides for use in high temperature fuel cells. *part of: Energy Materials. Advances in Characterization, Modelling and Application, Proceedings (ISBN: 978-87-550-3694-9)Forskningscenter Risø, Roskilde*, 2008.

[51] C.N. Huang, J.S. Bow, Y. Zheng, S.Y. Chen, N.J. Ho, and P. Shen. Nonstoichiometric Titanium Oxides via Pulsed Laser Ablation in Water. *Nanoscale Research Letters*, pages 1–14, 2010.

[52] G. Weber, S. Kapphan, and M. Wöhlecke. Spectroscopy of the O-H and O-D stretching vibrations in $SrTiO_3$ under applied electric field and uniaxial stress. *Physical Review B*, 34(12):8406–8417, 1986.

[53] T.S. Bjørheim, A. Kuwabara, I. Ahmed, R. Haugsrud, S. Stølen, and T. Norby. A combined conductivity and DFT study of protons in $PbZrO_3$ and alkaline earth zirconate perovskites. *Solid State Ionics*, 181(3-4):130–137, 2010.

[54] M. Glerup, F.W. Poulsen, and R.W. Berg. Vibrational spectroscopy on protons and deuterons in proton conducting perovskites. *Solid State Ionics*, 148(1-2):83–92, 2002.

[55] W. Münch, K.D. Kreuer, G. Seifert, and J. Majer. A quantum molecular dynamics study of proton diffusion in $SrTiO_3$ and $CaTiO_3$. *Solid State Ionics*, 125(1-4):39–46, 1999.

[56] M.S. Islam. Computer modelling of defects and transport in perovskite oxides. *Solid State Ionics*, 154:75–85, 2002.

[57] S. Klauer and M. Wöhlecke. Incorporation of hydrogen in cubic and uniaxial oxidic crystals deduced from polarized Raman scattering. *Physical Review B*, 49(1):158–181, 1994.

[58] N. Sata, K. Hiramoto, M. Ishigame, S. Hosoya, N. Niimura, and S. Shin. Site identification of protons in SrTiO_ {3}: Mechanism for large protonic conduction. *Physical Review B*, 54(22):15795–15799, 1996.

[59] S. Aggarwal, S.R. Perusse, C.W. Tipton, R. Ramesh, H.D. Drew, T. Venkatesan, D.B. Romero, V.B. Podobedov, and A. Weber. Effect of hydrogen on Pb(Zr,Ti)$O_3$-based ferroelectric capacitors. *Applied Physics Letters*, 73:1973, 1998.

[60] H. Yukawa, K. Nakatsuka, and M. Morinaga. Electronic structures of hydrogen in perovskite-type oxide, $SrTiO_3$. *Solid state ionics*, 116(1-2):89–98, 1999.

[61] M. Björketun. *Hydrogen in oxides: a densityfunctional study of thermodynamic and kinetic aspects*. PhD thesis, Chalmers University of Technology, 2007.

[62] M.E. Björketun, P.G. Sundell, and G. Wahnström. Effect of acceptor dopants on the proton mobility in $BaZrO_3$: A density functional investigation. *Physical Review B*, 76:054307, 2007.

[63] R.D. Shannon. Revised effective ionic radii and systematic studies of interatomic distances in halides and chalcogenides. *Acta Crystallographica Section A: Crystal Physics, Diffraction, Theoretical and General Crystallography*, 32(5):751–767, 1976.

[64] K.D. Kreuer, A. Rabenau, and W. Weppner. Vehicle mechanism, a new model for the interpretation of the conductivity of fast proton conductors. *Angewandte Chemie International Edition in English*, 21(3):208–209, 1982.

[65] V.P. Gorelov, V.B. Balakireva, and N.V. Sharova. Proton-oxygen Conductance in Substituted Perovskites $A\mathrm{Ti}_{0.95}M_{0.05}\mathrm{O}_{3-\alpha}$ ($A$= Ca, Sr, Ba; $M$= Sc, Mg) in the Reducing Hydrogen-Containing Atmospheres. *Èlektrohimiâ*, 35(4):438–444, 1999.

[66] T. Norby and P. Kofstad. Proton and native-ion conductivities in $Y_2O_3$ at high temperatures. *Solid State Ionics*, 20:169–184, 1986.

[67] K.D. Kreuer. Proton Conductivity: Materials and Applications. *Chemistry of materials*, 8:610–641, 1996.

[68] M.S. Islam, R.A. Davies, and J.D. Gale. Hop, skip or jump? Proton transport in the $CaZrO_3$ perovskite oxide. *Chemical Communications*, 2001(7):661–662, 2001.

[69] W. Münch, G. Seifert, K.D. Kreuer, and J. Maier. A quantum molecular dynamics study of proton conduction phenomena in $BaCeO_3$. *Solid State Ionics*, 86:647–652, 1996.

[70] K.S. Knight and N. Bonanos. The crystal structures of some doped and undoped alkaline earth cerate perovskites. *Materials Research Bulletin*, 30(3):347–356, 1995.

[71] N. Ishizawa, T. Miyata, I. Minato, F. Marumo, and S. Iwai. A structural investigation of $\alpha$-$Al_2O_3$ at 2170 K. *Acta Crystallographica Section B: Structural Crystallography and Crystal Chemistry*, 36(2):228–230, 1980.

[72] S.K. Mohapatra, S.K. Tiku, and F. Kröger. Defect structure of unintentionally doped Alpha-$Al_2O_3$ crystals. *Journal of the American Ceramic Society*, 62(1):50–57, 1979.

[73] W.H. Flygare and R.A. Huggins. Theory of ionic transport in crystallographic tunnels. *Journal of Physics and Chemistry of Solids*, 34(7):1199–1204, 1973.

[74] O.B. Ajayi, L.E. Nagel, I.D. Raistrick, and R.A. Huggins. Calculation of motional activation energies for interstitial ions in the rutile structure using a minimum energy path model. *Journal of Physics and Chemistry of Solids*, 37(2):167–172, 1976.

[75] A. Mitsui, M. Miyayama, and H. Yanagida. Evaluation of the activation energy for proton conduction in perovskite-type oxides. *Solid State Ionics*, 22:213–217, 1987.

[76] C.R.A. Catlow and G.D. Price. Computer modelling of solid-state inorganic materials. *Nature*, 347(6290):243–248, 1990.

[77] M. Cherry, M.S. Islam, and C.R.A. Catlow. Oxygen ion migration in perovskite-type oxides. *Journal of Solid State Chemistry*, 118(1):125–132, 1995.

[78] M. Cherry, M.S. Islam, J.D. Gale, and C.R.A. Catlow. Computational studies of proton migration in perovskite oxides. *Solid state ionics*, 77:207–209, 1995.

[79] K.D. Kreuer, S. Adams, W. Münch, A. Fuchs, U. Klock, and J. Maier. Proton conducting alkaline earth zirconates and titanates for high drain electrochemical applications. *Solid State Ionics*, 145(1-4):295–306, 2001.

[80] W. Münch, K.D. Kreuer, G. Seifert, and J. Maier. Proton diffusion in perovskites: comparison between $BaCeO_3$, $BaZrO_3$, $SrTiO_3$, and $CaTiO_3$ using quantum molecular dynamics. *Solid State Ionics*, 136:183–189, 2000.

[81] M.S. Islam. Ionic transport in $ABO_3$ perovskite oxides: a computer modelling tour. *Journal of Materials Chemistry*, 10(4):1027–1038, 2000.

[82] P.G. Sundell, M.E. Bjorketun, and G. Wahnstrom. Structure, structural phase transitions, mechanical properties, defects-Thermodynamics of doping vacancy formation in $BaZrO_3$ perovskite oxide from density functional calculations. *Physical Review-Section B-Condensed Matter*, 73(10):104112–104112, 2006.

[83] M. Saiful Islam, A.R. Davies, and J.D. Gale. Proton migration and defect interactions in the $CaZrO_3$ orthorhombic perovskite : A quantum mechanical study. *Chemistry of materials*, 13:2049–2055, 2001.

[84] A. Valdes, Z.W. Qu, G.J. Kroes, J. Rossmeisl, and JK Nørskov. Oxidation and Photo-Oxidation of Water on $TiO_2$ Surface. *The Journal of Physical Chemistry C*, 112(26):9872–9879, 2008.

[85] J.H. Yu, J.S. Lee, and J. Maier. Water incorporation in oxides: A moving boundary problem. *Solid State Ionics*, 2009.

[86] J.A. Enterkin, A.K. Subramanian, B.C. Russell, M.R. Castell, K.R. Poeppelmeier, and L.D. Marks. A homologous series of structures on the surface of $SrTiO_3$ (110). *Nature Materials*, 9(3):245–248, 2010.

[87] S.H. Brewer and S. Franzen. Calculation of the electronic and optical properties of indium tin oxide by density functional theory. *Chemical Physics*, 300(1-3):285–293, 2004.

[88] C.G. Van de Walle. Hydrogen in semiconductors and insulators. *Journal of Alloys and Compounds*, 446:48–51, 2007.

[89] C.G. Van de Walle. Universal alignment of hydrogen levels in semiconductors and insulators. *Physica B: Condensed Matter*, 376:1–6, 2006.

[90] W. Kohn. Nobel Lecture: Electronic structure of matter-wave functions and density functionals. *Reviews of Modern Physics*, 71(5):1253–1266, 1999.

[91] F. Jensen. *Introduction to computational chemistry*. Wiley New York, 1999.

[92] T. Helgaker, P. Jørgensen, and J. Olsen. *Molecular Electronic-Structure Theory*. Cambridge University Press, 2000.

[93] R.G. Parr and W. Yang. *Density-Functional Theory of Atoms and Molecules*. Cambridge University Press, 1994.

[94] R.M. Martin. *Electronic structure: Basic theory and practical methods*. Cambridge University Press, 2002.

[95] E. Schrödinger. An undulatory theory of the mechanics of atoms and molecules. *Physical Review*, 28:1049–1070, 1926.

[96] M. Born and R. Oppenheimer. Zur Quantentheorie der Molekeln. *Annalen der Physik*, 84:457, 1927.

[97] T.N. Truong, M. Nayak, H.H. Huynh, T. Cook, P. Mahajan, L. T. Tran, J. Bharath, S. Jain, H.B. Pham, C. Boonyasiriwat, N. Nguyen, E. Andersen, Y. Kim, S. Choe, J. Choi, T.E. Cheatham, III, and J.C. Facelli. Computational Science and Engineering Online (CSE-Online): A cyber-infrastructure for scientific computing. *Journal of Chemical Information and Modeling*, 46:971–984, 2006.

[98] L.H. Thomas. The calculation of atomic fields. *Proc. Cambridge Phil. Soc.*, 23:542, 1927.

[99] E. Fermi. Eine statistische Methode zur Bestimmung einiger Eigenschaften des Atoms und ihre Anwendung auf die Theorie des periodischen Systems der Elemente. *Z. Phys.*, 48:73, 1928.

[100] P.A.M. Dirac. Exchange phenomena in the Thomas atom. *Proc. Cambridge Phil. Soc.*, 26:376, 1930.

[101] C. F. von Weizsäcker. Zur Theorie der Kernmassen. *Z. Phys.*, 96:431, 1935.

[102] P.M.W. Gill. Density Functional Theory (DFT), Hartree-Fock (HF), and the Self-consistent Field. *J. Chem. Phys*, 100:5066–5075, 1994.

[103] R.G. Parr and W. Yang. Density-functional theory of the electronic structure of molecules. *Annual Review of Physical Chemistry*, 46(1):701–728, 1995.

[104] W. Kohn, A.D. Becke, and R.G. Parr. Density functional theory of electronic structure. *J. phys. Chem.*, 100(31):12974–12980, 1996.

[105] P. Hohenberg and W. Kohn. Inhomogeneous electron gas. *Phys. Rev*, 136(3B):B864–B871, 1964.

[106] J. W. Rayleigh. In Finding the Correction for the Open End of an Organ Pipe. *Phil. Trans.*, 161:77, 1870.

[107] W. Ritz. Über eine neue Methode zur Lösung gewisser Variationsprobleme der mathematischen Physik. *J. reine angew. Math.*, 135:1, 1908.

[108] W. Kohn and L.J. Sham. Self-consistent equations including exchange and correlation effects. *Phys. Rev*, 140(4A):A1133–A1138, 1965.

[109] A. Castro, H. Appel, M. Oliveira, C.A. Rozzi, X. Andrade, F. Lorenzen, M.A.L. Marques, E.K.U. Gross, and A. Rubio. Octopus: A tool for the application of time-dependent density functional theory. *physica status solidi (b)*, 243(11):2465–2488, 2006.

[110] D. Vanderbilt. Soft self-consistent pseudopotentials in a generalized eigenvalue formalism. *Phys. Rev. B*, 41:7892, 1990.

[111] P.E. Blochl. Projector augmented-wave method. *Physical Review-Section B-Condensed Matter*, 50(24):17953–17979, 1994.

[112] J.P. Perdew, K. Burke, and M. Ernzerhof. Generalized gradient approximation made simple. *Physical Review Letters*, 77(18):3865–3868, 1996.

[113] J.P. Perdew and Y. Wang. Accurate and simple analytic representation of the electron-gas correlation energy. *Physical Review B*, 45(23):13244–13249, 1992.

[114] V.I. Anisimov, J. Zaanen, and O.K. Andersen. Band theory and Mott insulators: Hubbard U instead of Stoner I. *Physical Review B*, 44(3):943–954, 1991.

[115] S.L. Dudarev, G.A. Botton, S.Y. Savrasov, C.J. Humphreys, and A.P. Sutton. Electron-energy-loss spectra and the structural stability of nickel oxide: An LSDA+U study. *Physical Review B*, 57(3):1505–1509, 1998.

[116] J. Lee and A.A. Demkov. Charge origin and localization at the n-type $SrTiO_3/LaAlO_3$ interface. *Physical Review B*, 78(19):193104, 2008.

[117] DACAPO pseudopotential code, http://www.fysik.dtu.dk/campos/dacapo.

[118] GPAW projector augmented wave algorithm, URL:https://wiki.fysik.dtu.dk/gpaw/.

[119] G. Kresse and D. Joubert. From ultrasoft pseudopotentials to the projector augmented-wave method. *Phys. Rev. B*, 59:1758, 1999.

[120] G.D. Billing, KV Mikkelsen, and D.G. Truhlar. Introduction to molecular dynamics and chemical kinetics. *Physics Today*, 49:74, 1996.

[121] S. Clark. *Complex structures in tetrahedrally bonded semiconductors*. PhD thesis, University of Edinburgh, 1994.

[122] C. Kittel and H. Kroemer. *Thermal physics*. W.H. Freeman & Co, 1980.

[123] N.W. Ashcroft and N.D. Mermin. *Solid Stale Physics*. Saunders College Publishing International Edition, 1976.

[124] Peter Hänggi, Peter Talkner, and Michal Borkovec. Reaction-rate theory: fifty years after kramers. *Rev. Mod. Phys.*, 62(2):251–341, Apr 1990.

[125] T. Vegge, T. Rasmussen, T. Leffers, O. B. Pedersen, and K. W. Jacobsen. Atomistic simulations of cross-slip of jogged screw dislocations in copper. *Philosophical Magazine Letters*, 81, 2001.

[126] T. Vegge. Locating the rate-limiting step for the interaction of hydrogen with Mg0001 using density-functional theory calculations and rate theory. *Physical Review B*, 70, 2004.

[127] H. Hellmann. Einfuhrung in die Quantenchemie. *Phys. Rev*, 56:340, 1939.

[128] R.P. Feynman. Forces in molecules. *Physical Review*, 56(4):340–343, 1939.

[129] G. Mills, H. Jónsson, and G. Schenter. Reversible work transition state theory: Application to dissociative adsorption of hydrogen. *Surface Sciences*, 324:305 ff., 1995.

[130] H. Jónsson, G. Mills, and K. W. Jacobsen. *Classical and Quantum Dynamics in Condensed Phase Simulations*. World Scientific Singapore, 1998.

[131] G. Henkelman, B.P. Uberuaga, and H. Jónsson. A climbing image nudged elastic band method for finding saddle points and minimum energy paths. *The Journal of Chemical Physics*, 113:9901, 2000.

[132] G. Henkelman and H. Jónsson. A dimer method for finding saddle points on high dimensional potential surfaces using only first derivatives. *The Journal of Chemical Physics*, 111:7010, 1999.

[133] A. Heyden, A.T. Bell, and F.J. Keil. Efficient methods for finding transition states in chemical reactions: Comparison of improved dimer method and partitioned rational function optimization method. *The Journal of chemical physics*, 123:224101, 2005.

[134] K.E. Edgecombe, R.O. Esquivel, V.H. Smith, and F. Müller-Plathe. Pseudoatoms of the electron density. *The Journal of Chemical Physics*, 97:2593, 1992.

[135] G. Henkelman, A. Arnaldsson, and H. Jónsson. A fast and robust algorithm for Bader decomposition of charge density. *Computational Materials Science*, 36(3):354–360, 2006.

[136] R.F.W. Bader. Principle of stationary action and the definition of a proper open system. *Physical Review B*, 49(19):13348–13356, 1994.

[137] R.F.W. Bader. 1997 Polanyi Award Lecture. Why are there atoms in chemistry? *Canadian Journal of Chemistry*, 76(7):973–988, 1998.

[138] K.B. Lipkowitz and D.B. Boyd. *Reviews in Computational Chemistry V*. VCH Publishers, Inc., 1994.

[139] RA Marcus. Electrostatic free energy and other properties of states having nonequilibrium polarization. I. *The Journal of Chemical Physics*, 24:979, 1956.

[140] RA Marcus. On the theory of oxidation reduction reactions involving electron transfer. *The Journal of Physical Chemistry*, 67(4):853–857, 1963.

[141] R.A. Marcus. Electron transfer reactions in chemistry. Theory and experiment. *Reviews of Modern Physics*, 65(3):599–610, 1993.

[142] M. Strange, KS Thygesen, and KW Jacobsen. Electron transport in a Pt-CO-Pt nanocontact: Density functional theory calculations. *Physical Review B*, 73(12):125424, 2006.

[143] M. Strange, IS Kristensen, KS Thygesen, and KW Jacobsen. Benchmark density functional theory calculations for nanoscale conductance. *The Journal of chemical physics*, 128:114714, 2008.

[144] M. Brandbyge, J.L. Mozos, P. Ordejon, J. Taylor, and K. Stokbro. Density-functional method for nonequilibrium electron transport. *Physical Review B*, 65(16):165401, 2002.

[145] Numerous reviews are avaliable from Journal of Alloys and Compounds. URL: http://www.sciencedirect.com/science/journal/09258388.

[146] G. Jones, J.G. Jakobsen, S.S. Shim, J. Kleis, M.P. Andersson, J. Rossmeisl, F. Abild-Pedersen, T. Bligaard, S. Helveg, B. Hinnemann, J.R. Rostrup-Nielsen, I. Chorkendorf, J. Sehested, and J.K. Nørskov. First principles calculations and experimental insight into methane steam reforming over transition metal catalysts. *Journal of Catalysis*, 259(1):147–160, 2008.

[147] F. Studt, F. Abild-Pedersen, T. Bligaard, R.Z. Sorensen, C.H. Christensen, and J.K. Nørskov. Identification of non-precious metal alloy catalysts for selective hydrogenation of acetylene. *Science*, 320(5881):1320, 2008.

[148] R. Coontz and B. Hanson. Not so simple. *Science*, 305(5686):957, 2004.

[149] D. Kennedy. The hydrogen solution. *Science*, 305(5686):917–917, 2004.

[150] S. Orimo, Y. Nakamori, J.R. Eliseo, A. Züttel, and C.M. Jensen. Complex hydrides for hydrogen storage. *Chem. Rev*, 107(10):4111–4132, 2007.

[151] J. Voss, J.S. Hummelshøj, Z. Łodziana, and T. Vegge. Structural stability and decomposition of $Mg(BH4)_2$ isomorphsan ab initio free energy study. *Journal of Physics: Condensed Matter*, 21:012203, 2009.

[152] H.W. Li, S. Orimo, Y. Nakamori, K. Miwa, N. Ohba, S. Towata, and A. Züttel. Materials designing of metal borohydrides: Viewpoints from thermodynamical stabilities. *Journal of Alloys and Compounds*, 446:315–318, 2007.

[153] See http://www.hydrogen.energy.gov/pdfs/review08/st_0_satyapal.pdf for "Hydrogen Storage," presentation by S. Satyapal, 2008 DOE Hydrogen Program, Merit Review and Peer Evaluation Meeting, 9 June 2008.

[154] H. Nöth, E. Wiberg, and L.P. Winter. Boranate und Boranato-metallate. III. Boranatozinkate der Alkalimetalle. *Zeitschrift fr anorganische und allgemeine Chemie*, 386:73–86, 1971.

[155] T. Bligaard, J.K. Nørskov, S. Dahl, J. Matthiesen, C.H. Christensen, and J. Sehested. The Brønsted-Evans-Polanyi relation and the volcano curve in heterogeneous catalysis. *Journal of Catalysis*, 224(1):206–217, 2004.

[156] J. Ranløv, N. Bonanos, F.W. Poulsen, and M. Mogensen. Criteria for prediction of high oxide ion conductivity in perovskite oxides. *Diffusion and Defect Data Part B (Solid State Phenomena)*, 39-40:219–22, 1994.

[157] T. Norby and Y. Larring. Concentration and transport of protons in oxides. *Current Opinion in Solid State and Materials Science*, 2:593–599, 1997.

[158] T. Kudo, K. Yashiro, H. Matsumoto, K. Sato, T. Kawada, and J. Mizusaki. Slow relaxation kinetics of $Sr(Zr,Y)O_3$ in wet atmosphere. *Solid State Ionics*, 179(21-26):851–854, 2008.

[159] H.I. Yoo, J.K. Kim, and C.E. Lee. Electrical Conductivity Relaxations and Chemical Diffusivities of $BaCe_{0.95}Yb_{0.05}O_{2.975}$ upon Hydration and Oxidation. *Journal of the Electrochemical Society*, 156(1):B66–B73, 2009.

[160] C.H. Park. Microscopic Properties of Complex of Hydrogen and Pb-Vacancy in $ABO_3$-Type Perovskite. *Ferroelectrics*, 268(1):17–22, 2002.

[161] H.F. Ades and A.L. Companion. The interaction of hydrogen with point defects in aluminum metal. *Surface Science*, 177(3):553–564, 1986.

[162] E.B. Lombardi, A. Mainwood, and K. Osuch. Ab initio study of the passivation and interaction of substitutional impurities with hydrogen in diamond. *Diamond & Related Materials*, 12(3-7):490–494, 2003.

[163] D.R. Bowler, J.H.G. Owen, K. Miki, and G.A.D. Briggs. Diffusion of paired hydrogen on Si(001). *Phys. Rev. B*, 57(15):8790–8793, 1998.

[164] D.D. Cuong, B. Lee, K.M. Choi, H.S. Ahn, S. Han, and J. Lee. Oxygen Vacancy Clustering and Electron Localization in Oxygen-Deficient SrTiO $_3$: LDA+ U Study. *Physical review letters*, 98(11):115503, 2007.

[165] L.N. Cooper. Bound electron pairs in a degenerate Fermi gas. *Physical Review*, 104(4):1189–1190, 1956.

[166] S. Rey-Mermet and P. Muralt. Solid oxide fuel cell membranes supported by nickel grid anode. *Solid State Ionics*, 179(27-32):1497–1500, 2008.

[167] T. Shimura, M. Komori, and H. Iwahara. Ionic conduction in pyrochlore-type oxides containing rare earth elements at high temperature. *Solid State Ionics*, 86:685–689, 1996.

[168] M.E. Björketun, C.S. Knee, B.J. Nyman, and G. Wahnström. Protonic defects in pure and doped $La_2Zr_2O_7$ pyrochlore oxide. *Solid state ionics*, 178(31-32):1642–1647, 2008.

[169] A. Novak. Hydrogen bonding in solids. Correlation of spectroscopic and structural data. *Structure and Bonding*, 18:177–216, 1974.

[170] A.A. Popov, V.M. Senyavin, O.V. Boltalina, K. Seppelt, J. Spandl, C.S. Feigerle, and R.N. Compton. Infrared, Raman, and DFT vibrational spectroscopic studies of $C_{60}F_{36}$ and $C_{60}F_{48}$. *J. Phys. Chem. A*, 110(28):8645–8652, 2006.

[171] M. Karlsson, M.E. Björketun, P.G. Sundell, A. Matic, G. Wahnström, D. Engberg, L. Börjesson, I. Ahmed, S. Eriksson, and P. Berastegui. Vibrational properties of protons in hydrated $BaIn_xZr_{1-x}O_{3-x/2}$. *Physical Review B*, 72(9):94303, 2005.

[172] K.E.J. Eurenius, E. Ahlberg, I. Ahmed, S.G. Eriksson, and C.S. Knee. Investigation of proton conductivity in $Sm_{1.92}Ca_{0.08}Ti_2O_{7-\delta}$ and $Sm_2Ti_{1.92}Y_{0.08}O_{7-\delta}$ pyrochlores. *Solid State Ionics*, 181(3-4):148–153, 2010.

[173] K. Hayashi, M. Hirano, and H. Hosono. Functionalities of a Nanoporous Crystal $12CaO{\cdot}7Al_2O_3$ Originating from the Incorporation of Active Anions. *Bulletin of the Chemical Society of Japan*, 80(5):872–884, 2007.

[174] A. Yokozawa and Y. Miyamoto. First-principles calculations for charged states of hydrogen atoms in $SiO_2$. *Physical Review B*, 55(20):13783–13788, 1997.

[175] C.G. Van de Walle. Hydrogen in semiconductors and insulators. *Journal of Alloys and Compounds*, 446:48–51, 2007.

[176] M. Widerøe, N. Kochetova, and T. Norby. Transport numbers from hydrogen concentration cells over different oxides under oxidising and reducing conditions. *Dalton Transactions*, 2004(19):3147–3151, 2004.

[177] M. Widerøe, R. Waser, and T. Norby. Transport of hydrogen species in a single crystal $SrTiO_3$. *Solid state ionics*, 177(17-18):1469–1476, 2006.

[178] S. Steinsvik, Y. Larring, and T. Norby. Hydrogen ion conduction in iron-substituted strontium titanate, $SrTi_{1-x}Fe_xO_{3-x/2}$ ($0 \leq x \leq 0.8$). *Solid state ionics*, 143(1):103–116, 2001.

[179] T. Norby and Y. Larring. Mixed hydrogen ion-electronic conductors for hydrogen permeable membranes. *Solid State Ionics*, 136:139–148, 2000.

[180] T. Norby, M. Viderøe, R. Glöckner, and Y. Larring. Hydrogen in oxides. *Dalton Transactions*, pages 3012–3018, 2004.

[181] K. Van Benthem, C. Elsässer, and R.H. French. Bulk electronic structure of SrTiO: Experiment and theory. *Journal of Applied Physics*, 90:6156, 2001.

[182] E. Sanville, S.D. Kenny, R. Smith, and G. Henkelman. Improved grid-based algorithm for Bader charge allocation. *Journal of Computational Chemistry*, 28(5):899, 2007.

[183] F. De Proft, C. Van Alsenoy, A. Peeters, W. Langenaeker, and P. Geerlings. Atomic charges, dipole moments, and Fukui functions using the Hirshfeld partitioning of the electron density. *Journal of computational chemistry*, 23(12):1198–1209, 2002.

[184] J. Enkovaara, C. Rostgaard, J.J. Mortensen, J. Chen, M. Dułak, L. Ferrighi, J. Gavnholt, C. Glinsvad, V. Haikola, HA Hansen, et al. Electronic structure calculations with GPAW: a real-space implementation of the projector augmented-wave method. *Journal of Physics: Condensed Matter*, 22:253202, 2010.

# Article I

# Density functional theory based screening of ternary alkali-transition metal borohydrides: A computational material design project

J. S. Hummelshøj, D. D. Landis, J. Voss, T. Jiang, A. Tekin, N. Bork, M. Dułak, J. J. Mortensen, L. Adamska, J. Andersin, J. D. Baran, G. D. Barmparis, F. Bell, A. L. Bezanilla, J. Bjork, M. E. Björketun, F. Bleken, F. Buchter, M. Bürkle, P. D. Burton, B. B. Buus, A. Calborean, F. Calle-Vallejo, S. Casolo, B. D. Chandler, D. H. Chi, I Czekaj, S. Datta, A. Datye, A. DeLaRiva, V Despoja, S. Dobrin, M. Engelund, L. Ferrighi, P. Frondelius, Q. Fu, A. Fuentes, J. Fürst, A. García-Fuente, J. Gavnholt, R. Goeke, S. Gudmundsdottir, K. D. Hammond, H. A. Hansen, D. Hibbitts, E. Hobi, Jr., J. G. Howalt, S. L. Hruby, A. Huth, L. Isaeva, J. Jelic, I. J. T. Jensen, K. A. Kacprzak, A. Kelkkanen, D. Kelsey, D. S. Kesanakurthi, J. Kleis, P. J. Klüpfel, I Konstantinov, R. Korytar, P. Koskinen, C. Krishna, E. Kunkes, A. H. Larsen, J. M. G. Lastra, H. Lin, O. Lopez-Acevedo, M. Mantega, J. I. Martínez, I. N. Mesa, D. J. Mowbray, J. S. G. Mýrdal, Y. Natanzon, A. Nistor, T. Olsen, H. Park, L. S. Pedroza, V Petzold, C. Plaisance, J. A. Rasmussen, H. Ren, M. Rizzi, A. S. Ronco, C. Rostgaard, S. Saadi, L. A. Salguero, E. J. G. Santos, A. L. Schoenhalz, J. Shen, M. Smedemand, O. J. Stausholm-Møller, M. Stibius, M. Strange, H. B. Su, B. Temel, A. Toftelund, V Tripkovic, M. Vanin, V Viswanathan, A. Vojvodic, S. Wang, J. Wellendorff, K. S. Thygesen, J. Rossmeisl, T. Bligaard, K. W. Jacobsen, J. K. Nørskov, and T. Vegge[a)]

*The 2008 CAMD Summer School in Electronic Structure Theory and Materials Design, Center for Atomic-scale Materials Design, Department of Physics, Technical University of Denmark, DK-2800 Kgs. Lyngby, Denmark*[b)]

(Received 20 November 2008; accepted 8 May 2009; published online 1 July 2009)

We present a computational screening study of ternary metal borohydrides for reversible hydrogen storage based on density functional theory. We investigate the stability and decomposition of alloys containing 1 alkali metal atom, Li, Na, or K ($M_1$); and 1 alkali, alkaline earth or $3d/4d$ transition metal atom ($M_2$) plus two to five $(BH_4)^-$ groups, i.e., $M_1M_2(BH_4)_{2-5}$, using a number of model structures with trigonal, tetrahedral, octahedral, and free coordination of the metal borohydride complexes. Of the over 700 investigated structures, about 20 were predicted to form potentially stable alloys with promising decomposition energies. The $M_1(Al/Mn/Fe)(BH_4)_4$, $(Li/Na)Zn(BH_4)_3$, and $(Na/K)(Ni/Co)(BH_4)_3$ alloys are found to be the most promising, followed by selected $M_1(Nb/Rh)(BH_4)_4$ alloys. © *2009 American Institute of Physics*.
[DOI: 10.1063/1.3148892]

## I. INTRODUCTION

The development of sustainable energy solutions for the future requires new and improved materials. Specifically designed material properties are needed to solve the grand challenges in energy production, storage, and conversion. Within energy storage, hydrogen has been investigated extensively over the past decade[1] as one of the few promising energy carriers which can provide a high energy density without resulting in $CO_2$ emission by the end user. Finding materials for efficient, reversible hydrogen storage, however, remains challenging. Here, the specific requirements of the rapidly growing transportation sector coupled with complex engineering challenges[2] have directed research toward complex materials with extreme hydrogen storage capacities[3] such as metal borohydrides[4] and metal ammines.[5] Finding materials with high reversible hydrogen content and optimal thermodynamic stability is essential if hydrogen is going to be used as a commercial fuel in the transport sector. The binary metal borohydrides have been studied extensively: the alkali based compounds, e.g., $LiBH_4$,[6–8] are too thermodynamically stable, the alkaline earth compounds are kinetically too slow and practically irreversible,[9] and the transition metal borohydrides are either unstable or irreversible.[10] This leaves hope that mixed metal ("alloyed") systems might provide new opportunities.

The use of computational screening techniques has proved a valuable tool in narrowing the phase space of potential candidate materials for hydrogen storage.[11,12] Recent density functional theory (DFT) calculations have shown that the thermodynamic properties of even highly complex borohydride superstructures can be estimated by DFT using simple model structures, if the primary coordination polyhedra are correctly accounted for.[13] These findings enable faster screening studies of thermodynamic stability and decomposition temperatures for, e.g., ternary and quaternary borohydride systems; not only in terms of reduced computational effort due to smaller system sizes but also with the advantage that the exact space group does not need to be known

a)Electronic mail: teve@risoe.dtu.dk.
b)For a full list of affiliations, see Ref. 41.

 

*a priori*.

In the present paper, we apply a "local coordination screening" (LCS) approach to search for novel metal borohydrides. The vast majority of the calculations were performed as part of the 2008 CAMD summer school in electronic structure theory and materials design, where more than 100 scientists combined DFT calculations, database methods, and screening techniques to investigate the structure and stability of promising ternary borohydrides. A few additional calculations were subsequently performed based on the insight gained from the initial screening.

Out of 757 investigated $M_1M_2(BH_4)_{2-5}$ ($M_1$=alkali metal and $M_2$=alkali, alkaline earth or $3d/4d$ transition metal) compositions and structures, a total of 22 were found to form potentially stable alloys with promising decomposition energies, which should subsequently be subjected to more detailed theoretical and experimental verification.

## II. COMPUTATIONAL SETUP

Groups of alloy compositions and structures were divided among different groups of scientists, each of which was responsible for its own subset of the alloy configuration space. A number of predefined structural templates and optimization procedures had been prepared to assist the groups in setting up structures and calculations for the initial optimization (see Sec. II B). This was done to ensure a sufficient accuracy in all calculations (i.e., convergence with respect to plane wave cutoff, *k*-point sampling, etc.).

To ensure reliability of the generated results, an automated checking procedure was enforced before a result could be included in the database (see Sec. III) to ensure the presence of the required output (total energies, lattice constants, etc.).

### A. Computational parameters

The total energies and gradients were calculated within density functional theory[14] as implemented by the software package Dacapo.[15] A plane wave basis set with a cutoff energy of 350 eV (density grid cutoff of 700 eV) and the RPBE exchange-correlation functional[15] were used for all calculations. Dacapo uses ultrasoft pseudopotentials[16] for a description of the ionic cores. The coordinate optimization was implemented and performed within the atomic simulation environment.[17] The electronic Brillouin zones were sampled with $(4\times4\times4)$ *k*-points (spacings of $\sim0.05$ Å$^{-1}$). A quasi-Newton method[18] was used for all relaxations.

### B. Configuration space and template structures

The alloys which were initially screened have the general formula $M_1M_2(BH_4)_x$, where $M_1\in\{Li,Na,K\}$ and $x=2-4$. The $x=2$ alloys were investigated for $M_2\in\{Li,Na,K\}$, and $x=3,4$ for $M_2\in\{Li,Na,K,Mg,Al,Ca,Sc-Zn,Y-Mo,Ru-Cd\}$.

In order to limit the total number of calculations, only template structures with tetrahedral and octahedral coordination of the $(BH_4)^-$ groups to the metal atoms were used. Most metals prefer an octahedral coordination of their ligands, but for the metal borohydrides the ligand-ligand repulsion between the relatively large $(BH_4)^-$ ions often forces a lower coordination number. The primary structures observed and reported in literature for the alkali and alkaline earth borohydrides are either tetrahedral (for the smallest Li and Mg) or octahedral (for the larger Na, K, and Ca), while a trigonal planar ligand arrangement is observed for $Al(BH_4)_3$. However, Al can also have a tetrahedral coordination as is the case of the $LiAl(BH_4)_4$ alloy obtained here (see Sec. V), and since the radii of the considered ions lie between the radius for K and the radius for Al, the tetrahedral and octahedral primary structures are expected to be representative.

For each alloy composition, four different template structures were used to sample the tetrahedral and octahedral primary structures in the combinations: tetrahedral/tetrahedral, octahedral/octahedral, tetrahedral/octahedral, and octahedral/tetrahedral, referring to the coordination of the $(BH_4)^-$ groups to the $M_1$ and $M_2$ atoms, respectively. The coordination polyhedra were either corner sharing, edge sharing, or a combination to yield the required stoichiometric ratio of $(BH_4)^-$ groups (see Fig. 1). All structures were designed to have a unit cell containing only one formula unit (see Sec. II D). It has previously been shown that these simple template structures can be within $\sim0.1$ eV (10 kJ/mol $H_2$) of the true ground state energy if the local coordination is correctly accounted for; e.g., $M_1M_2(BH_4)_2$-tetra for $LiBH_4$,[7] $M_1M_2(BH_4)_4$-octa for $Ca(BH_4)_2$,[19] and even $M_1M_2(BH_4)_4$-tetra for the free energy of $Mg(BH_4)_2$ superstructures.[13]

The initial optimization of the structures only relaxed the hydrogen positions and the unit cell volume while keeping the metal-boron coordination polyhedra fixed. For a given set of $(M_1,M_2)$, the most stable structure was then used as the starting point for a calculation in which all atomic positions and the unit cell were relaxed. Even though many of the structures did not change significantly during the final relaxation, it added, in principle, an additional structure to the phase space for each set of $(M_1,M_2)$. These are included as "other" structures in the results (Figs. 3–12) to distinguish them from the structures with fixed metal-boron coordination polyhedra, even though the original coordination polyhedra are only slightly distorted in many of them.

A number of structures were subsequently added based on the knowledge gained from the initial screening and the reference binary borohydride structures (see Secs. IV and VI). In some of these structures, the metal ions had the same valence as in the reference structures, which meant that the four $x=2$ templates were also applied to $M_2\in\{Ni,Pd,Cu,Ag\}$, while a new template for $x=5$ was investigated for $M_2\in\{Ti,Zr\}$ in the two combinations tetrahedral/octahedral and octahedral/tetrahedral. An alternative $x=3$ tetragonal/trigonal template was applied to $M_2\in\{Mg,Al,Ca,Sc-Zn,Y-Mo,Ru-Cd\}$ to investigate possible size effects. In this structure, the $M_1$ ion has a tetrahedral coordination while the $M_2$ atom is surrounded by three $(BH_4)^-$ groups in a trigonal planar arrangement (see Fig. 2). This enabled the metal-boron distances for the two metals to be optimized independently, which was not pos-

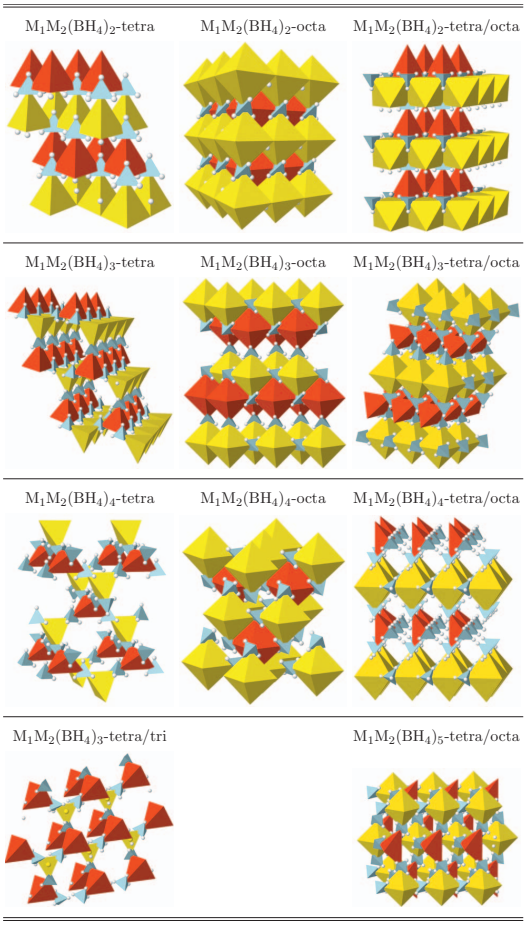


FIG. 1. The template structures of $M_1M_2(BH_4)_{2-5}$. Red and yellow polyhedra show the coordination of the B atoms around the $M_1$ and $M_2$ atoms, respectively; blue tetrahedra represent the $(BH_4)^-$ groups. The octa/tetra structures are obtained by switching $M_1$ and $M_2$ in the tetra/octa structures.

sible in the original $x=3$ templates, but found to be required to obtain the preferred local coordination of certain alloys.

In total, 757 structures have been simulated and are reported herein.

### C. Group calculations

The 69 sets of $(M_1,M_2)$ combinations investigated in this study were divided among 32 groups of scientists for the initial screening. Each group followed step I of the calculational procedure outlined below for each alloy containing $M_1$ and $M_2$ and step II for the most stable resulting structure.

### D. Calculational procedure

#### 1. Step I

An initial structure was set up by calling a function that populates one of the four template structures with two supplied metal ions, e.g., Li and Sc. The function utilizes the ionic radii obtained from the calculations of binary reference borohydrides, i.e., individual metal atom borohydrides, to calculate metal-boron distances, where the ionic radius used for a $(BH_4)^-$ group depends on whether a face, edge or corner of the H-tetrahedron points toward the metal atom. In general, this ensured that the effective lattice constant and the $c/a$ ratio were close to the optimum. The initial structure was used as the initial guess for the first iteration of the following procedure.

TABLE I. The calculated reference energies for the binary borohydrides in their most stable template structures (see Fig. 2).

| | wt % (kg $H_2$/kg material) | $\Delta E_{decomp}$ (eV/$H_2$) |
|---|---|---|
| $K(BH_4)$ | 7.5 | −0.968 |
| $Na(BH_4)$ | 10.7 | −0.729 |
| $Li(BH_4)$ | 18.5 | −0.422 |
| $Ag(BH_4)$ | 3.3 | 0.278 |
| $Cu(BH_4)$ | 5.1 | 0.352 |
| $Pd(BH_4)$ | 3.3 | 0.661 |
| $Ni(BH_4)$ | 5.5 | 0.680 |
| $Ca(BH_4)_2$ | 11.6 | −0.636 |
| $Mg(BH_4)_2$ | 14.9 | −0.467 |
| $Zn(BH_4)_2$ | 8.5 | −0.063 |
| $Cd(BH_4)_2$ | 5.7 | −0.043 |
| $V(BH_4)_2$ | 10.0 | −0.031 |
| $Nb(BH_4)_2$ | 6.6 | 0.066 |
| $Fe(BH_4)_2$ | 9.4 | 0.090 |
| $Cr(BH_4)_2$ | 9.9 | 0.162 |
| $Mn(BH_4)_2$ | 9.5 | 0.174 |
| $Co(BH_4)_2$ | 9.1 | 0.264 |
| $Mo(BH_4)_2$ | 6.4 | 0.280 |
| $Rh(BH_4)_2$ | 6.1 | 0.340 |
| $Ru(BH_4)_2$ | 6.2 | 0.351 |
| $Y(BH_4)_3$ | 9.1 | −0.676 |
| $Sc(BH_4)_3$ | 13.5 | −0.595 |
| $Al(BH_4)_3$ | 16.9 | −0.209 |
| $Zr(BH_4)_4$ | 10.7 | −0.429 |
| $Ti(BH_4)_4$ | 15.0 | −0.252 |

All hydrogen positions were relaxed until the maximum force on the atoms reached 0.05 eV/Å or, alternatively, a maximum of 50 quasi-Newton steps had been performed. The resulting structure was then contracted and expanded to 90%, 95%, 105%, and 110% of the unit cell volume by a proportional scaling of the unit cell, while keeping the B–H distances in each $(BH_4)^-$ group fixed; a single total energy calculation was performed for each volume. A Murnaghan equation-of-state was fitted to the calculated five points to estimate the optimal unit cell volume, to which the unit cell was then scaled (again while conserving B–H distances), followed by a relaxation of the hydrogen positions to a force convergence of 0.05 eV/Å.

After each iteration, an energy versus unit cell volume plot was inspected visually to decide whether the minimum had been sufficiently sampled or an additional iteration of the procedure should be performed; in the latter case, a structure resulting from the first iteration was used as the starting guess for the next iteration.

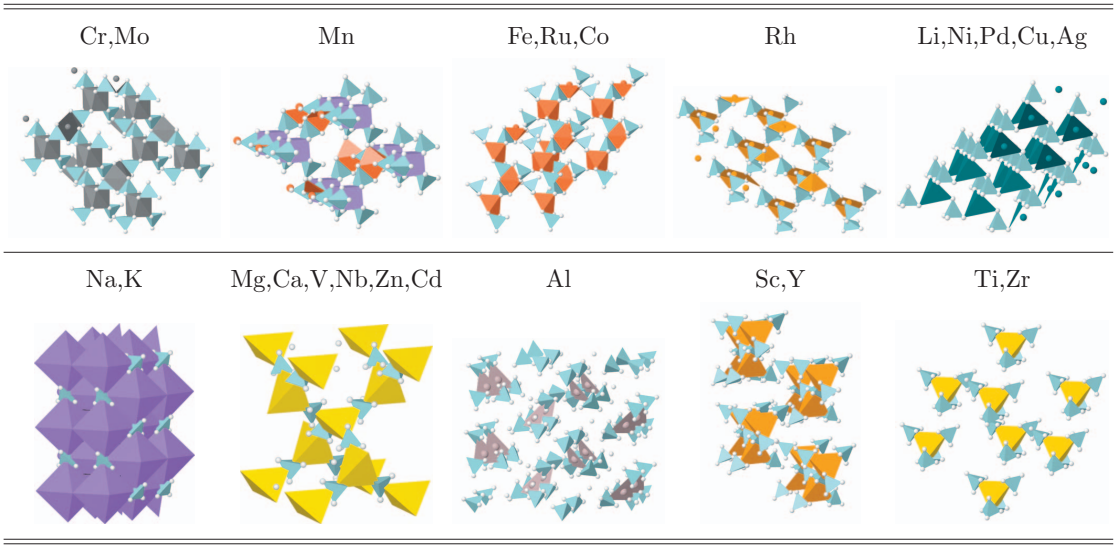


FIG. 2. The structures used for calculating the binary reference energies. For Cr, Mo, Mn, Fe, Ru, Co, Rh, Li, Ni, Pd, Cu, and Ag, the polyhedra show the coordination of the H atoms; the coordination of the $(BH_4)^-$ groups are tetrahedral in these structures. For the remaining metals the coordination polyhedra show the coordination of the $(BH_4)^-$ groups.

#### *2. Step II*

When all template structures for each of the $(M_1,M_2)$ alloys had been optimized in step I, the most stable structure was relaxed without constraints by repeating the procedure that first relaxes all atomic positions for a fixed cell and then the unit cell for fixed internal positions. To limit the computational time used by this algorithm, the number of iterations was limited to 5, and the number of steps per iteration was limited to 12 for the internal relaxation and 5 for the unit cell relaxation.

#### *3. Procedure for the additional structures*

For the structures calculated later, the $x=2$ structures (monovalent transition metals) followed the same procedure mentioned above, whereas only a single free optimization was performed on the extra $x=3$ and $x=5$ structures, in which all atoms were allowed to relax.

## III. DATA COLLECTION AND STORAGE

Every group executed the calculation procedures for steps I and II. After each step, the validity of the results was checked by the group and the results were checked in (stored in a global location for indexing) to the common database.

### A. Front end

A Python[20] script took care of checking in all relevant files that were needed for subsequent checking. This included the calculation script and the output files containing the atoms, energies and the calculational parameters. A subversion (svn) version control system[21] assisted to manage groups and users, storing results and assuring transaction consistency.

### B. Back end

A second Python script was used to extract the relevant parameters, i.e., the total energy, unit cell volume, chemical symbols, structure, and the calculational parameters such as *k*-points, number of bands, density wave cutoff, and to select the best structure (at any given time) for every borohydride to create/update the intermediate result plots, which were accessible to all participants. Python, in combination with Matplotlib,[22] was used to ensure a flexible user interface and to generate the plots. A special Python class managed the resulting data, consisting of approximately 5500 calculations. This class provided basic database operations such as selecting, sorting, and filtering of data and facilitated the creation of the plots considerably.

The overall construction of the database and data retrieval procedures will also facilitate screening for possible correlations between combinations of a number of different values in future projects.

## IV. DATA ANALYSIS

The initial screening procedure presented here is performed to reduce the number of potential alloys for further investigation, and two simple selection criteria were set up to assess the stability of the investigated alloy structures against phase separation/disproportionation and decomposition. The stabilities were first analyzed against phase separation into the original binary borohydrides as illustrated for $LiSc(BH_4)_4$:

$$\Delta E_{\text{alloy}} = E_{\text{LiSc(BH}_4)_4} - (E_{\text{LiBH}_4} + E_{\text{Sc(BH}_4)_3}). \quad (1)$$

Reference energies for the 3 alkali, 2 alkaline earth, $Al(BH_4)_3$ plus 19 transition metal borohydrides were ob-

TABLE II. Structures with alloying energies $\Delta E_{alloy} < 0.0$ eV/f.u. (formula unit) and decomposition energies $\Delta E_{decomp} < 0.0$ eV/$H_2$.

| | wt % (kg $H_2$/kg material) | $\Delta E_{alloy}$ (eV/f.u.) | $\Delta E_{decomp}$ (eV/$H_2$) |
|---|---|---|---|
| $LiNa(BH_4)_2$ | 13.5 | −0.020 | −0.581 |
| $KZn(BH_4)_3$ | 8.1 | −0.349 | −0.423 |
| $KAl(BH_4)_4$ | 12.9 | −0.138 | −0.416 |
| $NaAl(BH_4)_4$ | 14.7 | −0.279 | −0.373 |
| $KCd(BH_4)_3$ | 6.2 | −0.005 | −0.352 |
| $NaZn(BH_4)_3$ | 9.1 | −0.358 | −0.344 |
| $LiAl(BH_4)_4$ | 17.3 | −0.391 | −0.311 |
| $KFe(BH_4)_3$ | 8.7 | −0.116 | −0.282 |
| $LiZn(BH_4)_3$ | 10.4 | −0.362 | −0.243 |
| $NaFe(BH_4)_3$ | 9.8 | −0.141 | −0.206 |
| $KMn(BH_4)_4$ | 10.5 | −0.148 | −0.174 |
| $NaNb(BH_4)_4$ | 9.2 | −0.128 | −0.165 |
| $KCo(BH_4)_3$ | 8.5 | −0.089 | −0.161 |
| $NaMn(BH_4)_4$ | 11.7 | −0.284 | −0.131 |
| $KNi(BH_4)_3$ | 8.5 | −0.120 | −0.116 |
| $LiFe(BH_4)_3$ | 11.3 | −0.141 | −0.104 |
| $LiNb(BH_4)_4$ | 10.1 | −0.194 | −0.097 |
| $NaCo(BH_4)_3$ | 9.6 | −0.143 | −0.090 |
| $KRh(BH_4)_4$ | 8.0 | −0.058 | −0.079 |
| $LiMn(BH_4)_4$ | 13.3 | −0.358 | −0.063 |
| $NaNi(BH_4)_3$ | 9.6 | −0.164 | −0.043 |
| $NaRh(BH_4)_4$ | 8.7 | −0.033 | −0.016 |

TABLE III. Structures with alloying energies $0 < \Delta E_{alloy} < 0.2$ eV/f.u. (formula unit) with decomposition energies $\Delta E_{decomp} < 0.0$ eV/$H_2$.

| | wt % (kg $H_2$/kg material) | $\Delta E_{alloy}$ (eV/f.u.) | $\Delta E_{decomp}$ (eV/$H_2$) |
|---|---|---|---|
| $KNa(BH_4)_2$ | 8.8 | 0.095 | −0.825 |
| $NaY(BH_4)_4$ | 9.4 | 0.115 | −0.675 |
| $NaCa(BH_4)_3$ | 11.2 | 0.129 | −0.645 |
| $LiY(BH_4)_4$ | 10.4 | 0.033 | −0.609 |
| $LiCa(BH_4)_3$ | 13.2 | 0.052 | −0.556 |
| $LiSc(BH_4)_4$ | 14.5 | 0.143 | −0.534 |
| $NaCd(BH_4)_3$ | 6.7 | 0.003 | −0.271 |
| $KNb(BH_4)_4$ | 8.4 | 0.016 | −0.207 |
| $NaV(BH_4)_4$ | 12.1 | 0.076 | −0.188 |
| $NaAg(BH_4)_2$ | 5.0 | 0.193 | −0.177 |
| $LiCd(BH_4)_3$ | 7.4 | 0.102 | −0.152 |
| $KCr(BH_4)_4$ | 10.7 | 0.199 | −0.136 |
| $LiV(BH_4)_4$ | 13.8 | 0.061 | −0.113 |
| $NaCr(BH_4)_4$ | 12.0 | 0.050 | −0.095 |
| $KPd(BH_4)_3$ | 6.4 | 0.047 | −0.095 |
| $KMo(BH_4)_4$ | 8.3 | 0.185 | −0.079 |
| $KRu(BH_4)_3$ | 6.5 | 0.168 | −0.061 |
| $NaMo(BH_4)_4$ | 9.0 | 0.056 | −0.035 |
| $LiCr(BH_4)_4$ | 13.6 | 0.029 | −0.021 |
| $NaPd(BH_4)_3$ | 7.0 | 0.052 | −0.014 |

tained using the most stable structures among the applied $M_2(BH_4)_{1-4}$ model templates (see Table I). Due to computational constraints, the performed calculations are not spin polarized, which causes certain reference structures, e.g., $Mn(BH_4)_2$, to become unstable. In order not to exclude potentially stable candidates, the assessment in Eq. (1) was used for all reference structures (see Table I).

For assessing the stability of alloys with a potentially less favorable stoichiometry, like $LiSc(BH_4)_3$, an effective reference value for $E_{Sc(BH_4)_2}$ was determined from the stable $E_{Sc(BH_4)_3}$ as $E_{Sc(BH_4)_2}^{*} = E_{Sc(BH_4)_3} - 2E_{H_2} - E_B$. Using $1/2(B_2H_6 + H_2)$ as a reference only shifts the energy by 0.07 eV/$H_2$ and does not result in a new preferred coordination for any of the stable alloys.

The decomposition pathways of binary and ternary metal borohydrides are often highly complex and differ significantly from one system to the next, e.g., $LiBH_4$,[23] $Mg(BH_4)_2$,[24] and $LiZn(BH_4)_3$,[25] and the formed products can even depend on the details of the desorption conditions. Certain compounds form transition metal hydrides,[26] others form transition metal borides,[27] di-,[10] or dodeca-boranes,[28] and others again, e.g., Cr, Cd, Mn, and $Zn(BH_4)_2$ decompose to the elements.[29,30] Given the inclusive nature of this initial screening study and the fact that the true decomposition pathways in most of the investigated alloys are not well known, a simple and generic decomposition pathway was selected, which all interesting mixed borohydrides must be stable against (as a minimum). Here, the alloys decompose into the highly stable alkali- and alkaline earth hydrides, transition metals, boron and $H_2$, e.g.:

$$\Delta E_{decomp} = E_{LiMn(BH_4)_3} - (E_{LiH} + E_{Mn} + 3E_B + 5.5E_{H_2}). \quad (2)$$

In this definition, $\Delta E_{decomp}$ estimates the stability of the alloy against decomposition. Transition metal hydrides, metal borides, higher order boranates and diborane, which may potentially form, are thus not taken into consideration in this first screening.

The analysis is based on the ground state energies only. Although the difference in vibrational entropy between hydrogen in an alkali metal borohydride and in the gas phase is often significantly smaller than in conventional metal hydrides,[31] the contributions to the free energy from the vibrational entropy may be significant.

A stability range of $\Delta E_{alloy} \leq 0.0$ eV/f.u. (formula unit) and $\Delta E_{decomp} \in \{-0.5; 0.0\}$ eV/$H_2$ is used to select the most interesting alloys with $\Delta E_{decomp} = -0.2$ eV/$H_2$ as the target value (see Table II), but given the idealized screening criteria in Eqs. (1) and (2), alloys with only small instabilities, i.e., $\Delta E_{alloy} \leq 0.2$ eV/f.u and $\Delta E_{decomp} \leq 0.0$ eV/$H_2$ should not be discarded *a priori* (see Table III).

## V. RESULTS

As the first step of the stability screening, we have plotted the alloying energy against the decomposition energy of the 757 investigated alloys (see Fig. 3). Most of the alloys are found to be stable against decomposition, but the majority are found to be unstable against separation into their binary components ($\Delta E_{alloy} > 0.0$ eV/f.u.). Many are still within the 0.2 eV/f.u. boundary regime. The lithium-containing alloys (red) are less stable against decomposition than those containing sodium (blue) and potassium (green). Restricting the plot to only the most stable structure for each

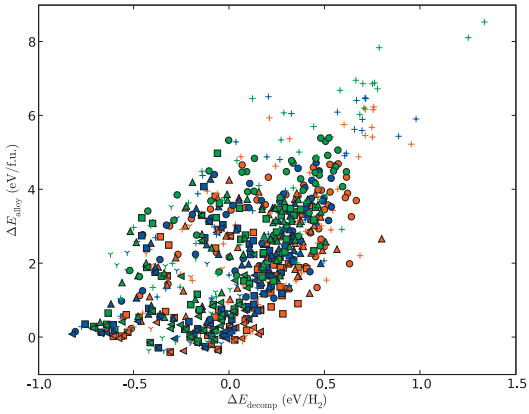


FIG. 3. The alloying energy, $\Delta E_{alloy}$, as a function of the decomposition energy, $\Delta E_{decomp}$, for all alloy compositions. Colors: Li (red), Na (blue), and K (green). Investigated coordinations: tetra (□), octa (○), octa-tetra (△), tetra-octa (+), tetra-tri ( ᛉ ), other (◁). Total number of structures: 757.

$M_1M_2$ system (see Fig. 4) seems to support this observation, and yields a total of 22 stable alloys (see Table II). Figure 4 is dominated by alloys where (a) both metal atoms are tetrahedrally coordinated to the borohydride groups (□), (b) one is tetrahedral the other trigonal ( ᛉ ), and (c) so-called other (◁), where all constraints have been lifted. Some octa-tetra (△) and tetra-octa (+) are also observed.

Plotting the hydrogen density of the stable alloys, $\Delta E_{alloy} \leq 0.0$ eV/f.u. and $\Delta E_{decomp} \leq 0.0$ eV/H$_2$, Fig. 5 shows that alloys containing potassium (in green) are found to have the lowest density, followed by sodium (in blue) and lithium (in red), as expected. The overall density is found to be around that of liquid hydrogen, which is largely due to the choice of simple template structures; higher densities are expected for real systems as previously observed for $Mg(BH_4)_2$.[9] Alloys containing Al, Mn, Fe, and Zn are found to be stable for all alkali metals screened, whereas those

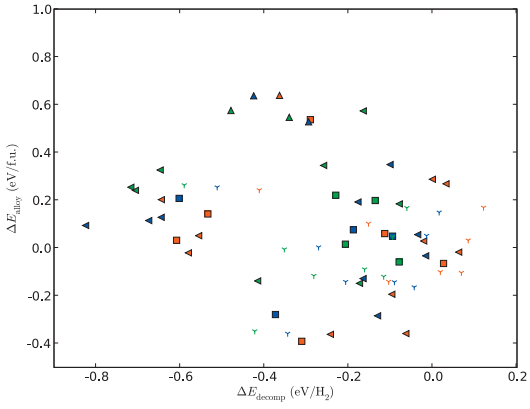


FIG. 4. The alloying energy, $\Delta E_{alloy}$, as a function of the decomposition energy, $\Delta E_{decomp}$, for all preferred alloy systems. Colors: Li (red), Na (blue) and K (green). Preferred local coordination: tetra (□), octa (○), octa-tetra (△), tetra-octa (+), tetra-tri ( ᛉ ), other (◁).

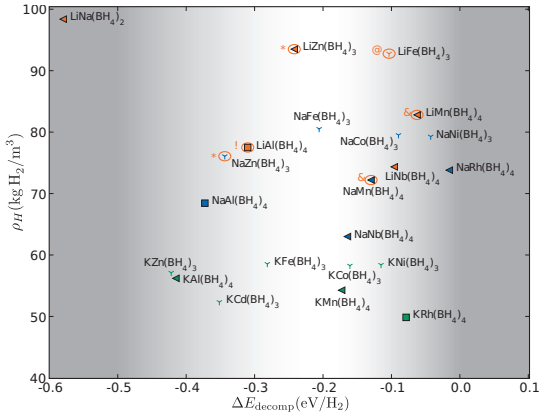


FIG. 5. The hydrogen density (kg $H_2$ $m^{-3}$ as a function of the decomposition energy for the 22 alloys with $\Delta E_{alloy} \leq 0.0$ eV/f.u. and $\Delta E_{decomp} \leq 0.0$ eV/$H_2$. References to experimental observations: !: Ref. 25, @: Ref. 37, &: Ref. 38, *: Ref. 39. Colors: Li (red), Na (blue), and K (green). Preferred local coordination: tetra (□), octa (○), octa-tetra (△), tetra-octa (+), tetra-tri ( ᛉ ), other (◁).

based on Co, Ni, Nb, and Rh are stable for two out of three alkali metals. The only other stable alloys are $KCd(BH_4)_3$ and $LiNa(BH_4)_2$ (see Table II).

The storage capacity (wt % hydrogen) of the stable alloys is plotted as a function of the decomposition energy, $\Delta E_{decomp}$, in Fig. 6. Here, the data from the binary reference structures have also been included, and it is clearly seen that the stability has been reduced significantly compared to the highly stable binary borohydrides. Most alloys have storage capacities above the DOE 2015 system target of 9 wt % (Ref. 3) and several also have favorable stabilities. A number of these ternary borohydrides have been synthesized either

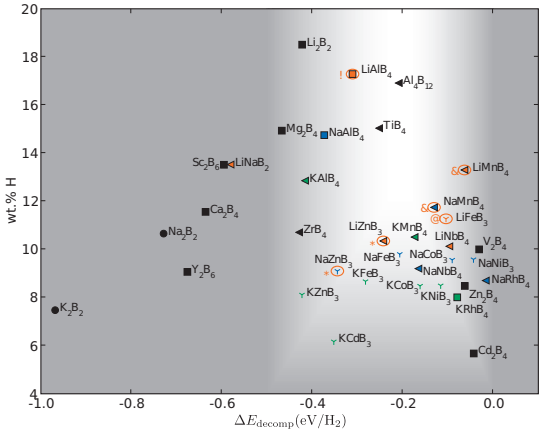


FIG. 6. The weight percent of hydrogen (wt. %) as a function of the decomposition energy, $\Delta E_{decomp}$ [Eq. (2)], for all 22 stable alloys and 13 binary reference structures ($\Delta E_{decomp} \leq 0.0$ eV/$H_2$ and $\Delta E_{alloy} \leq 0.0$ eV/f.u.). References to experimental observations: !: Ref. 25, @: Ref. 37, &: Ref. 38, *: Ref. 39. Colors: Li (red), Na (blue), K (green), and reference structures (black). Labels: "$MB_x$" refers to "$M(BH_4)_x$." Preferred local coordination: tetra (□), octa (○), octa-tetra (△), tetra-octa (+), tetra-tri ( ᛉ ), other (◁).

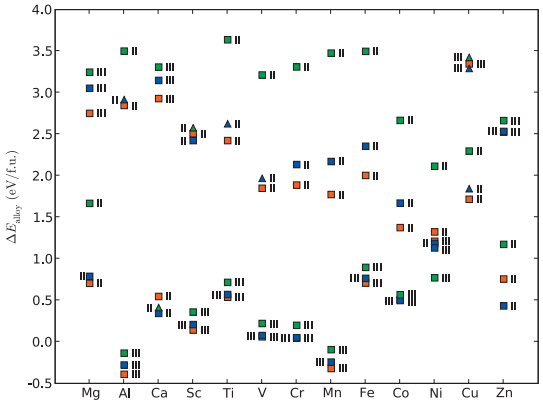


FIG. 7. The alloying energy, $\Delta E_{alloy}$, for the 3*d*-metals (plus Mg, Al, and Ca) in their preferred $M_1M_2(BH_4)_x$ template structures with $M_1$, $M_2$, and B fixed for both $x=3$ and $x=4$. Colors: Li (red), Na (blue), and K (green). Preferred local coordination: tetra (□), octa (○), octa-tetra (△), tetra-octa (+). The labels indicate the oxidation state of $M_2$.

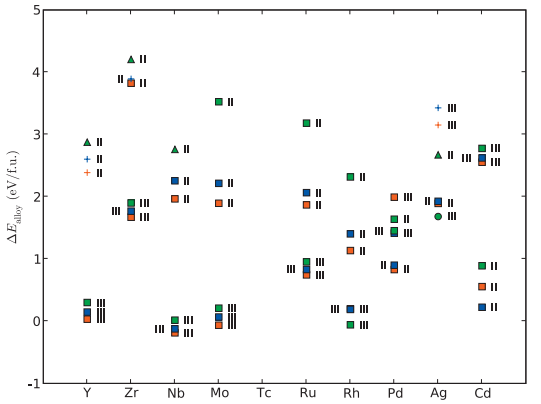


FIG. 8. The alloying energy, $\Delta E_{alloy}$, for the 4*d*-metals in their preferred $M_1M_2(BH_4)_x$ template structures with $M_1$, $M_2$, and B fixed for both $x=3$ and 4. Colors: Li (red), Na (blue), and K (green). Preferred local coordination: tetra (□), octa (○), octa-tetra (△), tetra-octa (+). The labels indicate the oxidation state of $M_2$.

very recently or historically (circled in Figs. 5 and 6). Of the experimentally observed stable/metastable structures, $LiSc(BH_4)_4$,[10] $KNa(BH_4)_2$,[32] and $Li_2Cd(BH_4)_4$ (Ref. 30) show a weak preference for phase separation, but are all found to be potentially stable (see Table III); only $LiK(BH_4)_2$ (Ref. 33) ($\Delta E_{alloy}=0.202$ eV/f.u. and $\Delta E_{decomp}=-0.645$ eV/$H_2$) and $LiNi(BH_4)_3$ (Ref. 30) ($\Delta E_{alloy}=-0.104$ eV/f.u. and $\Delta E_{decomp}=0.069$ eV/$H_2$) fall marginally outside the selection criteria. Furthermore, $LiMn(BH_4)_3$ and $NaMn(BH_4)_3$ are found experimentally to decompose at ~100 and 110 °C,[34] and $LiZn(BH_4)_3$ and $LiAl(BH_4)_4$ are found to disproportionate at ~130 °C.[25] These are all structures that are located near the optimal stability in the figure (the nonshaded region).

## VI. TRENDS

Given the systematic approach to the screening study it is also possible to extract information from the database about possible trends and correlations, in order to search for predictors and descriptors[35] for the design of future quaternary alloys or alloys with different cation stoichiometries.

### A. 3*d* and 4*d* transition metals

The stability of the alloys, as produced by the most stable $x=3$ and $x=4$ initial template structures before the free relaxation, is presented for all 3*d* transition metals (plus Mg, Ca, and Al) in Fig. 7, and for the 4*d* transition metals in Fig. 8. A clear preference for the $M_1M_2(BH_4)_4$-tetra template is observed, which is somewhat surprising, because many of the transition metals have an oxidation state of II in the reference calculations (see Table I). This apparent discrepancy could result from partially non-ionic bonding in these structures, meaning that the coordination of the hydrogen atoms to the metal is the determining factor, not whether the metal has the "correct" valence. For instance, we find no significant energy difference between $Fe_2(BH_4)_3$ and $Fe(BH_4)_2$ as long as the H atoms are octahedrally coordinated to the Fe atom. Size effects also become apparent here since the $M_1M_2(BH_4)_4$-tetra template is the only template structure that allows the coordination polyhedra of $M_1$ and $M_2$ to be relaxed independently. This is supported by the larger spacing between most of the Li, Na, and K alloy energies produced by the other template structures (see Figs. 7 and 8).

To investigate this further, the $M_1M_2(BH_4)_3$-tetra/tri-template was applied to all alloys, and in Figs. 9 and 10, the final alloy stabilities are presented; these also include the free relaxation and the additional $x=2$ and $x=5$ calculations. It is seen that the $M_1M_2(BH_4)_3$-tetra/tri-structures now become the most stable for a number of alloys and that the Li, Na, and K points lie closer indicating a reduction in the size effects.

There is a general agreement between valencies in the reference calculations and the alloys; divalent metals are

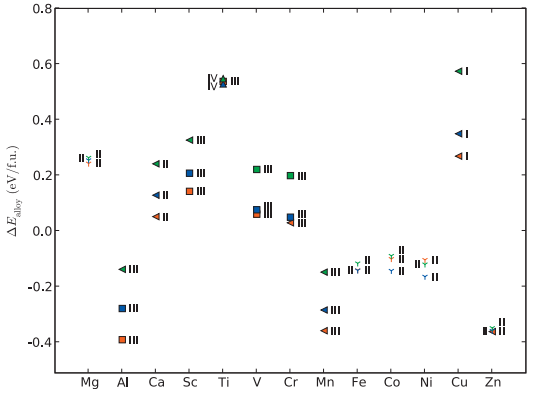


FIG. 9. The alloying energy, $\Delta E_{alloy}$, for the 3*d*-metals using only the energy of the preferred $M_1M_2(BH_4)_x$, $x=2-5$ structure. Colors: Li (red), Na (blue), and K (green). Preferred local coordination: tetra (□), octa (○), octa-tetra (△), tetra-octa (+), tetra-tri (ϒ), other (◁). The labels indicate the oxidation state of $M_2$.

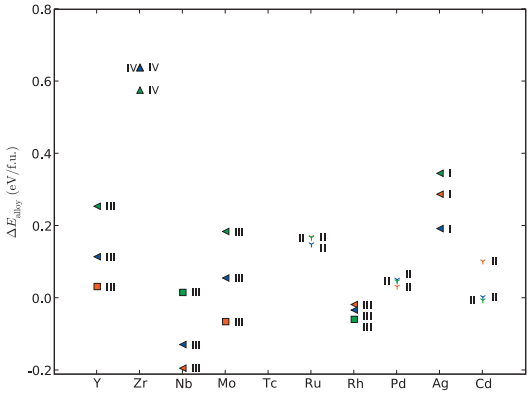


FIG. 10. The alloying energy, $\Delta E_{alloy}$, for the 4*d*-metals using only the energy of the preferred $M_1M_2(BH_4)_x$, $x=2-5$ structure. Colors: Li (red), Na (blue), and K (green). Preferred local coordination: tetra (□), octa (○), octa-tetra (△), tetra-octa (+), tetra-tri ( ᛉ ), other (◁). The labels indicate the oxidation state of $M_2$.

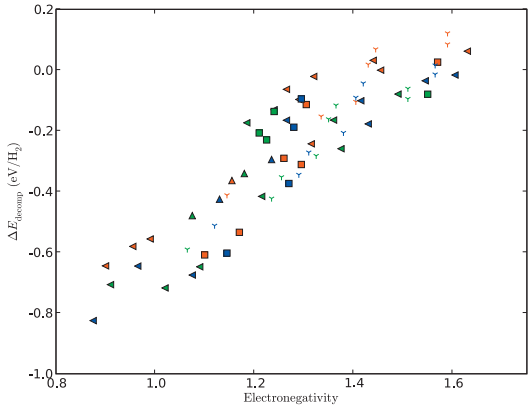


FIG. 11. The decomposition energy, $\Delta E_{decomp}$, as a function of the average Pauling electronegativity for all alloys in their preferred $M_1M_2(BH_4)_x$ coordination: tetra (□), octa (○), octa-tetra (△), tetra-octa (+), tetra-tri ( ᛉ ), other (◁). Colors: Li (red), Na (blue), and K (green).

found to prefer a $M_1M_2(BH_4)_3$ configuration, whereas trivalent metals prefer $M_1M_2(BH_4)_4$, tetravalent metals prefer $M_1M_2(BH_4)_5$ and the monovalent Cu and Ag prefer $M_1M_2(BH_4)_2$. Some deviations are found, but given the simple model structures used for both alloys and reference calculations, and given the fact that some of the metals are found by experiments to form ternary borohydrides in different oxidation states, the agreement is good.

The most stable alloys are found for the half-filled *d*-bands, but interesting alloys are also found for the empty and fully occupied *d*-bands with the addition of Al, where the $M_1Al(BH_4)_4$ are found to be promising (see Figs. 9 and 10).

Lithium-based alloys (red) are generally found to be the most stable, followed by sodium (blue) and potassium (green), although significant deviations are observed. This follows the observed trend for the storage capacities.

### B. Stability versus electronegativity

A number of recent publications[33,36] have shown an apparent linear correlation between the decomposition temperature and the average cation Pauling electronegativity. Although this might be expected, given the definition of Pauling's electronegativity, it also indicates that the kinetic barriers—if any—do not appear to be particularly system dependent.

Plotting the calculated decomposition energy as a function of the average cation electronegativity for all alloys in their most stable local coordination (see Fig. 11) appears to support this observation. The scatter of the data points around the "line" (which would have a slope that agrees with Ref. 36 to within 10%–15%) is, however, significant and deviations of $\pm 0.1$ eV/$H_2$ can be sufficient to shift a material from interesting to irrelevant for storage applications, or vice versa.

The stable alloys ($\Delta E_{alloy} \leq 0.0$ eV/f.u.) are seen to cluster around certain average electronegativities of 1.3–1.4 and 1.6 (see Fig. 12). The cluster around 1.3–1.4 is highly promising with $\Delta E_{decomp} \simeq -0.1$ eV/$H_2$ for Mn and Nb and particularly promising for Al, Zn, and Fe with $\Delta E_{decomp} \simeq -0.3$ eV/$H_2$. The Mo and Rh alloys at electronegativities around 1.6 are found to border on decomposition, but experimental work by Nikels *et al.*[33] estimates the decomposition temperature of such compounds to be around 150 °C.

## VII. CONCLUSIONS

We have analyzed the thermodynamic properties of possible alkali-transition metal borohydride systems, finding a number of candidates showing favorable properties.

The $M_1(Al/Mn/Fe)(BH_4)_4$, $(Li/Na)Zn(BH_4)_3$, and $(Na/K)(Ni/Co)(BH_4)_3$ alloys are found to be the most promising, followed by selected $M_1(Nb/Rh)(BH_4)_4$ alloys. These findings are in good agreement with experimental observations for $LiFe(BH)_3$,[37] $LiAl(BH_4)_4$,[25] $(Li/Na)Mn(BH)_{3,4}$,[38]

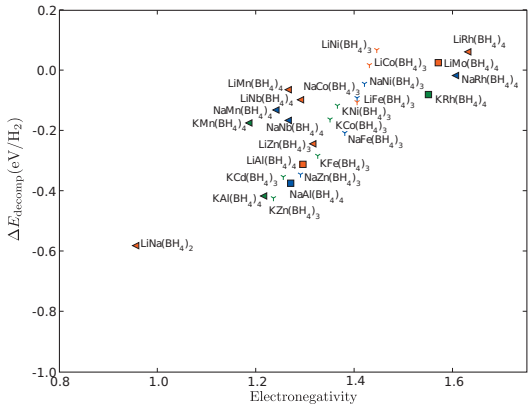


FIG. 12. The decomposition energy, $\Delta E_{decomp}$, as a function of the average Pauling electronegativity for alloys with $\Delta E_{alloy} \leq 0.0$ eV/$H_2$. Colors: Li (red), Na (blue), and K (green). Preferred $M_1M_2(BH_4)_x$, $x=2-5$, coordination: tetra (■), octa (○), octa-tetra (△), tetra-octa (+), tetra-tri ( ᛉ ), other (◁).

and $(Li/Na)Zn(BH_4)_3$,[39] whereas the Co, Cd, Nb, and Rh and alloys still remain to be synthesized and tested. Although some structures can be observed experimentally in different metal-metal stoichiometries than those used in the screening study, e.g., the Li–Zn system,[39] the alloy systems were still identified as promising candidates in this screening study. Some of the nearly stable compounds in Table III, e.g., $LiSc(BH_4)_4$ (Ref. 10) and $KNa(BH_4)_2$ (Ref. 32) have recently been found to be metastable, while $LiNi(BH_4)_3$ (Ref. 30) was found to be marginally unstable here. The LCS approach was found to limit the 757 potential alloys to 22 promising candidates of which ~10 are highly promising. These structures can now be pursued further, analyzing their detailed decomposition pathways, both theoretically[40] and experimentally.

## ACKNOWLEDGMENTS

The authors acknowledge financial support by the European Commission DG Research (Contract No. SES6-2006-51827/NESSHy), the Nordic Energy Research Council (Contract No. 06-HYDRO-C15) and the Danish Center for Scientific Computing (DCSC) for computer time (Grant No. HDW-1103-06). The Center for Atomic-Scale Materials Design is funded by the Lundbeck Foundation.

[1] L. Schlapbach and A. Züttel, Nature **414**, 353 (2001).
[2] D. Mosher, X. Tang, and S. Arsenault, DoE Hydrogen Program, FY 2006 Annual Progress Report, 2006, pp. 281–284.
[3] See http://www1.eere.energy.gov/vehiclesandfuels/about/partnerships/freedomcar/fc_goals.html for FreedomCAR and Fuel Technical Partnership Technical Goals.
[4] S. Orimo, Y. Nakamori, J. R. Eliseo, A. Züttel, and C. M. Jensen, Chem. Rev. **107**, 4111 (2007).
[5] R. Z. Sørensen, J. S. Hummelshøj, A. Klerke, J. B. Reves, T. Vegge, J. K. Nørskov, and C. H. Christensen, J. Am. Chem. Soc. **130**, 8660 (2008).
[6] A. Züttel, S. Rentsch, P. Fischer, P. Wenger, P. Sudan, P. Mauron, and C. Emmenegger, J. Alloys Compd. **356–357**, 515 (2003).
[7] Z. Łodziana and T. Vegge, Phys. Rev. Lett. **93**, 145501 (2004).
[8] Z. Łodziana and T. Vegge, Phys. Rev. Lett. **97**, 119602 (2006).
[9] K. Chłopek, C. Frommen, A. Léon, O. Zabara, and M. Fichtner, J. Mater. Chem. **17**, 3496 (2007).
[10] H. Hagemann, M. Longhini, J. W. Kaminski, T. A. Wesolowski, R. Cerný, N. Penin, M. H. Sørby, B. C. Hauback, G. Severa, and C. M. Jensen, J. Phys. Chem. A **112**, 7551 (2008).
[11] S. V. Alapati, J. K. Johnson, and D. S. Sholl, J. Phys. Chem. C **112**, 5258 (2008).
[12] V. Ozolins, E. H. Majzoub, and C. Wolverton, Phys. Rev. Lett. **100**, 135501 (2008).
[13] J. Voss, J. S. Hummelshøj, Z. Łodziana, and T. Vegge, J. Phys.: Condens. Matter **21**, 012203 (2009).
[14] P. Hohenberg and W. Kohn, Phys. Rev. **136**, B864 (1964).
[15] B. Hammer, L. B. Hansen, and J. K. Nørskov, Phys. Rev. B **59**, 7413 (1999).
[16] D. Vanderbilt, Phys. Rev. B **41**, 7892 (1990).
[17] S. R. Bahn and K. W. Jacobsen, Comput. Sci. Eng. **4**, 56 (2002).
[18] D. F. Shanno, Math. Comput. **24**, 647 (1970).
[19] F. Buchter, Z. Łodziana, A. Remhof, O. Friedrichs, A. Borgschulte, Ph. Mauron, A. Züttel, D. Sheptyakov, G. Barkhordarian, R. Bormann, K. Chłopek, M. Fichtner, M. Sørby, M. Riktor, B. Hauback, and S. Orimo, J. Phys. Chem. B **112**, 8042 (2008).
[20] See http://www.python.org for Python Programming Language.
[21] See http://subversion.tigris.org for Subversion version control system.
[22] See http://matplotlib.sourceforge.net for Matplotlib 2D plotting library for Python.
[23] J.-H. Her, M. Yousufuddin, W. Zhou, S. S. Jalisatgi, J. G. Kulleck, J. A. Zan, S.-J. Hwang, R. C. Bowman, Jr., and T. J. Udovic, Inorg. Chem. **47**, 9757 (2008).
[24] N. Hanada, K. Chłopek, C. Frommen, W. Lohstroh, and M. Fichtner, J. Mater. Chem. **18**, 2611 (2008).
[25] H.-W. Li, S. Orimo, Y. Nakamori, K. Miwa, N. Ohba, S. Towata, and A. Züttel, J. Alloys Compd. **446–447**, 315 (2007).
[26] E. Wiberg, Angew. Chem. **65**, 16 (1953).
[27] X. B. Yu, D. M. Grant, and G. S. Walker, Chem. Commun. (Cambridge) **37**, 3906 (2006).
[28] S.-J. Hwang, R. C. Bowman, Jr., J. W. Reiter, J. Rijssenbeek, G. L. Soloveichik, J.-C. Zhao, H. Kabbour, and C. C. Ahn, J. Phys. Chem. C **112**, 3164 (2008).
[29] Y. Nakamori, H.-W. Li, M. Matsuo, K. Miwa, S. Towata, and S. Orimo, J. Phys. Chem. Solids **69**, 2292 (2008).
[30] Y. Nakamori and S. Orimo, in *Solid-state Hydrogen Storage—Materials and Chemistry*, edited by G. Walker (Woodhead, Cambridge, 2008), pp. 420–449.
[31] P. Mauron, F. Buchter, O. Friedrichs, A. Remhof, M. Bielmann, C. N. Zwicky, and A. Züttel, J. Phys. Chem. B **112**, 906 (2008).
[32] L. Seballos, J. Z. Zhang, E. Ronnebro, J. L. Herberg, and E. H. Majzoub, J. Alloys Compd. **476**, 446 (2009).
[33] E. A. Nickels, M. O. Jones, W. I. F. David, S. R. Johnson, R. L. Lowton, M. Sommariva, and P. P. Edwards, Angew. Chem., Int. Ed. **47**, 2817 (2008).
[34] See http://www.docstoc.com/docs/922287/Fundamental-Studies-of-Advanced-High-Capacity-Reversible-Metal-Hydrides for "Fundamental Studies of Advanced High-Capacity, Reversible Metal Hydrides," presentation by C. M. Jensen, DOE Hydrogen Program, 13 May 2007.
[35] F. Studt, F. Abild-Pedersen, T. Bligaard, R. Z. Sørensen, C. H. Christensen, and J. K. Nørskov, Science **320**, 1320 (2008).
[36] Y. Nakamori, K. Miwa, A. Ninomiya, H. Li, N. Ohba, S. Towata, A. Züttel, and S. Orimo, Phys. Rev. B **74**, 045126 (2006).
[37] H. Nöth and P. Fritz, Angew. Chem. **73**, 408 (1961).
[38] See http://www.hydrogen.energy.gov/pdfs/review08/st_0_satyapal.pdf for "Hydrogen Storage," presentation by S. Satyapal, 2008 DOE Hydrogen Program, Merit Review and Peer Evaluation Meeting, 9 June 2008.
[39] H. Nöth, E. Wiberg, and L. Winter, Z. Anorg. Allg. Chem. **386**, 73 (1971).
[40] V. Ozolins, E. H. Majzoub, and C. Wolverton, J. Am. Chem. Soc. **131**, 230 (2009).
[41] See EPAPS Document No. E-JCPSA6-130-043923 for a listing of the authors' affiliations. For more information on EPAPS, see http://www.aip.org/pubservs/epaps.html.

# Article II

# Simple descriptors for proton-conducting perovskites from density functional theory

N. Bork and N. Bonanos
*Fuel Cells and Solid State Chemistry Division, Risø National Laboratory for Sustainable Energy, Technical University of Denmark, DK-4000 Roskilde, Denmark*

J. Rossmeisl
*Center for Atomic-scale Materials Design, Department of Physics, Technical University of Denmark, DK-2800 Kongens Lyngby, Denmark*

T. Vegge*
*Materials Research Division, Risø National Laboratory for Sustainable Energy, Technical University of Denmark, DK-4000 Roskilde, Denmark*

(Received 1 October 2009; revised manuscript received 29 April 2010; published 8 July 2010)

A series of (pseudo)cubic perovskites, $ABO_3$, have been investigated using density functional theory calculations. The structures have been optimized and thermodynamic properties and activation energies for the relevant steps of the hydrogen/proton diffusion mechanism have been calculated using the nudged elastic band path technique. We find a strong correlation between the O-H binding energy for hydrogen/proton uptake in perovskites and the energy barriers involved in the observed Grotthuss-type diffusion process. We demonstrate the possibility of estimating diffusion rates based on O-H binding energy and temperature only, without determining transition states and vibrational frequencies. We determine the binding energy providing the optimal tradeoff between occupation and diffusion rate at a given temperature, and finally we show how these correlations can be used to suggest candidate materials with improved kinetic properties for potential application as hydrogen permeable membranes and proton-conducting electrolytes.

DOI: 10.1103/PhysRevB.82.014103 PACS number(s): 66.30.jp, 71.15.Mb, 82.20.Db

## I. INTRODUCTION

The recent revival of interest in renewable energy has led to increased interest in energy technologies based on hydrogen and fuel cells. Contaminants in the hydrogen gas is an issue that needs to be dealt with since these degrade both lifetime and performance of fuel cells by active site poisoning.[1] One way of purifying the feed gas is by diffusion through a dense hydrogen separation membrane hereby producing hydrogen virtually free of contaminants. Membranes may also be applied in the separation of $CO_2$ and $H_2$ synthesized from natural gas and potentially also as electrochemical sensors.

Typical membranes applied today are based on alloys of, e.g., palladium, silver, or niobium but oxide-based ceramics, e.g., perovskites ($ABO_3$), also exhibit hydrogen/proton permeability and offer potential savings compared to typical metallic membranes.

The main obstacle for perovskite based membranes is the low diffusivity of hydrogen in any pure perovskite. It has been found that doping the perovskite with 5–25 % of a lower valence element, such as yttrium or neodymium, on the $B$ site can increase the concentration of protons in the membrane significantly and increase the hydrogen flux.[2] Even though protons in perovskites have been studied extensively, there are still considerable uncertainties and the optimal membrane composition is yet to be determined. A complete investigation of all possible combinations of perovskite, dopant and dopant concentration is however practically impossible. To address this issue, we have searched for possible correlations between hydrogen flux, protonic concentration in the material and structural properties, in order to find simple "descriptors" which can facilitate a more efficient screening of candidate materials.[3] Similar investigations have previously been performed but no decisive breakthrough has been made.

Ranløv *et al.*[4] have investigated $LnAl_{0.95}Mn_{0.05}O_{3-y}$, Ln= (Y and lanthanides) and found that the ionic radius of the Ln ion correlates with several structural and thermodynamic properties of the material. Mitsui *et al.*[5] were able to link kinetic properties for proton diffusion in perovskites to structural parameters, e.g., lattice constants. The existence of a strong correlation between prefactors and activation barriers has also been shown in the hydrogenation and dehydrogenation processes of various metals and metal hydrides.[6]

Grain boundaries, defects, and dopants create irregularities in the lattice which increase the complexity of both the thermodynamics and kinetics of the system.[7] We have therefore undertaken a theoretical study of hydrogen/proton (henceforth referred to as proton) diffusion in the undoped pseudocubic and cubic perovskites listed in Table I.[8] The complexity of the diffusion mechanism is thereby reduced due to the high-symmetry inherent in the investigated materials. In oxides and (pseudo)cubic perovskites, in particular, the possible diffusion paths are limited since the proton in all studied systems binds strongly to the lattice oxygen as shown in Fig. 1. We present results for the Grotthuss diffusional mechanism for individual protons where the host lattice distorts due to the H/OH defect but remains unchanged with respect to bonding at any time during the diffusion. This is also referred to as "free proton migration" and is considered the primary mechanism for protonic transport in oxides.[19,20] Only two distinct diffusional steps are required, namely, the transfer of a proton from one oxygen atom to another, termed

 

TABLE I. Calculated cubic unit-cell volumes compared to experimental data. † indicates that an orthorhombic structure is preferred at room temperature. $\Delta E_{\mathrm{OH\ form}}$ is the formation energy of a hydrogen defect from reaction (2).

| Perovskite | Lattice volume (Å$^3$) Calc. | Lattice volume (Å$^3$) Expt. | $\Delta E_{\mathrm{OH\ form}}$ (eV) |
|---|---|---|---|
| $BaTiO_3$ | 62.1 | 63.5[9] | 1.40 |
| $BaZrO_3$ | 73.6 | 73.0[10] | 2.15 |
| $BaNbO_3$ | 67.4 | 65.9[11] | 2.14 |
| $CaMnO_3$ | 51.1 | 51.9[12]† | −1.92 |
| $CaTiO_3$ | 57.5 | 53.6[13]† | −1.32 |
| $CaZrO_3$ | 69.4 | 64.5[14]† | −2.66 |
| $PbTiO_3$ | 62.1 | 62.6[15] | 1.32 |
| $PbZrO_3$ | 72.0 | 73.0[15] | 1.61 |
| $SrNbO_3$ | 65.5 | 65.5[16] | 1.92 |
| $SrTiO_3$ | 59.8 | 59.3[17] | 1.40 |
| $SrZrO_3$ | 72.0 | 71.5[18] | 0.69 |

"H *jump*," and the rotation of the OH bond around the oxygen atom termed "OH rot." These steps are sufficient to describe the macroscopic protonic transport.

In the theoretical approach described here, we are able to treat each diffusional process separately and deduce information of the individual processes at the atomic scale, in contrast to an experimental approach where data originating from, e.g., impedance spectroscopy or the electromotive force often reflect an average over several mechanisms and effects.[21] Atomic details can be extracted from neutron-scattering experiments[22,23] but the high cost of these, combined with time consuming data analysis, makes this technique unsuitable for screening purposes.

## II. METHODS AND COMPUTATIONAL DETAILS

The electronic-structure calculations have been performed using density functional theory (DFT) implemented in the DACAPO package[24] developed at CAMD at the Technical University of Denmark. The exchange-correlation functional used is PW91.[25] The electronic wave functions are expanded in plane wave functions with a cutoff energy of 350 eV while the electronic-density energy cutoff was 550 eV. The ion cores are described by ultrasoft pseudopotentials.[26]

Periodic boundary conditions have been used in all calculations on $(2\times2\times2)$ perovskite supercells of approximately $(8\ \text{Å})^3$ containing 40 atoms. The Brillouin zone has been sampled by a $(2\times2\times2)$ Monkhorst-Pack grid.[27] Convergence is reached when the maximum force acting on any atom drops below 0.05 eV/Å and the optimization is performed using the quasi-Newton algorithm.

The minimum-energy paths and energy barriers have been determined using the nudged elastic band (NEB) method.[28,29] Convergence criteria for the transition states are, as for optimizations, 0.05 eV/Å.

Rate constants are calculated using transition state theory in the harmonic approximation (hTST).[30] The pre-exponential is, in the harmonic approximation, given as the ratio between the products of vibrational frequencies of the initial state, $\nu_{initial}$, and the vibrational frequencies of transition state, $\nu_{TS}$.[31,32] The reaction rate is thus given as

$$k(T) = \frac{\prod \nu_{initial}}{\prod \nu_{TS}^{\ddagger}} \times \exp\left(\frac{-E_a}{k_B T}\right) \tag{1}$$

where ‡ indicates that the imaginary frequency is left out of the equation, resulting in unit of $s^{-1}$. The vibrational frequencies of both optimized and transition states are calculated using a finite-difference approximation with displacements of 0.01 Å.

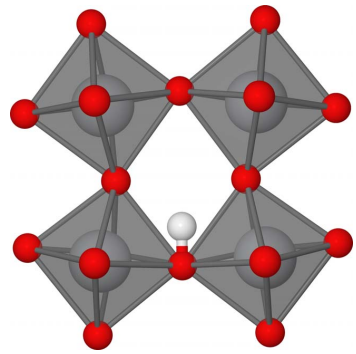

FIG. 1. (Color online) Conformation of most stable configuration of a hydrogenated $SrTiO_3$ supercell. [Sr: omitted for clarity, Ti: gray (large), O: red, and H: white.]

## III. RESULTS AND DISCUSSION

The initial unit-cell optimization was performed while enforcing cubic *P*4*mm* symmetry. The optimized cell volumes were in good agreement with experimentally obtained data, given the simplified model (see Table I). The largest deviation in lattice volumes were found in the cases of $BaNbO_3$, $CaTiO_3$, and $CaZrO_3$ with deviations of 2.3%, 7.3%, and 7.6%, respectively. It should be noted that $CaTiO_3$ and $CaZrO_3$ are found experimentally to prefer an orthorhombic structure over the cubic in the relevant temperature range.[12,13] All other deviations were below 2%. Since not all structures are perfectly cubic, the structures were internally relaxed in the optimized cubic supercells to minimize any structural inaccuracies from subsequent calculations. These reoptimized structures were used as reference states.

A hydrogen atom was then introduced in the supercell and all internal degrees of freedom were again optimized. Using a Bader charge analysis,[33] we found the local charge distribution on the proton almost identical irrespective of whether a proton or a neutral hydrogen atom is inserted. The hydrogen/proton is in both cases best described as $H^{+0.5}$;[34] and the neutral hydrogen atom was therefore chosen for all further calculations to utilize the more accurately determined energies from neutrally charged systems. The O-H distance was in all systems very close to 1.0 Å and the O-H bond

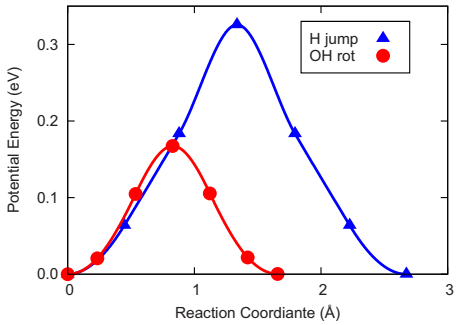


FIG. 2. (Color online) Illustration of potential energy surfaces of the minimum-energy paths linking reactant and product in the Grotthuss processes in $SrTiO_3$. Markers indicate the configurations included in the actual NEB calculations.

was in all systems perpendicular to the B-B line and pointing between the *A* cations (see Fig. 1) consistent with many previous studies, e.g., Björketun [35] The insertion of the hydrogen atom into the supercell correspond to the reaction

$$1/2H_2(g) + O_O^x \rightarrow OH_O^{a\bullet} + ae', \quad 0 \le a \le 1 \tag{2}$$

which is the first reaction of the hydrogen transport process, here in Kröger-Vink notation. $O_O^x$ denotes a structural oxygen with the "*x*" indicating neutral charge compared to normal structural oxygen. $OH_O^{a\bullet}$ denote a hydroxyl defect on an oxygen site with charge "*a*" compared to $O_O^x$ and $e'$ denotes an electron. The free-energy differences associated with this reaction will be denoted $\Delta E_{\mathrm{OH\ form}}$ and are listed in Table I.

Having located the optimal proton positions in the lattice, we were able to identify reaction pathways using the NEB method (see Sec. II) for both of the Grotthuss processes. The reaction paths were in most cases symmetrical around the transition state as demonstrated in Figs. 2 and 3. The values of the activation barriers are listed in Table II.

In order to determine the diffusional rates using hTST, we also calculated the vibrational frequencies for the optimized structures and the transition states. Since an accurate determination of vibrational frequencies is a comparatively demanding task in terms of computational expense only the atoms closest to the proton were free to move while the rest of the atoms were fixed in space. We found that including the four closest *A* ions, the two closest *B* ions and all oxygens bonded to these *B* ions was sufficient. In all cases, we found only positive frequencies for the optimized configurations while the transition states each had exactly one imaginary frequency corresponding to the reaction coordinate.

In order to compare the proton transport rate through the membrane materials, we need to determine the protonic concentration and diffusion rate constant. Here, the protonic concentration, $[OH_O]$, (charge symbol is omitted for clarity) is calculated by assuming equilibrium with gaseous hydrogen ($p_{H_2}=1$ bar) while enforcing site conservation and electroneutrality. From these standard assumptions, we obtain[36]

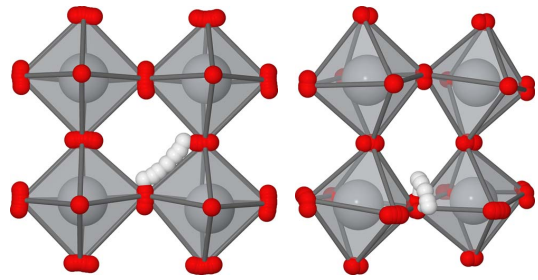

FIG. 3. (Color online) Illustration of conformational changes in $SrTiO_3$ during (a) "H jump" and (b) "OH rot" diffusional processes. Octahedra illustrate the transition state structure. [Sr: omitted for clarity, Ti: gray (large), O: red, and H: white].

$$[OH_O] = \frac{K(T)}{2}\left(\sqrt{1+\frac{4}{K(T)V}} - 1\right), \tag{3}$$

where $K(T)=\exp(-\Delta G/k_BT)$ is the equilibrium constant of reaction (2). *V* is the unit-cell volume and $\Delta G=\Delta E_{\mathrm{OH\ form}}-T\Delta S$ is the change in Gibbs free energy. The entropy of the gaseous hydrogen is determined by assuming a constant heat capacity in the temperature range of interest (500–1500 K) while the entropy of the absorbed hydrogen atom can be determined by considering the OH pairs as independent harmonic oscillators.

An effective rate constant for the two-step transport defined as

$$k_{eff}(T) = [k_{\mathrm{OH\ rot}}^{-1}(T) + k_{\mathrm{H\ jump}}^{-1}(T)]^{-1} \tag{4}$$

provides a simple way of comparing diffusional properties of the different compounds. $k_{eff}(T)$ from Eq. (4) is thus an upper bound to the true rate constants. It should be emphasized that the absolute rates obtained here are not expected to be directly comparable to experimentally obtained data due to

TABLE II. Energy barriers and pre-exponential factors for the two fundamental Grotthuss-type diffusion processes (H jump and OH rot) calculated by the NEB method.

| | Barrier (eV) | | Pre-exponential ($s^{-1}$) | |
|---|---|---|---|---|
| Perovskite | H jump | OH rot | $A_{\mathrm{H\ jump}}$ | $A_{\mathrm{OH\ rot}}$ |
| $BaTiO_3$ | 0.18 | 0.16 | $1.6\times10^{13}$ | $1.7\times10^{13}$ |
| $BaZrO_3$ | 0.27 | 0.10 | $8.9\times10^{12}$ | $9.6\times10^{12}$ |
| $BaNbO_3$ | 0.12 | 0.12 | $1.4\times10^{13}$ | $1.2\times10^{13}$ |
| $CaMnO_3$ | 1.76 | 0.32 | $1.2\times10^{15}$ | $1.4\times10^{13}$ |
| $CaTiO_3$ | 1.68 | 0.28 | $1.2\times10^{13}$ | $6.1\times10^{14}$ |
| $CaZrO_3$ | 2.51 | 0.47 | $4.9\times10^{14}$ | $3.2\times10^{13}$ |
| $PbTiO_3$ | 0.30 | 0.13 | $1.2\times10^{14}$ | $8.6\times10^{12}$ |
| $PbZrO_3$ | 0.34 | 0.13 | $1.1\times10^{13}$ | $4.0\times10^{13}$ |
| $SrNbO_3$ | 0.26 | 0.11 | $1.3\times10^{13}$ | $2.8\times10^{13}$ |
| $SrTiO_3$ | 0.33 | 0.16 | $8.0\times10^{13}$ | $7.9\times10^{12}$ |
| $SrZrO_3$ | 0.80 | 0.22 | $3.9\times10^{13}$ | $1.2\times10^{13}$ |

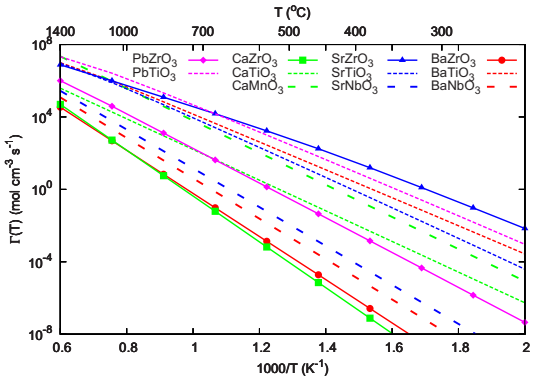


FIG. 4. (Color online) Proton transport frequency, Γ, as a function of temperature.

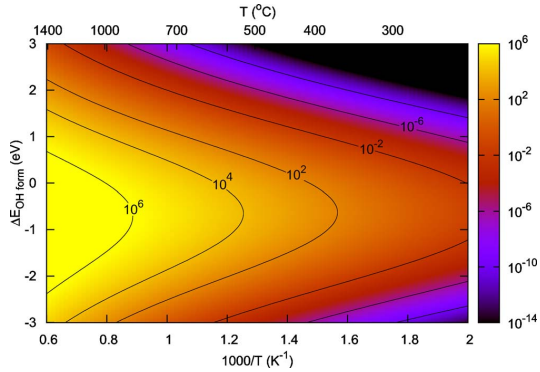


FIG. 6. (Color online) The proton transport frequency, Γ, in mol $cm^{-3}$ $s^{-1}$ as a function of temperature and $\Delta E_{\mathrm{OH\ form}}$.

the undoped and defect free nature of this model.

We note that most experimentally measurable properties such as flux, diffusivity, and resistivity scale linearly with the protonic concentration and approximately linear with the effective rate constant from Eq. (4).[30] Here we introduce the "proton transport frequency" as the product of these

$$\Gamma(T) = k_{eff}(T)[\mathrm{OH_O}] \tag{5}$$

which is proportional to the hydrogen flux. The proton transport frequencies are illustrated as a function of temperature in Fig. 4.

By initially comparing the activation energies of the two processes, we found a strong correlation. The two diffusional steps seemed hindered or favored by an underlying property of the material. We found a correlation of similar high quality between the diffusional barriers and $\Delta E_{\mathrm{OH\ form}}$; the free-energy difference of reaction (2). See Fig. 5. It is clear that a stable protonic defect implies large activation barriers for both diffusional steps.

This inverse proportionality between mobility and concentration has been found in several other studies and is an important point to emphasize. The task of optimizing the overall protonic flux through the membrane is therefore a task of finding the optimal tradeoff between mobility and concentration. This is true for both pure and doped materials. It is known that *A*-site doping can increase the protonic concentration dramatically[2,37] but dopants can also have a trapping effect on the protons and thereby lowering the mobility.[38]

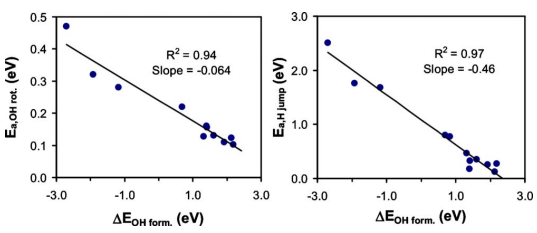


FIG. 5. (Color online) Correlations between $E_{a,\mathrm{OH\ rot}}$, $E_{a,\mathrm{H\ jump}}$, and $\Delta E_{\mathrm{OH\ form}}$.

The correlation scaling factor is quite different for the two Grotthuss processes investigated. While the OH *rot* barriers depend weakly on $\Delta E_{\mathrm{OH\ form}}$, the H *jump* barriers are strongly dependent with a ratio of approximately 0.5 eV barrier per eV $\Delta E_{\mathrm{OH\ form}}$ apparent from the slopes in Fig. 5. This can be explained by the difference in the dynamics of the processes. In the rotational process, the proton stays closely bound to the oxygen and remains "shielded" by the oxygen. It is thus expected that this activation barrier should be less sensitive to the composition of the material. The opposite can be stated for the H *jump* process. The proton has to leave the parent oxygen by breaking the OH bond from where much of the stabilization of the protonic defect stems.

It is interesting that the correlation is between these properties since it then is possible to determine the diffusion "flux" via just the thermodynamics of reaction (2), with only $T$ and $\Delta E_{\mathrm{OH\ form}}$ as variables, via the relations

$$E_{a,\mathrm{OH\ rot}} = -0.064\Delta E_{\mathrm{OH\ form}} + 0.24\ \mathrm{eV}, \tag{6}$$

$$E_{a,\mathrm{H\ jump}} = -0.46\Delta E_{\mathrm{OH\ form}} + 1.09\ \mathrm{eV} \tag{7}$$

apparent from Fig. 5. Hereby it is possible to estimate Γ as a volcano curve as a function of $\Delta E_{\mathrm{OH\ form}}$ and temperature with good accuracy. See Fig. 6.

We see that the maximum flux, for a pure and undoped material, will be found at varying values of $\Delta E_{\mathrm{OH\ form}}$ dependent on temperature, as a result of entropy. At temperatures relevant for hydrogen permeable membranes (300–800 °C), the maximum is found around $\Delta E_{\mathrm{OH\ form}} = -0.5$ eV and it is noticeable that none of the materials investigated are found in this desirable region. Even the closest materials, $SrZrO_3$ and $CaTiO_3$ with $\Delta E_{\mathrm{OH\ form}}$ of 0.69 and −1.32 eV, respectively, are far from possessing this optimal tradeoff between mobility and concentration. As can be seen from the logarithmic scale of Fig. 6, even a slight improvement in $\Delta E_{\mathrm{OH\ form}}$ could increase the flux significantly.

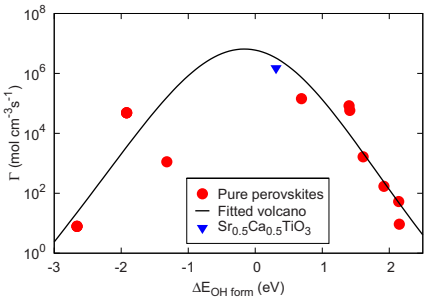


FIG. 7. (Color online) The proton transport frequency, Γ, in mol $cm^{-3}$ $s^{-1}$ as a function of $\Delta E_{\mathrm{OH\ form}}$ at 800 °C. The alloyed perovskite has more than one order of magnitude higher protonic flux than any of the pure perovskites. The compositions of the pure perovskites are listed in Table I.

A method for designing membranes based on this seem possible since we have demonstrated that the binding energy and flux are correlated. Starting from a given material, e.g., $CaTiO_3$, we now know that the main underlying problem is that the proton binds too strongly to the lattice oxygen ($\Delta E_{\mathrm{OH\ form}}=-1.32$ eV), leading to too low a protonic mobility, which is not sufficiently compensated by the increased protonic concentration. We also know that, e.g., $SrTiO_3$ has the opposite properties ($\Delta E_{\mathrm{OH\ form}}=1.40$ eV). It thus seems possible that an alloy of these materials might have the desired thermodynamic properties leading to an increased overall diffusion rate.

To test this hypothesis, we set up a cubic $(2\times2\times2)$ $Sr_{0.5}Ca_{0.5}TiO_3$ supercell as for the undoped compounds. The optimized cell constant of $(3.908\ \text{Å})^3$ differ approximately 3% from the experimentally found value.[16] Even though $Sr_{0.5}Ca_{0.5}TiO_3$ is structurally more complicated than a pure perovskite we note that all oxygens and OH bonds are equivalent when the material is assumed fully mixed. The formation energy of the protonic defect was hereafter determined to 0.31 eV comparable to the average value of the two pure compounds (approximately 0 eV). When determining the kinetic barriers we note that, as for the pure compounds, only one proton jump is found but two different OH rotations must be taken into consideration. Namely, one rotation past a Sr ion and another rotation past a Ca ion both necessary for diffusion through an entire unit cell. The energy barriers of these three processes were determined to 0.26 eV, 0.32 eV, and 0.30 eV with exponential prefactors of $5.2\times10^{12}$ $s^{-1}$, $1.9\times10^{13}$ $s^{-1}$, and $2.5\times10^{13}$ $s^{-1}$, respectively. The proton transport frequency for $Sr_{0.5}Ca_{0.5}TiO_3$ is plotted in Fig. 7 and we see that the correlations seem to hold for this compound as well. It is noteworthy that this mixed titanate is predicted to have considerably higher proton flux than any of the pure materials in the temperature range of interest—even the zirconates. The exact position of the top of the volcano is however sensitive to the limited number of data points on the left-hand side of Fig. 7 but the material is potentially very promising.

A similar approach to designing materials has already successfully been applied for several metallic catalysts[39] and since experimentally determining the best level of doping can be a highly time consuming and expensive task such correlations can help to guide the experimentalist when selecting dopants and dopant concentrations. This study reveal that it may be possible to predict optimal doping levels using correlation schemes determined by DFT.

Correlations between structural parameters, e.g., ionic radii and kinetic or thermodynamic properties are highly desirable since they could help to design materials from even simpler and more readily available data. Correlations with structural parameters of the same quality as the correlations described so far were not found but we did however find single logarithmic correlations of decent quality, $R^2=0.79$ and 0.60, between the ionic radius of the *A* ion and the barriers for H *jump.* and OH *rot.*, respectively. In both cases, we find that generally the larger *A* ion yield smaller barriers, consistent with the findings by Mitsui *et al.*[5] but this was not explored further.

## IV. CONCLUSIONS

We have investigated hydrogen/proton dynamics in a series of undoped perovskites using DFT. The preferred site for protonic defects and the reaction paths in the Grotthuss-type diffusion process have been determined. Transition states, energy barriers, and proton transport frequencies have been determined. We find a strong correlation between the barriers of diffusion and the binding energy of the proton indicating that the stronger the proton binds to the oxygen, the higher is the energy barrier for diffusion.

We thus find that the proton concentration and proton mobility are correlated properties and we deduce a direct relation between the proton transport and the binding energy. This correlation is useful for screening candidate membrane materials without performing expensive reaction path calculations; only calculating the binding energy, $\Delta E_{\mathrm{OH\ form}}$. We find no pure perovskites possessing the optimum thermodynamics and by this we also stress the importance of acceptor doping. Finally, we demonstrate the possibility of predicting membrane materials with better tradeoffs between mobility and concentration of protons in the membrane by utilizing the correlations found.

## ACKNOWLEDGMENTS

The authors would like to acknowledge the Danish Center for Scientific Computing, the Nordic Center of Excellence on Hydrogen Storage Materials, the Catalysis for Sustainable Energy (CASE) initiative and the Center of Atomic-Scale Materials Design (CAMD). CASE is funded by the Danish Ministry of Science, Technology and Innovation, and CAMD is funded by the Lundbeck foundation.

*teve@risoe.dtu.dk


[1] Y. Nagahara, S. Sugawara, and K. Shinohara, J. Power Sources **182**, 422 (2008).
[2] K. D. Kreuer, Annu. Rev. Mater. Res. **33**, 333 (2003).
[3] J. S. Hummelshøj *et al.*, J. Chem. Phys. **131**, 014101 (2009).
[4] J. Ranløv, N. Bonanos, F. W. Poulsen, and M. Mogensen, Diffus. Defect Data, Pt. B **39-40**, 219 (1994).
[5] A. Mitsui, M. Miyayama, and H. Yanagida, Solid State Ionics **22**, 213 (1987).
[6] A. Andreasen, T. Vegge, and A. S. Pedersen, J. Phys. Chem. B **109**, 3340 (2005).
[7] K. D. Kreuer, Solid State Ionics **125**, 285 (1999).
[8] All formal oxidation states are 2+ and 4+ and coordination numbers are 12 and 6 for the *A* and *B* metallic cations, respectively.
[9] I. Ahmed, S. G. Eriksson, E. Ahlberg, C. S. Knee, M. Karlsson, A. Matic, D. Engberg, and L. Boerjesson, Solid State Ionics **177**, 2357 (2006).
[10] Y. Grin, H. Mueller-Buschbaum, and H. G. von Schnering, Z. Naturforsch. Teil B **52**, 153 (1997).
[11] Q. Zhou and B. J. Kennedy, J. Phys. Chem. Solids **67**, 1595 (2006).
[12] A. T. Zayak, X. Huang, J. B. Neaton, and K. M. Rabe, Phys. Rev. B **74**, 094104 (2006).
[13] I. Levin, T. G. Amos, S. M. Bell, L. Farber, T. A. Vanderah, R. S. Roth, and B. H. Toby, J. Solid State Chem. **175**, 170 (2003).
[14] Y. Kuroiwa, Y. Terado, Kim Su Jae, A. Sawada, Y. Yamamura, S. Aoyagi, E. Nishibori, M. Sakata, and M. Takata, Jpn. J. Appl. Phys., Part 1 **44**, 7151 (2005).
[15] H. Hannerz, G. Svensson, S. Ya. Istomin, and O. G. D'yachenko, J. Solid State Chem. **147**, 421 (1999).
[16] T. Yamanaka, N. Hirai, and Y. Komatsu, Am. Mineral. **87**, 1183 (2002).
[17] B. J. Kennedy, C. J. Howard, A. K. Prodjosantoso, and B. C. Chakoumakos, Appl. Phys. A **74**, S1660 (2002).
[18] M. Hikam, B. Soegijono, and N. I. Sofyan, J. Appl. Sci. **6**, 3096 (2006).
[19] K. D. Kreuer, Chem. Mater. **8**, 610 (1996).
[20] T. Norby and P. Kofstad, Solid State Ionics **20**, 169 (1986).
[21] H. K. Bentzer, N. Bonanos, and J. W. Phair, Solid State Ionics **181**, 249 (2010).
[22] M. Karlsson, A. Matic, D. Engberg, M. E. Björketun, M. M. Koza, I. Ahmed, G. Wahnström, L. Börjesson, and S. G. Eriksson, Solid State Ionics **180**, 22 (2009).
[23] J. Voss, Q. Shi, H. S. Jacobsen, M. Zamponi, K. Lefmann, and T. Vegge, J. Phys. Chem. B **111**, 3886 (2007).
[24] DACAPO pseudopotential code, http://www.fysik.dtu.dk/campos/dacapo
[25] J. P. Perdew and Y. Wang, Phys. Rev. B **45**, 13244 (1992).
[26] D. Vanderbilt, Phys. Rev. B **41**, 7892 (1990).
[27] H. J. Monkhorst and J. D. Pack, Phys. Rev. B **13**, 5188 (1976).
[28] G. Mills, H. Jónsson, and G. Schenter, Surf. Sci. **324**, 305 (1995).
[29] H. Jónsson, G. Mills, and K. W. Jacobsen, *Classical and Quantum Dynamics in Condensed Phase Simulations* (World Scientific, Singapore, 1998).
[30] P. Hänggi, P. Talkner, and M. Borkovec, Rev. Mod. Phys. **62**, 251 (1990).
[31] T. Vegge and K. W. Jacobsen, J. Phys. Condens. Matter **14**, 2929 (2002).
[32] T. Vegge, Phys. Rev. B **70**, 035412 (2004).
[33] R. F. W. Bader, Can. J. Chem. **76**, 973 (1998).
[34] N. Bork, N. Bonanos, J. Rossmeisl, and T. Vegge (unpublished).
[35] M. Björketun, Ph.D. thesis, Chalmers University of Technology, 2007.
[36] P. Kostad, *Non-Stoichiometry, Diffusion and Electrical Conductivity in Binary Metal Oxides* (Wiley-Interscience, New York, 1972).
[37] T. Norby, M. Viderøe, R. Glöckner, and Y. Larring, Dalton Trans. **2004**, 3012.
[38] M. E. Björketun, P. G. Sundell, and G. Wahnström, Phys. Rev. B **76**, 054307 (2007).
[39] J. K. Nørskov, T. Bligaard, B. Hvolbæk, F. Abild-Pedersen, I. Chorkendorff, and C. H. Christensen, Chem. Soc. Rev. **37**, 2163 (2008).

# Article III

# Thermodynamic and kinetic properties of strongly interacting hydrogen defects in $SrTiO_3$ investigated by density functional theory

**Nicolai Bork,[a] Nikolaos Bonanos,[a] Jan Rossmeisl,[b] and Tejs Vegge*[,a,b]**

***Received Xth XXXXXXXXXX 20XX, Accepted Xth XXXXXXXXX 20XX***
***First published on the web Xth XXXXXXXXXX 200X***
**DOI: 10.1039/b000000x**

A detailed density functional theory investigation of thermodynamic and kinetic properties of hydrogen-hydrogen defect interactions in cubic $SrTiO_3$ perovskite is presented. We find a net attraction between the hydrogen atoms, with an optimal separation of $\sim 2.3$ Å. The energy gain is ca. 0.3 eV and the energy converge to that of two single hydrogen defects at separations beyond 10 Å. The cause of the net attractive potential is mainly elastic defect interactions through lattice deformaion. The Coulomb repulsion due to the identical charge on the hydrogen defects is not strong enough to push the defects apart. Two diffusion paths for the double defect are investigated and determined to be slightly faster than the corresponding diffusion paths for single hydrogen atoms. The main contributor to the total flux is identified as the double defect due to the higher concentration and mobility of this.

## 1 Introduction

Protonic defects are currently receiving much attention from several fields of science partly due to the renewed interest in hydrogen as a fuel and energy storage medium,[1] but also in recognition that protons exist in many materials and can have a significant effect on the properties of the host material. Examples include embrittlement of steel[2], band gap tuning of semiconductors[3] and switchable mirrors and solar collectors of metal-hydrides.[4,5]

It is also well known that hydrogen interact with most oxides forming mainly hydroxyl defects. In ceramic materials, e.g. perovskites or pyrochlores, the hydroxyl defect is mobile and may diffuse through the material when subjected to e.g. a pressure gradient in pressure.[6] This open the possibility for application of ceramics as gas separation membranes and fuel cell electrolytes. There are, however, several properties that needs improvement e.g. mechanical stability towards heat and pressure gradients and chemical stability towards pollutants, but most prominent is the low hydrogen flux through any known oxide.[7] A major disadvantage for the research into improving the diffusion properties of these materials is the lack of understanding of the basic mechanisms governing and limiting the diffusivity of the hydroxyl defect. Effects of grain boundaries, vacancies and surface dynamics are not well understood nor is the largely uninvestigated hydrogen-hydrogen interaction.

Hydrogen is most often introduced into oxide materials from gaseous hydrogen or water vapor through the reactions

$$H_2(g) + 2O_O^x \rightarrow 2OH_O^\bullet + 2e' \quad \text{(R1)}$$

$$H_2O(g) + v_O^{\bullet\bullet} + O_O^x \rightarrow 2OH_O^\bullet \quad \text{(R2)}$$

here presented in standard Kröger-Vink notation.[8] Even though the reaction between the gaseous and solid layer is sparsely investigated it is clear that some hydrogen-hydrogen interaction must occur in the breaking and subsequent reforming of the $H_2$ or $H_2O$ molecule.[9,10] Despite of this the literature on hydrogen defect interaction is very sparse probably caused by the general assumption that, given their mobility and charge, the hydrogen defects will repel each other and quickly diffuse apart.

C.H. Park has studied the interaction of two hydrogen defects around a lead vacancy in $PbTiO_3$ and found that the most stable configuration is with the OH bonds pointing towards each other from either side of the vacancy.[11] This study was focused on ferroelectrics and did not investigate the kinetic properties of this double hydrogen defect. Ades and Companion have found up to 5 hydrogen defects stabilized around an Al vacancy in FCC aluminum,[12] and stable configurations of multiple hydrogen defects have been found in diamond[13] and on silicon.[14]

Since understanding the fundamental mechanisms controlling the formation and mobility of hydrogen is essential in order to design novel materials with improved transport properties we have undertaken a density functional theory (DFT) investigation of a test material, $SrTiO_3$, to investigate the interaction of hydrogen defects. The theoretical approach enables

* *E-mail: tejs.vegge@risoe.dtu.dk*
[a] *Fuel Cells and Solid State Chemistry Division, Risø National Laboratory for Sustainable Energy, Technical University of Denmark, 4000 Roskilde, Denmark.*
[b] *Center for Atomic-scale Materials Design, Department of Physics, Technical University of Denmark, 2800 Kgs. Lyngby, Denmark.*

insight at the atomic level by explicitly modelling each atom which may be hard or even impossible to obtain in the laboratory. This material has been chosen since it posses several relevant properties: The perovskite structure is simple and experimentally well examined and much research is still being invested in this structure. $SrTiO_3$ does contains mobile hydrogen defects in small, but measurable concentrations[15,16] It is cubic down to 120 K, which covers all relevant application temperatures. The cubic structure is easy to handle computationally and the high symmetry of the system limits the number of configurations to investigate. Finally have numerous studies demonstrated that the material is well treated by DFT.[17–19]

We present the first extensive study of thermodynamic and kinetic properties of multiple hydrogen defects in an oxide.

## 2 Method and computational details

All calculations were performed using DFT implemented the GPAW package[20,21] combined with the Atomic Simulation Environment[22] developed at Technical University of Denmark. The GPAW package is a real space grid algorithm based on the projector augmented wavefunction method[23] with frozen core approximation.

Structure optimizations were performed following a Quasi-Newton minimization algorithm. The force convergence criteria was 0.05 eV/Å for each atom while the energy convergence criteria was $10^{-3}$ eV/atom. A symmetric gridsampling with gridspacing of 0.2 Å was used with periodic boundary conditions in all directions and a Fermi temperature of 0.1 K was used to ease convergence. Two supercells were considered; a 2×2×2 supercell containing 40 atoms and a 3×3×3 supercell containing 135 atoms. No constrainth have been enforced during the structural optimizations. The Brillouin zone was sampled using a 2×2×2 Monkhorst-Pack mesh[24] for the smaller cell while only the gamma point was sampled in the larger.

The minimum energy path (MEP) between two stable configurations was determined using the Nudged Elastic Band (NEB) method.[25,26] For accurate determination of the transition state configuration the climbing image approach was useful (cNEB).[27] The force convergence criteria was here lowered to 0.025 eV/Å.

The vibrational frequencies are calculated using a finite difference method with atomic displacements of 0.01 Å.

Rate constants are subsequently derived using transition state theory in the harmonic approximation (hTST)[28,29] given by

$$k(T) = \frac{\prod \nu_{ini}}{\prod \nu_{TS}^{\#}} \times \exp\left(\frac{-E_a}{k_B T}\right) \quad (1)$$

where $\nu_{ini}$ and $\nu_{TS}$ are the frequencies of the initial state and transition state respectively and where '#' indicate that the imaginary frequency should be omitted. This frequency ratio defines the pre-exponential factor also denoted '$A_0$'. $E_a$ is the activation energy of the reaction and $k_B$ is Boltzmann's constant.

**Table 1** *Summary of thermodynamic and kinetic properties of a single H defect in* $SrTiO_3$

| | 2×2×2 cell | 3×3×3 cell |
|---|---|---|
| $\Delta E_{OH\,form}$ | 1.72 eV | 1.63 eV |
| $E_a$ (H jump) | 0.17 eV | 0.16 eV |
| $A_0$ (H jump) | $10^{13.13}$ $s^{-1}$ | $10^{13.15}$ $s^{-1}$ |
| $E_a$ (OH rot.) | 0.33 eV | 0.33 eV |
| $A_0$ (OH rot.) | $10^{13.32}$ $s^{-1}$ | $10^{13.46}$ $s^{-1}$ |

## 3 Results and discussion

In this section will the thermodynamic and kinetic properties of hydrogen in $SrTiO_3$ be explored. Initially the perfect $SrTiO_3$ crystal is examined whereafter one and two hydrogen are introduced.

### 3.1 $SrTiO_3$ - defect free

Initially the unit cell of the perfect $SrTiO_3$ crystal was optimized. The unit cell parameter was determined to 3.931 Å in accordance with 3.905 Å found experimentally.[30] The bulk modulus was calculated to 167 GPa also in accordance with experimental values ranging from 169 to 184 with 169 GPa as the most recent.[31†] We conclude that the methods chosen are able to reproduce characteristic values for $SrTiO_3$ well.

### 3.2 $SrTiO_3$ with one H

A hydrogen atom was introduced into both of the 2×2×2 and 3×3×3 supercells corresponding to one half of reaction (R1). We found only one stable site for the hydrogen defect characterized by a O-H separation of 0.985 Å for the 2×2×2 cell and 0.981 Å for 3×3×3 cell with the hydrogen pointing directly between the Sr ions. See Fig. 1. This is the generally accepted configuration of a hydrogen defect in an undoped cubic perovskite.[6]

The formation energy of this hydrogen defect is determined to 1.72 eV in the 2×2×2 cell and 1.63 eV in the 3×3×3 cell in accordance with previous results.[32] We note that these results are without entropy contributions. We also note that the formation energy of the defect is sensitive to the cell size due to the different relative concentrations of the hydrogen defect.

† and references therein.

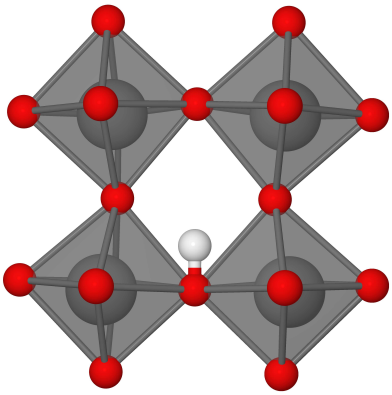

**Fig. 1** *Configuration of* $(SrTiO_3)_{27}$ *with one* $OH_O$ *defect. The corresponding structure of the smaller 2×2×2 cell is more deformed, but is otherwise similar. Oxygen (red), titanium (grey), hydrogen (white). Strontium are omitted for clarity*

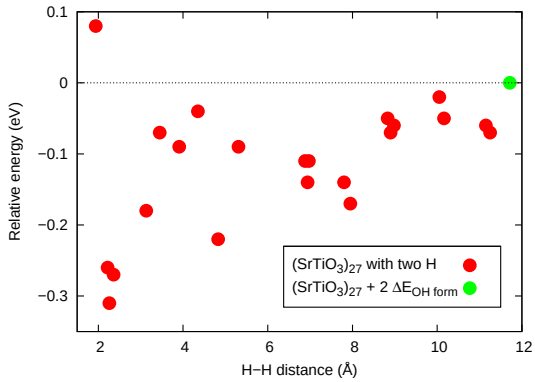


**Fig. 2** *Energy of a selection of configurations of* $(SrTiO_3)_{27}$ *with 2* $OH_O$ *defects relative to the defect free energy plus the energy of two single defects. The most stable doubly hydrogenated configuration is with ca. 2.3 Å H-H separation approximately 0.33 eV more stable than two single defects towards which the energy converge*

In a cubic and undoped perovskite only two diffusional steps are necessary to describe the full macroscopic diffusional path; a jump of a hydrogen from one oxygen to the nearest other and rotation of a hydrogen around the oxygen. The transition states of these paths were determined using NEB and the barriers and prefactors from Eq. (1) were determined (see Table 1). Due to computational expense only the hydrogen and the 7 atoms closest to the hydrogen were free to move in the calculations for the 3×3×3 cell.

We note that the kinetic properties are largely unaffected by the size of the supercell and in reasonable agreement with an overall activation barrier of 0.41 eV determined by experiment[7,16] as well as modeling studies.[33] Pre-exponentials close to $10^{13}$ Hz are also quite typical for hydrogen diffusion in perovskites.[7]

### 3.3 $SrTiO_3$ with two H

Having established the reliability of the computational methods we proceed to introduce the second hydrogen atom. Initially we attempted to determine the interaction of two hydrogen defects in a 2×2×2 supercell. A strong attractive interaction was apparent and configurations with H-H separation down to ∼ 2.5 Å were considerably stabilized, but we were unable to quantify the interaction due to the size of the cell. We therefore shifted our attention to the larger 3×3×3 supercell where much better results could be obtained.

#### 3.3.1 Thermodynamics

Due to the cubic symmetry of the material, only one stable site exist for a single hydrogen defect, but this is not the case in the doubly hydrogenated supercell. Even though many configurations are equivalent through symmetry, it is too extensive to consider all possible configurations so a selection were made. This includes all of the most stable configurations found at small H-H separation in the 2×2×2 supercell, some of the less stable configurations at medium H-H separation and finally some configurations with larger separation than possible in the 2×2×2 supercell thereby covering a large range of H-H distances. All configurations were optimized without constraints and a plot of the relative energy as function of hydrogen separation is given in Fig. 2.

These calculations verify that the most stable configurations are found at small hydrogen separation. The most stable configuration of 2 hydrogen in a 3×3×3 supercell is ca. 0.33 eV stabilized compared to two isolated defects and is illustrated in Fig. 3. This configuration is characterized by having the hydrogen defects located at the same octahedron on neighbouring oxygens with parallel OH bonds.

The energy and the H-H distance seem closely correlated and a parametrization is definitely possible. We note that a local maximum and a local minimum are found at distances at ca. 4 and ca. 8 Å. These seem to fit with the unit cell parameter (3.905 Å), but this possible effect was not explored further.

To identify the source of the attraction similar calculations were performed, but with a rigid lattice. The interaction was here purely repulsive indicating that the hydrogen themselves

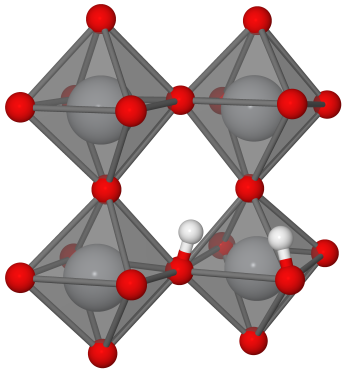

**Fig. 3** *Most stable configuration of* $(SrTiO_3)_{27}$ *with two* $OH_O$ *defects. Oxygen (red), titanium (grey), hydrogen (white). Strontium are omitted for clarity*

actually repel each other due to to their identical charges. Fitting these rigid lattice energies to a Coulomb potential we determined the effective charge on the hydrogen to ca. 0.20 *e*.§ This differ significantly from the protonic charge usually assumed, but is more in accordance with recent charge evaluations designating ca. 0.50 *e* to the OH defect.[34]

As no attractive electronic contribution is found between the hydrogen themselves we conclude that the stabilization of the closely separated hydrogens is an elastic lattice effect. Two reasons to explain the particular low energy of the configuration in Fig. 3 can be given:

1. Some lattice deformation has taken place in the immediate vicinity of the hydrogen defects, but the remaining lattice is almost perfectly cubic.

2. The lattice configuration of the single hydrogen defect creates a void in the structure where the second hydrogen can be inserted without much further lattice deformation. The energetically unfavorable lattice deformation is hereby reused.

Although defect pairing is known in several systems (REF Bjorketun m.fl.) no direct evidense of H-H pairs exist. Some insight is however avaliable through infra red spectra of hydrogenated single crystals of $SrTiO_3$. Several sepctra are avaliable and very often are several peaks around the characteristic O-H streach frequency visible.[35–37] This can not be explained by a single hydrogen defect and could be a consequence of H-H pairing.

§ 34 data points with $R^2$=0.68

### 3.3.2 Kinetics

Having justified the existence of the double hydrogen defect we proceed to the kinetic investigation. This will be performed in the 2×2×2 supercell due to the high computational effort required to determine reaction paths. We recall that the kinetic properties of one H defect were insensitive to the size of the unit cell implying that the kinetic data will provide insight into a real $SrTiO_3$ crystal with much lower defect concentration.

Many diffusional paths are possible for the double defect and in principle they all need to be investigated before anything can be concluded since every path will contribute to the total flux. A complete investigation is of course practically impossible so we focus on two paths of particular low energy. The starting and end configurations have been chosen as the most stable configuration found in the 2×2×2 supercell. The two paths are illustrated in Fig. 4.

The first path, termed "*6 step path*", is the most simple. A hydrogen moves through three elementary reactions whereafter the other follows in the exact same way. The first hydrogen jump towards the other and thereafter rotate 90° around the oxygen which it has just reached. It thereafter jump to the oxygen on the same octahedra as the "stationary" H and the configuration of Fig. 3 has been reached. The other H follows by first jumping, rotating and finally jumping so that the initial conformation is reestablished.

The second path, termed "*8 step path*", start by one hydrogen rotating away from the other **(2, 1)**, whereafter the other makes a jump **(2, 3)**, a rotation **(2, 4)** and another jump **(2, 5)** all decreasing the H-H distance. The first hydrogen rotate back to the initial position **(6, 5)** whereby the configuration in Fig. 3 is reached. The second hydrogen then rotates **(6, 7)** and jumps to the vacant oxygen opposing the first hydrogen **(6, 8)**. The first H then rotates to reach the initial configuration **(9, 8)**. The numbers in parenthesis correspond to the hydrogen positions illustrated in Fig. 4.

Energy barriers and transition states were determined using the NEB and cNEB methods without constraints as described in Section 2. In the vibrational analysis only 10 atoms closest to the defects were allowed to move due to computational expense. These were closen to capture the relevant dynamics from the full system and consisted of, besides the 2 hydrogen, 5 oxygen, 2 titanium and 1 strontium. The OH frequencies were consistent, within a few $cm^{-1}$, to two non-restricted test calculations. The activation barriers and prefactors are listed in Table 2 and the potential energy surfaces are illustrated in Fig. 5.

The barriers between 0.28 and 0.12 eV for the "*6 step path*" and between 0.31 and 0.09 eV for the "*8 step path*" are slightly lower than the corresponding barriers for single hydrogen diffusion of 0.33 and 0.17 eV. Pre-exponentials are all within 1.25 order of magnitude. The lowest, at $4 \times 10^{12} s^{-1}$, is found

*"6 step path": The starting configuration is with both hydrogens (yellow and white) furthest up of the illustrated pathways. One hydrogen diffuse the entire path, whereafter the second hydrogen follows*

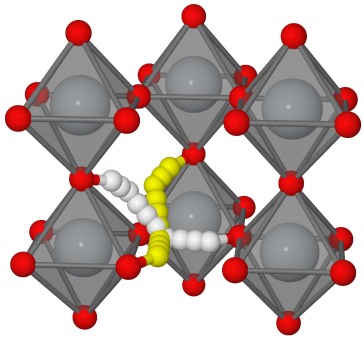

*"8 step path": The hydrogen start in positions 1 and 1. Hereafter the two hydrogens jumps and rotate such that they reach positions 2, 3, 4 and upwards to 9 where the initial configuration is reestablished*

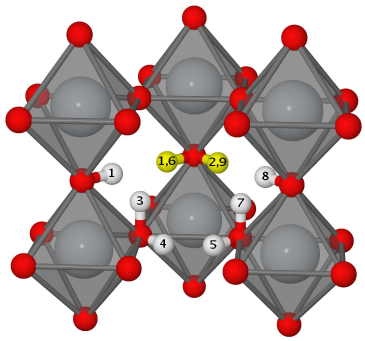


**Fig. 4** *Illustrations of the two diffusional paths under investigation. Oxygen (red), titanium (grey), hydrogen (white or yellow). Lattices are displayed unperturbed and all Strontium are omitted for clarity*

**Table 2** *Table of energies (in eV) of the configurations involved in two double hydrogen diffusional paths in* $SrTiO_3$. *The pre-exponential factor,* $A_0$ *(in* $s^{-1}$*), are calculated as in Eq.* (1)

| *"6 step path"* | Initial | TS | Final | $A_0$ |
|---|---|---|---|---|
| Step 1 | 0.00 | 0.28 | 0.16 | $10^{13.25}$ |
| Step 2 | 0.16 | 0.36 | 0.10 | $10^{12.69}$ |
| Step 3 | 0.10 | 0.26 | 0.09 | $10^{13.28}$ |
| Step 4 | 0.09 | 0.26 | 0.10 | $10^{13.82}$ |
| Step 5 | 0.10 | 0.36 | 0.16 | $10^{13.37}$ |
| Step 6 | 0.16 | 0.28 | 0.00 | $10^{12.60}$ |
| *"8 step path"* | Initial | TS | Final | $A_0$ |
| Step 1 | 0.00 | 0.23 | 0.15 | $10^{13.28}$ |
| Step 2 | 0.15 | 0.41 | 0.10 | $10^{13.04}$ |
| Step 3 | 0.10 | 0.19 | 0.09 | $10^{13.41}$ |
| Step 4 | 0.09 | 0.26 | 0.10 | $10^{13.82}$ |
| Step 5 | 0.10 | 0.19 | 0.09 | $10^{13.41}$ |
| Step 6 | 0.09 | 0.20 | 0.10 | $10^{13.82}$ |
| Step 7 | 0.10 | 0.41 | 0.15 | $10^{13.31}$ |
| Step 8 | 0.15 | 0.23 | 0.00 | $10^{13.42}$ |

for the final jump in the "*6 step path*" while the highest, at $7 \times 10^{13} s^{-1}$, is during a rotation starting from the configuration in Fig. 3 and are involved in both paths.

In order to compare the flux from these two paths to each other and to the single hydrogen diffusion path we have considered only the infinitely driven systems, i.e. neglecting random diffusion. The rate constant, $k(T)$, is thus calculated as

$$k(T)^{-1} = \sum_i k_i(T)^{-1} \sigma_i \tag{2}$$

where $k_i$ is a rate constant for an elementary process from Eq. (1) and $\sigma_i$ is a symmetry factor. The summation runs over the elementary processes of the paths; $i = 4$ for the single H diffusion, $i = 6$ for the "*6 step path*" and $i = 8$ for the "*8 step path*". This corresponds to diffusion of one hydrogen atom through one unit cell membrane or diffusion of two hydrogen through one half membrane unit cell. This yields an upper bound to the true rate constants and provide comparable results. Upper bounds to the actual diffusion rates, $r(T)$, can be calculated by

$$r(T) = k(T)[\mathrm{OH}] \tag{3}$$

where [OH] denote the concentration of the hydrogen defect. Since the hydrogen defects are formed pairwise and no evidense of repulsive ineractions have been found in this study we suggest that the double hydrogen defect is in thermal equilibrium with the single hydrogen defects. These are determined assuming also thermodynamic equilibrium of reaction

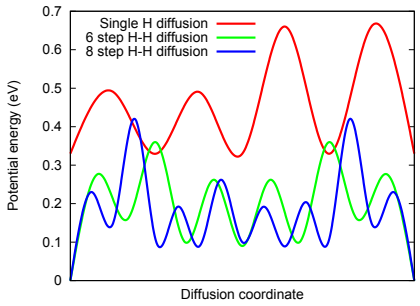


**Fig. 5** *Potential energy surfaces for the three diffusion mechanisms under consideration. The curves are splined fits to the initial and transition state energies and are to guide the eye only. The reaction coordinate corresponds is either half a lattice length for two H or a full lattice length for a single H and are thus fully comparable. The single H diffusion energies are shiftet upwards by 0.33 eV due to the relative destabilization of this compared to the double H defect.*

(R1) and electroneutrality. We obtain the equations

$$\frac{[\mathrm{OH_O}\ (double)]^2 n^2}{[\mathrm{O_O}]^2 \mathrm{pH_2}} = \exp\left(\frac{-1.63\ \mathrm{eV}}{k_B T}\right) \quad (4)$$

$$\frac{[\mathrm{OH_O}\ (single)]}{[\mathrm{OH_O}\ (double)]} = \exp\left(\frac{-0.16\ \mathrm{eV}}{k_B T}\right) \quad (5)$$

$$n = [\mathrm{OH_O}\ (single)] + [\mathrm{OH_O}\ (double)] \quad (6)$$

which are readily solved to yield the hydrogen concentrations of paired, $\mathrm{OH_O}(double)$, and isolated, $\mathrm{OH_O}(single)$, hydrogen. $n$ denote the electronic defect concentration, $[\mathrm{O_O}]$ the oxygen concentration of the material and $\mathrm{pH_2}$ the hydrogen partial pressure. Charge symbols are omitted for clarity. The rate constants and diffusion rates are plotted as function of temperature in Fig. 6.

From Fig. 6**(a)** we identify the "*6 step path*" as slightly faster than the "*8 step path*", both noticeably faster than single hydrogen diffusion. This is mainly a consequence of the barrier heights. As temperatures increase the limit of the pre-exponential factors are approached and the rate constants converge to very similar values. The rate limiting step is thus different in the low and high temperature limits. This compensation effect of high barrier implying low pre-factor and vice versa has been observed previously.[7,38]

Considering the limited size of the unit cell and the similarity of the activation barriers it is fair to state that none of the individual paths are predicted decisively faster than the others. However the total rate constant for diffusion of a double hydrogen defect will be significantly higher than the single hydrogen diffusion pathway. The total rate is given as the sum of

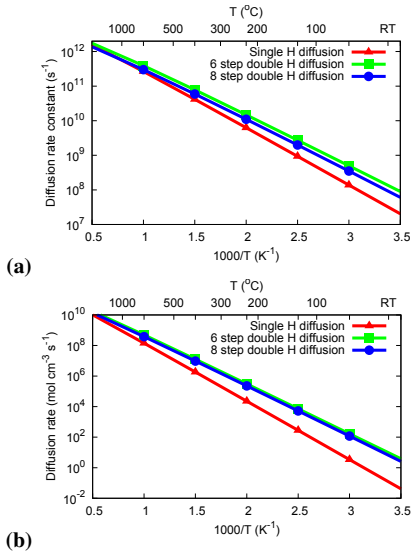


**Fig. 6** *Diffusion rate constants **(a)** and diffusion rates **(b)** for the three diffusional mechanisms under investigation as function of temperature at one bar hydrogen pressure calculated by Eq.* (2) *and* (3) *respectively*

rate constants for all the possible double defect paths, where only two have been investigated here.

Including now the relative concentrations of the defects it is clear from Fig. 6**(b)** that the double hydrogen pathway will dominate the overall flux at moderate temperatures due to the higher concentration of this defect. At high temperatures the rate of diffusion from the single defect is increasing rapidly and may possibly dominate the total flux due to the higher limiting prefactor of this process of $\sim 3\times10^{13}\mathrm{s}^{-1}$.

## 4 Conclusions

We have investigated the interaction between hydrogen defects in cubic $SrTiO_3$ perovskite. We found that two hydrogen defects stabilize each other by more than 0.3 eV. We found that this attractive interaction converge towards the expected energy at distances beyond 10 Å. Due to this long range interaction a $3\times3\times3$ supercell (135 atoms) were needed for consistent results. The interaction is primarily an elastic lattice effect and a purely repulsive H-H interaction were found in a rigid lattice.

Two possible diffusional paths of the double hydrogen defect have been investigated. These consist of low energy configurations only and will both contribute significantly to the

total hydrogen flux. The energy barriers of diffusion have been investigated and are comparable to the barriers involved in diffusion of a single hydrogen defect. The pre-exponential factors were evaluated and were also comparable to the pre-exponentials for single hydrogen diffusion.

The mobility of a single or double hydrogen defect is roughly equal implying that the double defect will dominate the net flux due to the higher concentration of this at the $500 - 800\,C$ temperature interval relevant for gas separation membranes or electrolytes in solid oxide fuel cells. At high temperatures the single hydrogen defect may dominate due to the limiting pre-exponential factors of the three paths.

Even though the double defect is stabilized compared to the single defects will configurational entropy be significant at elevated temperatures due to the low concentration of hydrogen in the material. This will favorize single hydrogen defects since two single hydrogen defects will have a low probability of meeting and recombining. In an actual working membrane at thickness down to 2,000 chemical units of perovskite[39] one should note that chemical equilibrium will not have time to settle since the acutal permeation time for a given hydrogen is on the order of a few tens of nano seconds. Since the defects are created together these will exist long enough to reach to outher side of the membrane and recombine to gaseous hydrogen.

We speculate that the stabilization of two hydrogen will be present not only in $SrTiO_3$ but in many other cubic perovskites since the prerequisites for the stabilization of such a double defect will be present namely considerably endothermic lattice deformation around a single hydrogen defect. It also seem possible that the same effect could be present in many other oxides and even in doped materials. In this study we have concentrated on the interaction of two hydrogen defects, but it is clearly interesting to include more hydrogen into the unit cell. Based on the structural knowledge we speculate that further hydrogen defects could be significantly stabilized.

## Acknowledgments

This work have been funded by Risø-DTU as part of the "Initiative for Hydrogen Separation Membranes". The authors would like to acknowledge the Danish Center for Scientific Computing for supercomputer access. The Center for Atomic Scale Material Design is supported by the Lundbeck foundation and the Catalysis for Sustainable Energy initiative is funded by the Danish Ministry of Science, Technology and Innovation.

## References

1 J. Graetz, *Chemical Society Reviews*, 2009, **38**, 73–82.
2 E. V. Monakhov, A. Yu Kuznetsov and S. B. G., *Corr. Eng.*, 2009, **58**, year.
3 T. Omura, *Corr. Eng.*, 2009, **58**, year.
4 A. Van Gogh, E. Kooij and R. Griessen, *Physical Review Letters*, 1999, **83**, 4614–4617.
5 A. Remhof and A. Borgschulte, *ChemPhysChem*, 2008, **9**, year.
6 K. Kreuer, *Annual Review of Materials Research*, 2003, **33**, 333–359.
7 K. Kreuer, *Solid State Ionics*, 1999, **125**, 285–302.
8 F. Kröger and H. Vink, *Solid State Physics*, 1956, **3**, 301 ff.
9 J. Yu, J. Lee and J. Maier, *Solid State Ionics*, 2009.
10 J. Enterkin, A. Subramanian, B. Russell, M. Castell, K. Poeppelmeier and L. Marks, *Nature Materials*, 2010, **9**, 245–248.
11 C. Park, *Ferroelectrics*, 2002, **268**, 17–22.
12 H. Ades and A. Companion, *Surface Science*, 1986, **177**, 553–564.
13 E. Lombardi, A. Mainwood and K. Osuch, *Diamond & Related Materials*, 2003, **12**, 490–494.
14 D. R. Bowler, J. H. G. Owen, K. Miki and G. A. D. Briggs, *Phys. Rev. B*, 1998, **57**, 8790–8793.
15 M. Widerøe, W. Münch, Y. Larring and T. Norby, *Solid State Ionics*, 2002, **154**, 669–677.
16 M. Widerøe, R. Waser and T. Norby, *Solid state ionics*, 2006, **177**, 1469–1476.
17 L. Marks, A. Chiaramonti, F. Tran and P. Blaha, *Surface Science*, 2009.
18 J. Padilla and D. Vanderbilt, *Arxiv preprint cond-mat/9802207*, 1998.
19 R. Evarestov, I. Tupitsyn, A. Bandura and V. Alexandrov, *International Journal of Quantum Chemistry*, 2006, **106**, year.
20 J. Mortensen, L. Hansen and K. Jacobsen, *Arxiv preprint cond-mat/0411218*, 2004.
21 *GPAW projector augmented wave algorithm, URL:www.fysik.dtu.dk/campos/gpaw/*.
22 S. Bahn and K. Jacobsen, *Computing in Science & Engineering*, 2002, 56–66.
23 P. Blochl, *Physical Review-Section B-Condensed Matter*, 1994, **50**, 17953–17979.
24 H. Monkhorst and J. Pack, *Physical Review B*, 1976, **13**, 5188–5192.
25 G. Mills, H. Jónsson and G. Schenter, *Surface Sciences*, 1995, **324**, 305 ff.
26 H. Jónsson, G. Mills and K. W. Jacobsen, *Classical and Quantum Dynamics in Condensed Phase Simulations*, World Scientific Singapore, 1998.
27 G. Henkelman, B. Uberuaga and H. Jónsson, *The Journal of Chemical Physics*, 2000, **113**, 9901.
28 P. Hänggi, P. Talkner and M. Borkovec, *Rev. Mod. Phys.*, 1990, **62**, 251–341.
29 T. Vegge, *Physical Review B*, 2004, **70**, year.
30 T. Yamanaka, N. Hirai and Y. Komatsu, *American Mineralogist*, 2002, **87**, 1183–1189.
31 J. Walsh, P. Taylor, A. Buckley, T. Darling, J. Schreuer and M. Carpenter, *Physics of the Earth and Planetary Interiors*, 2008, **167**, 110–117.
32 N. Bork, N. Bonanos, J. Rossmeisl and T. Vegge, *Submitted*.
33 W. Münch, K. Kreuer, G. Seifert and J. Majer, *Solid State Ionics*, 1999, **125**, 39–46.
34 N. Bork, N. Bonanos, J. Rossmeisl and T. Vegge, *Unpublished*.
35 J. Brebner, S. Jandl and Y. Lepine, *Physical Review[Section] B: Condensed Matter*, 1981, **23**, 3816–22.
36 S. Jandl, D. Houde, Y. Lepie and J. Brebner, *Ferroelectrics*, 1981, **38**, 805–808.
37 D. Houde, S. Jandl, P. Grenier, C. Péapin and Y. Léapine, *Ferroelectrics*, 1988, **77**, 55–68.
38 A. Andreasen, T. Vegge and A. S. Pedersen, *Journal of Physical Chemistry B*, 2005, **109**, 3340.
39 S. Rey-Mermet and P. Muralt, *Solid state ionics*, 2008, **179**, 1497–1500.

# Article IV

# The atomic structure of protons and hydrides in $Sm_{1.92}Ca_{0.08}Sn_2O_{7-\delta}$ pyrochlore from DFT calculations and FTIR spectroscopy

N. Bork[a], K.E.J. Eurenius[b], J. Rossmeisl[c], C.S. Knee[d], T. Vegge[a]

[a] *Risø National Laboratory for Sustainable Energy, Technical University of Denmark, 4000 Roskilde, Denmark*
[b] *Department of Materials Engineering, School of Engineering, University of Tokyo, 7-3-1 Hongo, Bunkyo-ku, Tokyo 113-8656, Japan*
[c] *Center for Atomic-scale Materials Design, Department of Physics, Technical University of Denmark, DK-2800 Kgs. Lyngby, Denmark*
[d] *Department of Chemistry, University of Gothenburg, SE-412 96 Göteborg, Sweden*

**Abstract**

A combined density functional theory and Fourier transform infrared spectroscopy study of the structure and specific site preference of protons and hydrides in the pyrochlore $Sm_{1.92}Ca_{0.08}Sn_2O_{7-\delta}$ is presented. Two protonic sites of particular high stability is identified, both located on O(1) oxygen atoms closely associated with a Ca dopant. Further, the finding of $H_O$ hydride defects is reported. Finally, the frequencies and relative intensities for these and other sites are calculated. All main features of the Fourier transform infrared spectra are hereby resolved.

*Keywords:* Pyrochlore, $Sm_2Sn_2O_7$, $Sm_{1.92}Ca_{0.08}Sn_2O_7$, Protonics, DFT, Density Functional Theory, FTIR, Fourier Transform Infrared Spectroscopy

*Email address:* teve@risoe.dtu.dk (T. Vegge)

## 1. Introduction

Perovskites have been at the centre of attention regarding the development of oxide based proton conducting electrolytes for many years[1, 2, 3, 4]. Acceptor doped variants of $BaCeO_3$[5] and $BaZrO_3$[6] are cheap and stable examples of simple phases which offer reasonably high proton conductivities, $\sim 10^{-3}$ S cm$^{-1}$, in the attractive intermediate temperature range.

Although extensively studied, no perovskite based material has obtained a sufficiently high protonic conductivity for commercial applications, and other structures are therefore being studied. In spite of a large number of studies relating to high temperature oxide ion migration in $A_2B_2O_7$ pyrochlore systems [7], there are relatively few studies of proton conduction at lower temperatures ($< 550$ °C) [4].

Pyrochlores can be viewed as inherently oxygen deficient flourites, but they still contain a network of apex-linked $BO_6$ octahedra that is expected to be critical for proton migration as found for perovskites[8]. The pyrochlore structure has space group Fd-3m with Wyckoff positions 16(c) and 16(d) for the $A$ and $B$ metallic cations and 48(f) and 8(b) for the two structurally inequivalent oxygen atoms denoted O(1) and O(2). The B cations are thus octahedrally coordinated by O(1) while the O(2) oxygen are tetrahedrally coordinated by A cations (See Figure 1) [8, 9].

Investigations of high temperature proton conductivity in pyrochlores have so far been focused on acceptor doped derivatives of $Ln_2B_2O_7$, where $Ln$ = lanthanide and Y, and $B$ = Zr and Ti. The original work claiming significant proton conduction in $La_2Zr_2O_7$ was performed by Shimura et al.[10]. Subsequently, infrared (IR) spectroscopy [11, 12], electrochemical

measurements[13], and quantum mechanical simulations[8] have been performed to further investigate proton mobility in the $La_2Zr_2O_7$ pyrochlore system. Recently, Fjeld et al.[14] reported on the conductivity of $Er_{1.96}Ca_{0.04}Ti_2O_{7-\delta}$ in wet oxidising conditions and found no contribution to the bulk conduction from proton charge carriers. Eurenius et. al. found bulk proton conductivity in both $Sm_{1.92}Ca_{0.08}B_2O_{7-\delta}$ and $Sm_2B_{1.92}Y_{0.08}O_{7-\delta}$, with $B$ = Ti [15] and $B$ = Sn [16] with higher proton conductivity observed for the A-site substituted (Ca-dopant) samples in both cases. These authors also studied the dependence of proton conductivity on lanthanide size in tin based pyrochlores, $Ln_{1.96}Ca_{0.04}Sn_2O_{7-\delta}$, $Ln$ = La, Sn and Yb [17].

Several basic structural properties of protons in pyrochlores are still unresolved and it is of interest to firmly establish the specific atomic configurations and protonic sites relevant for protonic diffusion. The specific protonic sites may, however, be difficult to determine experimentally using e.g. microscopy or X-rays and only few sets of neutron scattering data are available.[18, 19]

In the last decade, *ab initio* calculations have become an attractive alternative due to the rapid increase in available computational power. The explicit atomic modelling provides direct insight into atomic interactions and configurations and a wide range of properties may be calculated, e.g. atomic structures and vibrational frequencies may be determined with good accuracy[20].

In the present work, density functional theory (DFT) calculations and Fourier transform infrared spectroscopy (FTIR) data is combined to gain insight into the $Sm_{1.92}Ca_{0.08}Sn_2O_{7-\delta}$ structure at operating conditions. Us-

ing DFT, the $Ca_{Sm}$ and $V_O$ defective structure is determined and calculate the site preference for the hydrogen/deuterium defect.[1] The results are confirmed by calculating the corresponding OH stretch vibrational frequencies and comparing with experimentally obtained FTIR spectra.

## 2. Experimental

$Sm_{1.92}Ca_{0.08}Sn_2O_{7-\delta}$ was prepared via conventional solid state reactions. Hydrogenation/deuteration was achieved by exposure to 300 °C gaseous $H_2O/D_2O$ for 120 h.

The Fourier Transform Infrared (FTIR) measurements were performed in diffuse reflectance mode in the range (560  6000 $cm^{-1}$). The data was recorded with a Bruker IFS 66v/S vacuum FTIR interferometer with a KBr beam splitter and a mercury cadmium tellurium detector. The system was flushed with dry $CO_2$-free air. A reference spectrum was measured on ground KBr before collecting each sample (400 scans/run). The spectra were then derived by taking the logarithm of the ratio between the reference spectrum and the sample spectrum; for further details on the experiment, please refer to Eurenius et al.[15]

## 3. Electronic structure calculations

The calculations were performed using the VASP package using the projector augmented wave method[22, 23] with exchange and correlation functionals by Perdew, Burke and Entzerhof[24]. The Brillouin zone was sampled

[1]The Kröger-Vink notation scheme is used.[21]

using a 2x2x2 Monkhorst-Pack grid[25] and the wavefunctions were determined via plane wavefunctions up to 400 eV. The force convergence criterion was 0.01 eV/Å.

All internal degrees of freedom were relaxed during the ionic relaxations, but only the 5 closest oxygen atoms were free to move in the vibrational analysis. Since restraining a part of the system could lead to inaccuracies, a test calculation with no constrained atoms was performed. The resulting constrained and non-constrained OH vibrational frequencies differed by less than one $cm^{-1}$ confirming the validity of this approach.

For determing atomic charges, the Bader charge partitioning method is applied.[27] This has proven suitable for charge analysis of hydrogen in oxides; albeit requiring increased computational accuracy.[28] Therefore, electronic cutoffs were increased to $10^{-7}$ eV for obtaining high accuracy electronic densities via expanding the wavefunctions on 300×300×300 grids and the localized charges on 450×450×450 grids. The algorithm by Henkelman et. al. was used for the actual charge partitioning.[29, 30, 31]

## 4. Results and discussion

### *4.1. Thermodynamics*

For reference, the $V_O$ formation energy in pure $Sm_2Sn_2O_7$ was initially calculated. The unit cell parameter was first determined to be 10.531 Å in good agreement with previous experiments (10.516 Å).[15] Corresponding to the reaction

$$O_O^x \leftrightarrow 1/2\ O_2\ (g) + V_O^{\bullet\bullet} + 2\ e'. \tag{1}$$

the formation enthalpy of the oxygen vacancy was found to be 365 and 660 kJ/mol for the O(1) and O(2) sites respectively.[2] At the elevated temperatures the structure is destabilized by entropy but highly reducing conditions are required for vacancy formation in non-doped $Sm_2Sn_2O_7$.

The unit cell of $Sm_2Sn_2O_7$ contains 8 chemical units (88 atoms) so the experimentally obtained composition ($Sm_{1.92}Ca_{0.08}Sn_2O_{6.96}$) was modelled by inclusion of one $Ca_{Sm}$ dopant and the creation of an oxygen vacancy, yielding $Sm_{1.94}Ca_{0.06}Sn_2O_{6.97}$. This size cell have previously been found to be a good compromise between accuracy and computational expense.[8] Initially, the cubic unit cell constant was optimized to 10.536 Å in good agreement with previous experiments (10.514 Å) [15]. O(1) and O(2) vacancy formation energies of 225 and 385 kJ/mol via reaction (1) were found. Even though still unfavored, the formation energy of an oxygen vacancy is significantly decreased by doping and during sintering, at 1550 °C for 100 hours, oxygen vacancies are created.[15]

The most stable configuration is thus O(1) deficient as illustrated in Figure 1. At operating temperatures, this configuration is significantly more populated than any other oxygen vacant configuration and is therefore used as reference structure for the remaining of this article.[3]

[2]The reference value for molecular oxygen is associated with some uncertainty since current DFT functionals are unable correctly to describe the $^3O_2$ ground state. The expected error is on the order of 50-60 kJ per mol $O_2$ and insignificant to the relative energies and the comparison to experiments performed here.

[3]The most stable $V_{O(1)}$ site was stabilized by 16 kJ/mol compared to the second most stable $V_{O(1)}$ site.

The incorporation of a proton into the pyrochlore crystal can either be from the reaction with hydrogen and structural oxygen or through a reaction with water and an oxygen vacancy:

$$H_2(g) + 2\ O_O^x \rightarrow 2\ OH_O^\bullet + 2\ e' \tag{2}$$

$$H_2O(g) + V_O^{\bullet\bullet} + O_O^x \rightarrow 2\ OH_O^\bullet. \tag{3}$$

Initially, the first possibility was explored, albeit considering just a single OH defect. Due to the $Ca_{Sm}$ and $V_O$ defects, the symmetry of the system is low and many differnt sites are hence possible. 10 different sites were investigated and two sites of particular low energy were found. These were both bound to an oxygen atom neighbouring the vacancy but differed in the spatial orientation of the OH bond (see Figure 2). Formation energies were 21 and 30 kJ/mol H when formed via reaction (2). Hydrogen incorporation via direct reaction with hydrogen is thus not thermodynamically favorable at usual operating temperatures and pressures.

Hereafter, the incorporation of protons via reaction (3) was explored. Only two imperfections were present, but many different protonic sites are never the less available. 20 different sites were investigated and again found the most stable in the vicinity of the $Ca_{Sm}$ dopant. Two sites were significantly more stable and bonded to the same O(1) oxygen located at the former oxygen vacancy site (see Figure 3). The sites differed by the spatial orientation of the OH bond and were stabilized by ca. 137 and ca. 135 kJ/mol H when formed via reaction (3) in good agreement with experimental data of ca. 100 kJ/mol.[16] Similar energy differences were found by Björketun et al. in the case of Ca doped $La_2Zr_2O_7$ pyrochlore.[8] The exothermic nature

of reaction (3) is a direct result of the energy cost of creating the oxygen vacancy, since this energy is regained during reaction (3).

The hydrogen uptake reaction by reaction of water with an oxygen vacancy is thus highly exothermic suggesting an almost complete occupancy of the oxygen vacancies when exposed to water whereas experimental results suggest 72 % occupied vacancies[15]. The apparent discrepancy reflects kinetic limitations in the hydration and dehydration process, e.g. dissociation of $H_2O$ [33], or suggest that some of the oxygen vacancies have been occupied during the preparation of the Ca doped structure, in accordance with the endothermic nature of reaction (1). We note that both theoretical and experimental results suggest a high level of hydration.

Also the structure of hydrogenated, non-doped but oxygen deficient $Sm_2Sn_2O_7$ was determined. In the most stable structure, the proton was found not as a hydroxyl, but located at the oxygen vacancy as an $H_O$ defect (see Figure 4). To our knowledge, this defect has not previously been reported from *ab initio* studies. The defect formation energy, corresponding to the reaction

$$H_2(g) + 2\ V_O^{\bullet\bullet} + 2\ e' \rightarrow 2\ H_O^{\bullet}. \tag{4}$$

was 100 kJ/mol, favoring gaseous hydrogen and the expected $H_O$ defect concentration is thus low at ambient conditions.

### *4.2. Atomic charge distributions*

To analyse and predict possible multiple defect configurations, electrostatic defect interaction is the most importaint parameter since all present defects are electrically charged. It is generally assumed that oppositely charged defects attract while defect of similar charge repel each other. Recently, it

Table 1: *Summary of the atomic Bader charges (in e). The charges predicted by traditional defect chemistry are listed for comparison.*

| Defect structure | Figure | $Ca_{Sm}$ | $V_O$ | $OH_O$ | $H_O$ |
|---|---|---|---|---|---|
| $Ca_{Sm}V_{O(1)}$ | 1 | - 0.56 | 1.26 | - | - |
| $Ca_{Sm}V_{O(1)}OH_{O(1)}$ | 2 | - 0.59 | 1.26 | 0.55 | - |
| $Ca_{Sm}OH_{O(1)}$ | 3 | - 0.56 | - | 0.57 | - |
| Undoped $H_{O(1)}$ | 4 | - | - | - | - 0.44 |
| Trad. Def. Chem. | | - 1.00 | 2.00 | 1.00 | - 1.00 |

has however been demonstrated that elastic lattice interactions can stabilize otherwise unstable configurations.[34]

To explain the present defect structures, the most stable structures (Figures 1-4), are investigated using the Bader charge partitioning method. The results are summarized in Table 1. The determined atomic charges are not integers and smaller in magnitude than the integer charges predicted by traditional defect chemistry; the sign is however unchanged. It is known that some GGA functionals can produce artificial charge delocalization i oxides, but here, no such effect was found.

It is thus possible to assign the attractive interaction between the $Ca_{Sm}$ dopant and the $V_O$ or the $OH_O$ defect mainly to Coulomb attraction (Figures 1 and 3). Since the combined charge of the $Ca_{Sm}$ and $V_O$ defects (0.67 $e$) is similar to the $OH_O$ defect, it is not immediately apparent why the proton is attracted rather than repelled by the combined electrostatic charge on the $Ca_{Sm}$ and $V_O$ defects. The stability of two $OH_O$ defects in oxides has recently been demonstrated and explained by elastic lattice interaction,

minimizing lattice distortion by gathering defects.[34] The overall attractive force between the $Ca_{Sm}$, $V_O$ and $OH_O$ defects is proposed to be due to this effect.

Given the low stability of the $H_O$ defect under the experimental conditions, it is not relevant for the interpretation of the FTIR spectra. The $H_O$ defect has however been proposed as a possible site for hydrides in oxides and responsible for observed hydride conductivity in oxides.[35, 36, 37, 38] The apparent hydride conductivity has only been observed under highly reducing conditions at high temperatures; both conditions promoting high $V_O$ concentration and mobility. This is consistent with the $H_O$ defect being the charge carrier, but, to our knowledge, the actual charge of this defect has not been investigated previously using DFT or other *ab initio* methods.

The charge on the $H_O$ defect was determined to be -0.44 $e$ similar in magnitude to the charge designated to the "proton". We acknowlegde that this species could be termed "hydride" even though far from the full -1 charge.

### *4.3. Vibrational frequencies*

The relative intensities are assumed to be identical to the relative occupancies since the IR absorption coefficients of the relevant structures are expected to be near identical.[39]

From the experimentally obtained FTIR spectra, four distinct peaks at 3454, 3423, 3388 and 3314 $cm^{-1}$ was identified, confirming the presence of dissolved protons in the structure (see Figure 5 [15]). The three most intense peaks show clear isotopic shifts with isotopic shift ratios, $\nu_{OH}/\nu_{OD}$ $\sim$1.35, referring to the change in mass between O-H and O-D groups in accordance with the expected value.[40]

Since the vibrational frequencies depend on the second derivative of the energy these are inherently more difficult to calculate than e.g. simple energy differences and absolute agreement between DFT and FTIR results is seldom achieved. Typically, GGA functionals overestimate bond lengths and underestimate frequencies,[41] but although unable to produce accurate absolute numbers, trends and shifts are generally good.[42, 43, 44]

To quantify this problem, frequency calculations on gaseous $H_2O$ and $H_2O_2$ were performed. With the present computational parameters, the calculated OH stretch frequencies were all overestimated by 50 - 90 $cm^{-1}$ with 70 $cm^{-1}$ on average compared to experimental values.[32, 45] This suggest that the calculated OH frequencies for the present systems should be adjusted accordingly to obtain the best fit to experiment. Hereby, frequencies closely matching the main peaks of the FTIR spectrum were obtained and the adjusted frequencies are summarized in Table 2. We thus assign the two most intense peaks, at 3454 and 3314 $cm^{-1}$, to OH vibration from the H(1) and H(2) sites respectively, as illustrated in Figure 3.

Earlier studies by Omata et al.[11, 12], showing three bands in the OH frequency region in protonated $La_{1.96}Ca_{0.04}Zr_2O_{7-\delta}$, assigned one of the intense bands to protons bound to the O(2) oxygen. This based on empirical relations between O-H and O-O distances and O-H wavenumbers.[46] Our results show that a proton at the O(2) site is destabilized by 58 kJ/mol compared to the most stable $OH_{O(1)}$ site (Figure 3) in agreement with the findings of Björketun et al. for $La_2Zr_2O_7$ [8]. The $OH_{O(2)}$ defect is thus insignificantly populated at the relevant temperatures.

We were unable to identify the shoulders at 3388 and 3423 $cm^{-1}$ with

Table 2: *Calculated intensities (at 300 °C) and OH stretch frequencies (in $cm^{-1}$) of the most stable proton sites found in the undoped system, the doped system with and without an O(1) vacancy. The H(a) and H(b) sites are illustrated in Figure 2 while the H(1) to H(4) sites are as illustrated in Figure 3. The corresponding FTIR intensities and frequencies are listed for comparison.*

| Defect structure | Int.$_{DFT}$ | $\nu_{DFT}$ | Int.$_{FTIR}$ | $\nu_{FTIR}$ |
|---|---|---|---|---|
| Undoped $OH_{O(1)}$ | $\sim 0$ | 3350 | - | - |
| $Ca_{Sm}OH(1)_O$ | 73 % | 3463 | 65 - 70 % | 3454 |
| $Ca_{Sm}OH(2)_O$ | 27 % | 3322 | 30 - 35 % | 3314 |
| $Ca_{Sm}OH(3)_O$ | $< 1$ % | 3262 | - | - |
| $Ca_{Sm}OH(4)_O$ | $< 1$ % | 3331 | ($< 3$ %) | (3388) |
| $Ca_{Sm}V_OOH(a)_O$ | $\sim 0$ | 3290 | - | - |
| $Ca_{Sm}V_OOH(b)_O$ | $\sim 0$ | 4131 | - | - |

certainty, although the H(4) site in the Ca doped structure is a possible candidate (Figure 3). Otherwise, these may be attributed to structures resembling the ones investigated, but not analysed in this study or could arise from configurations involving more than two defects e.g. two Ca dopants and a proton or two protons and a Ca dopant[8, 34].

Finally, the peaks at approximately 3523 cm-1 and 2540 cm-1 (labelled with $*$ in Figure 5) are not linked to protons but are present due to the Stark effect [47]. This effect is related to ionic intraconfigurational transitions, causing a splitting in the normally degenerate f-orbitals of Sm and are energetically seen in the IR spectrum span[15].

## 5. Conclusions

Using density functional theory calculations and FTIR spectra, we investigated as-prepared and protonated $Sm_{1.92}Ca_{0.08}Sn_2O_{7-\delta}$ pyrochlore. In the most stable configuration, the $V_O$ defect was located on an O(1) site next to the $Ca_{Sm}$ dopant. Proton incorporation was investigated as a result of reaction with gaseous $H_2$ and $H_2O$, the former being endothermic while the latter exothermic in the presence of oxygen vacancies. This suggests little to no protonation via dry hydrogen while high protonation due to filling of the oxygen vacancies when exposed to water. Two protonic sites of particular low energy were found, whereby the magnitudes and intensities of the main bands of the FTIR spectrum could be reproduced with high certainty.

To explain the attractive potentials between the various defects we also determined their atomic charges. In accordance with previous results,[34] we found the $OH_O$ defect charged by ca. 0.55 $e$. We also report the finding of an $H_O$ defective oxide and determine this defect as a hydride.

## Acknowledgments

The authors thank N. Bonanos for valuable scientific discussions. The work has been supported by Stiftelsen Wilhelm and Martina Lundgrens Vetenskapsfond by providing funding to attend scientific conferences for K.E.J. Eurenius and further funded by Risø DTU as part of the "Initiative for Hydrogen Separation Membranes". C.S. Knee also acknowledges the financial support of the Swedish Research Council (Vetenskapsrådet) for this research. The Center for Atomic Scale Material Design is supported by the Lundbeck

257 foundation and the Catalysis for Sustainable Energy initiative is funded by
258 the Danish Ministry of Science, Technology and Innovation.

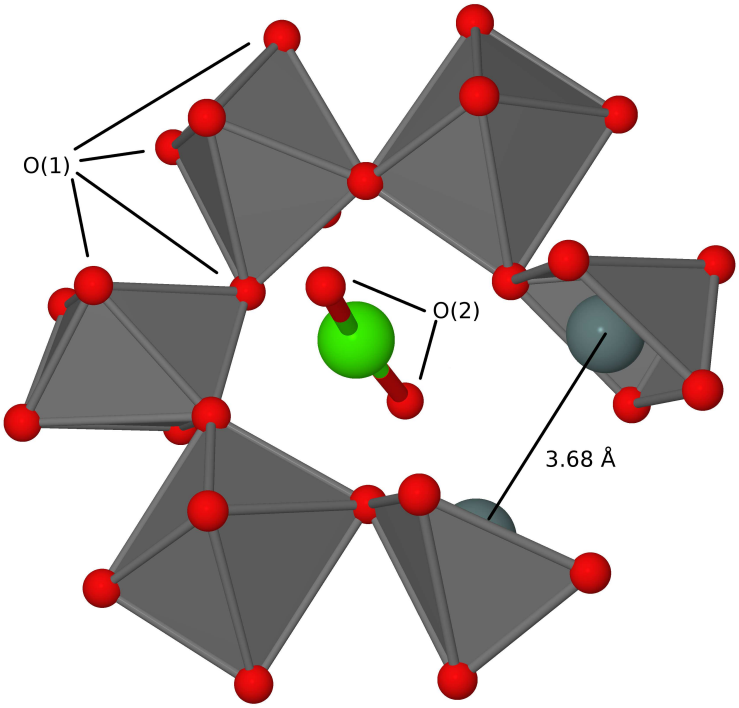


Figure 1: *Most stable configuration of the oxygen vacant* $Sm_{1.9375}Ca_{0.0625}Sn_2O_7$ *system. The structurally different O(1) and O(2) oxygen sites are indicated. The Sn-Sn distance around the oxygen vacancy is shortened to 3.68 Å compared to 3.73 Å in the defect free structure. (Sm: Omitted for clarity, Sn: Grey, inside octahedra, Ca: Green, O: Red)*

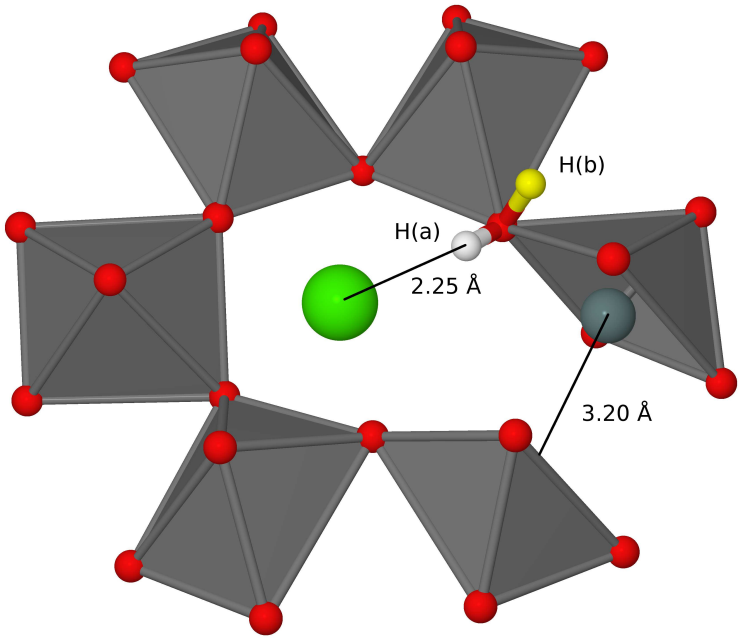


Figure 2: *Most stable configuration of a proton in the oxygen vacant* $Sm_{1.9375}Ca_{0.0625}Sn_2O_7$ *system. 4 symmetry equivalent proton sites exist, i.e. 2 on each side of the vacancy. The yellow hydrogen is included to illustrate the second most stable site. (Sm and O(2): Omitted for clarity, Sn: Inside octahedra, Ca: Green, O(1): Red, H: White and yellow)*

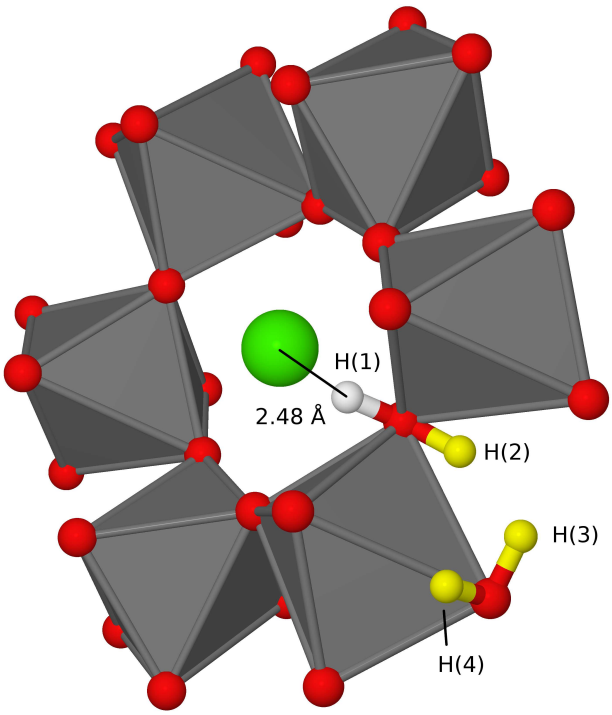


Figure 3: *Most stable configuration of a proton in* $Sm_{1.9375}Ca_{0.0625}Sn_2O_7$. *Around each Ca doipant are 12 symmetry equivalent sites i.e. 2 on each oxygen. The Ca-H distance is 2.48 Å and the Ca-O-H angle is ca. 63 °. The yellow hydrogen are included to illustrate the three second most stable sites. (Sm and O(2): Omitted for clarity, Sn: Inside octahedra, Ca: Green, O(1): Red, H: White and yellow)*

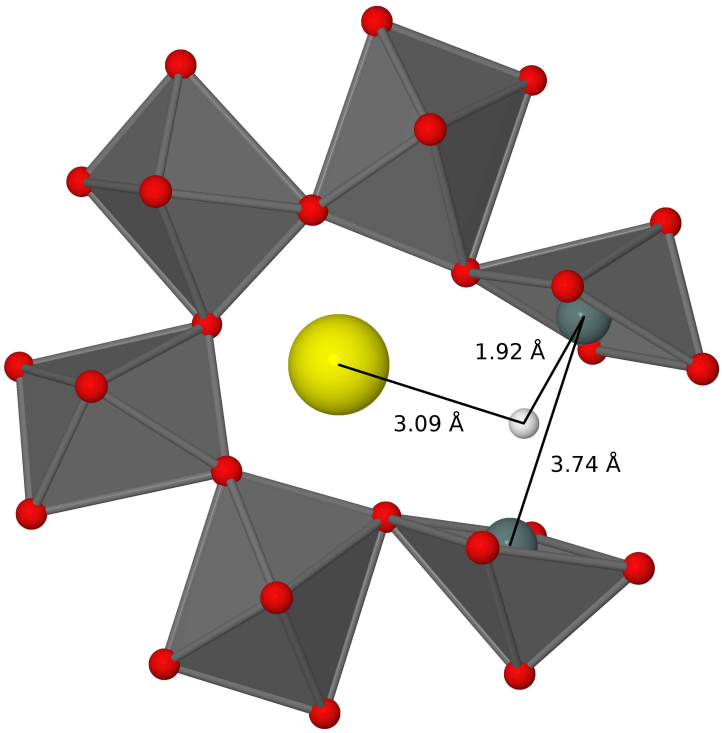


Figure 4: *Most stable configuration of a proton and an oxygen vacancy in* $Sm_2Sn_2O_7$. *The Sm-H distance is ca. 3.1 Å and the Sn-H bonds are ca. 1.9 Å in comparison with normal Sn-O distances of ca. 2.1 Å. The charge on the* $H_O$ *species is -0.44 e. (Sm: Yellow, Sn: Grey (inside octahedra), O(1): Red, O(2): Omitted for clarity, H: White)*

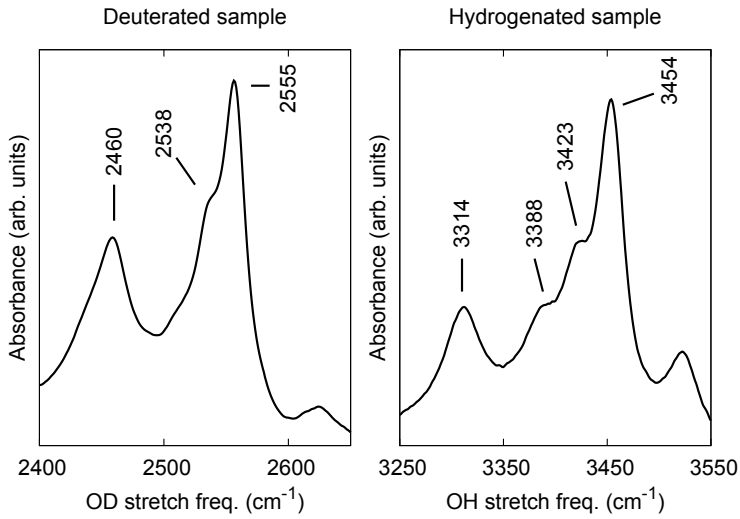


Figure 5: *Infrared absorbance spectra of* $Sm_{1.92}Ca_{0.08}Sn_2O_{7-\delta}$ *[15].* $*$ *indicate frequencies not linked to O-H/O-D vibrations. The ratios between the corresponding OH and OD frequencies are as expected close of 1.35. Data from Ref. [15].*

## References


[1] H. Iwahara, Solid State Ionics 77 (1995) 289.

[2] R.C.T. Slade, Solid State Ionics 61 (1993) 111.

[3] K.D. Kreuer, E. Schönherr, J. Maier, Solid State Ionics 70-71 (1994) 278.

[4] N. Bork, N. Bonanos, J. Rossmeisl, T. Vegge, Phys. Rev. B, 82 (2010) 014103.

[5] J.F. Liu, A.S. Nowick, Solid State Ionics 50 (1992) 131.

[6] R.B. Cervera, Y. Oyama, S. Miyoshi, K. Kobayashi, T. Yagi, S. Yamaguchi, Solid State Ionics 179 (2008) 263.

[7] S. A. Kramer, H.L. Tuller, Solid State Ionics 82 (1995) 15.

[8] M. E. Björketun, C. S. Knee, B. J. Nyman, G. Wahnström, Solid State Ionics 178 (2008) 1642.

[9] E. J. Harvey, K. R. Whittle, G. R. Lumpkin, R. I. Smith, S. A. T. Redfern, J. Solid State Chem. 178 (2005) 800.

[10] T. Shimura, M. Komori, H. Iwahara, Solid State Ionics 86-88 (1996) 685.

[11] T. Omata, M. Tagaki, S. Otsuka-Matsuo-Yao, J. Electrochem. Soc. 150 (2003) E590.

[12] T. Omata, S. Otsuka-Matsuo-Yao, J. Electrochem. Soc. 148 (2001) E475.

[13] T. Omata, S. Otsuka-Yao-Matsuo, J. Electrochem. Soc. 148 (2001) E252.

[14] H. Fjeld, R. Haugsrud, A. E. Gunnæs, T. Norby, Solid State Ionics 179 (2008) 1849.

[15] K.E.J. Eurenius, E. Ahlberg, I. Ahmed, S.G. Eriksson, C.S. Knee, Solid State Ionics 181 (2010) 148.

[16] K.E.J Euerenius, E. Ahlberg, C.S. Knee, submitted to solid state ionics, 2009.

[17] K.E.J Eurenius, E. Ahlberg, C.S. Knee, Solid State Ionics 181 (2010) 1258.

[18] M. Karlsson, A. Matic, D. Engberg, M. E. Björketun, M. M. Koza, I. Ahmed, G. Wahnström, L. Börjesson, S. G. Eriksson, Solid State Ionics 180 (2009) 22.

[19] J. Voss, Q. Shi, H. S. Jacobsen, M. Zamponi, K. Lefmann, and T. Vegge, J. Phys. Chem. B 111 (2007) 3886.

[20] F. Jensen, Inroduction to Computational Chemistry, Wiley, New York, (1999).

[21] F. Kröger and H. Vink, Solid State Phys. 3 (1956,) 301

[22] P.E. Blöchl, Phys. Rev. B 50 (1994) 17953.

[23] G. Kresse, D. Joubert, Phys. Rev. B 59 (1999) 1758.

[24] J. P. Perdew, K. Burke, M. Ernzerhof, Phys. Rev. Lett. 77 (1996) 3865.

[25] H.J. Monkhorst, J.D. Pack, Phys. Rev. B 13 (1976) 5188.

[26] B. Ruscic, R.E. Pinzon, M.L. Morton, N.K. Srinivasan, M.-C. Su, J.W. Sutherland, J.V. Michael, J. Phys. Chem. A 110 (2006) 110

[27] R.F.W. Bader, Can. J. Chem. 76 (1998) 7.

[28] N. Bork, N. Bonanos, J. Rossmeisl, and T. Vegge, Submitted (2010).

[29] G. Henkelman, A. Arnaldsson, and H. Jónsson, Comp. Mater. Sci. 36 (2006) 3.

[30] E. Sanville, S.D. Kenny, R. Smith, and G. Henkelman, J. Comput. Chem. 28 (2007) 5.

[31] W. Tang, E. Sanville, and G. Henkelman, J. Phys.-Condens. Mat. 21 (2009) 084204.

[32] J.D. Cox, D.D. Wagman, V.A. Medvedev, CODATA Key Values for Thermodynamics, Hemisphere, New York, (1989).

[33] A. Valdes, Z.W. Qu, G.J. Kroes, J. Rossmeisl, J.K. Nørskov, J. Phys. Chem. C 112 (2008) 9872.

[34] N. Bork, N. Bonanos, J. Rossmeisl, T. Vegge, Submitted (2010).

[35] M. Widerøe, N. Kochetova, and T. Norby, Dalton T. 19 (2004) 3147.

[36] M. Widerøe, R. Waser, and T. Norby, Solid State Ionics 177 (2006) 17-18.

[37] S. Steinsvik, Y. Larring, and T. Norby, Solid State Ionics 143 (2001) 103.

[38] T. Norby and Y. Larring, Solid State Ionics 139 (2000) 136.

[39] B. Andes Hess Jr., L.J. Schaad, P. Carsky, R. Zahradnik, Chem. Rev. 86 (1986) 709.

[40] M.J. Wojcik, J. Lindgren, J. Tegenfeldt, Chem. Phys. Lett. 99 (1983) 112.

[41] C. Adamo, M. Ernzerhof, G.E. Scuseria, J. Chem. Phys. 112 (2000) 2643

[42] J.O. Jensen, Spectrochim. Acta, Part A 58 (2002) 1373.

[43] R.G. Parr, W. Yang, Density Functional Theory of Atoms and Molecules, Oxford Univ. Press, Oxford (2002).

[44] M. Karlsson, A. Matic, S.F. Parker, I. Ahmed, L.Börjesson, S. Eriksson Phys. Rev. B 72 (2005) 094303

[45] T. Shimanouchi, J. Phys. Chem. Ref. Data 6 (1977) 993.

[46] A. Novak, Struct. Bonding 18 (1974) 177.

[47] G. H. Dieke, H. M. Crosswhite, Spectra and Energy Levels of Rare-earth Ions in Crystals, Interscience Publisher, N. Y. 1993

# Article V

# Ab initio Charge Analysis of Pure and Hydrogenated Perovskites

N. Bork,[1] N. Bonanos,[1] J. Rossmeisl,[2] and T. Vegge[3, a)]

[1)] *Fuel Cells and Solid State Chemistry Division, Risø National Laboratory for Sustainable Energy, Technical University of Denmark, 4000 Roskilde, Denmark*

[2)] *Center for Atomic-scale Materials Design, Department of Physics, Technical University of Denmark, 2800 Kgs. Lyngby, Denmark*

[3)] *Materials Research Division, Risø National Laboratory for Sustainable Energy, Technical University of Denmark, 4000 Roskilde, Denmark*

(Dated: 11 August 2010)

We present a density functional theory based Bader analysis on the charge distribution in pure and hydrogenated $SrTiO_3$. We find the hydrogen defect carries a +0.56 $e$ charge and the OH defect carrying a +0.50 $e$ charge compared to the host oxygen. Calculations on $BaNbO_3$, $CaTiO_3$ and $SrZrO_3$ support these findings. The distribution of the remaining electronic density decays exponentially with distance to the hydrogen defect. Diffusional paths are calculated wherein the hydrogenic species retain a charge between +0.57 and +0.54 $e$ showing that hydrogen permeation can not be viewed as consisting of virtually independent protonic and electronic transport processes.

## I. INTRODUCTION

Due to increased interest in hydrogen based technologies, the subject of protons in oxides is currently receiving much attention. The main prospects are usage of solid oxides in energy related technologies e.g. as hydrogen gas separation membranes[1] or as electrolytes in solid oxide fuel cells,[2] where significant savings may be obtained by replacing present technologies based on noble metals and noble metal alloys.

The main hindrance for any application of proton conducting oxides is the low protonic flux of any material investigated so far.[3] Depending on the material, a low protonic concentration or a low mobility of the protons may be limiting,[4] but much remains to be understood about the basic mechanisms governing the protonic and electronic transport properties.

It is usually assumed that H is incorporated in the material through reaction with gaseous $H_2$ or $H_2O$[5] e.g. through

$$H_2O(g) + 2O_O^x \rightarrow 2OH_O^\bullet + 2e' + 1/2O_2(g), \qquad (1)$$

here presented in Kröger-Vink notation, even though the actual surface reaction may be considerably more complex.[6,7] The proton is assumed to bind to a lattice oxygen, $O_O^x$, and form a hydroxyl defect, $OH_O^\bullet$, implying full dissociation of proton and electron. The electron, $e'$, is believed to transfer to the conduction band or associate with another defect.[8,9]

Hydrogenic defects in oxides are most commonly thought of as protons or hydroxides, but other charges are possible. Hydrides have been suggested e.g. in mayenite ($Ca_{12}Al_{14}O_{33}$), $SiO_2$, ZnO and MgO,[10–12] and recently has an apparent hydride conductivity been measured in several doped and undoped oxides.[13–16] Even the existence of nascent uncharged H has been suggested.[5,12]

To assist in resolving this matter, we have performed a density functional theory (DFT) study of the charge distribution and evolution during transport of hydrogen defects. We focus primarily on the $SrTiO_3$ perovskite structure as this material is known to be well treated by various DFT methods, and has been host for apparent hydride ion conductivity,[13,15] hereby making a more direct comparison of experiment and theory possible.

Determination of atomic charges is difficult since atomic charges are not observables and hence are no direct experimental data possible. Several theoretical methods are available, but the Bader charge partitioning method[17] solves many of the problems usually associated with atomic charge determination and is used exclusively in this study. See e.g. Lipkowitz and Boyd[18] for an extensive review.

## II. COMPUTATIONAL DETAILS

The electronic structure calculations were performed using the VASP package and plane augmented wavefunctions[19,20] with exchange-correlation functional by Perdew, Burke and Ernzerhof.[21] Kinetic energy cutoff for the plane waves was set to 400 eV. PBE-based functionals have been found to describe most properties of SrTiO3 well,[22] except for the band gap, which is underestimated by 1 eV. Here, the computationally more expensive non-local LDA+U calculations[23] are also performed in order to assess potential charge delocalization effects. Choosing $U_{eff}$ =8.5 eV yields a 3.2 eV band gap[24,25] in agreement with experiment.[26]

Only the gamma point was sampled in the 3×3×3 supercells (135 atoms) while a 2×2×2 Monkhorst-Pack k-point grid[27] was used for the 2×2×2 supercells (40 atoms). For structural optimizations, a $10^{-5}$ eV electronic convergence criterion and $10^{-4}$ eV/Å ionic force convergence criterion have been applied.

The Bader charge analysis was performed on single point calculations, with electronic cutoffs increased to

[a)] Electronic mail: teve@risoe.dtu.dk

TABLE I. *Average atomic Bader charges on perfect and hydrogenated $SrTiO_3$ (a.u.).*

| Supercell | Formula | Sr | Ti | O | H |
|---|---|---|---|---|---|
| 2×2×2 | $(SrTiO_3)_8$ | 1.59(7) | 1.92(7) | -1.17(5) | - |
| | $(SrTiO_3)_8H$ | 1.58(9) | 1.90(7) | -1.18(9) | 0.55(8) |
| 3×3×3 | $(SrTiO_3)_{27}$ | 1.59(6) | 1.91(7) | -1.17(1) | - |
| | $(SrTiO_3)_{27}H$ | 1.59(4) | 1.91(6) | -1.17(7) | 0.55(8) |

TABLE II. *Bader charges on H in OH in various materials (a.u.). † denote data from this study.*

| Material | $SrTiO_3$ | $BaNbO_3$ | $CaTiO_3$ | $SrZrO_3$ |
|---|---|---|---|---|
| Charge on H | 0.56† | 0.54† | 0.57† | 0.60† |
| Material | $H_2O$ | $H_2O_2$ | HCOOH | $CH_3COOH$ |
| Charge on H | 0.567[28] | 0.547[29] | 0.580[36] | 0.579[36] |

$10^{-7}$ eV, on already optimized structures. The algorithm by Henkelman et. al. was used for the actual charge partitioning[28–30]. The wavefunctions were expanded on a 300×300×300 grid and the localized charges on a 450×450×450 grid.

Reaction paths were determined using the climbing image-Nudged Elastic Band method (NEB).[31–33]

## III. RESULTS AND DISCUSSION

The unit cell lattice constant was determined to be 3.926 Å in good agreement with the 3.905 Å obtained experimentally.[34]

The Bader charges were hereafter calculated for both 2×2×2 and 3×3×3 supercells to determine the sensitivity towards the varying computational parameters (k-points and grid). See TABLE I. Even though small changes are apparent, the consistency is satisfactory, implying that the results in either system will be descriptive of the other. We conclude that the atomic charges in cubic $SrTiO_3$ are best describes as $Sr^{1.60}$, $Ti^{1.92}$ and $O^{-1.17}$. LDA+U calculations confirmed these charges to within a few percent.

A neutral hydrogen atom was hereafter introduced into both the 2×2×2 and 3×3×3 supercells. The large unit cell is more in accordance with a real crystal due to the expected low H concentration,[4] but NEB calculations become too expensive in this size cell. It has however been demonstrated that the errors in performing NEB in the 2×2×2 supercell are small.[35]

The average charges of these systems are listed in TABLE I. We see that the H is carrying ca. + 0.56 $e$ charge regardless of being in a small or large unit cell, confirming that the charges determined in one system is descriptive of the other. Inserting a proton only (and a compensating homogeneous negative background charge), instead of both proton and electron, did not change the charges significantly ($< 1.5$ %). LDA+U calculations differed negligibly.

To clarify whether the 0.56 $e$ charge on the hydrogen atom in $SrTiO_3$ is a typical value in perovskite systems, three other perovskites were investigated. $BaNbO_3$, $CaTiO_3$ and $SrZrO_3$ were chosen since they frequently are mentioned as candidates for proton or hydrogen conducting membranes.[37–39] 2×2×2 supercells were considered based on experimentally obtained unit cells and geometries.[40–42] The Bader charges were determined and the resulting hydrogen charges are displayed in TABLE II. Considering also the OH containing molecules it is clear that the charge on H is primarily determined by the bond to the oxygen and much less by the other atoms in the material and that the typical H charge is 0.54 - 0.60 $e$.

It is clear that upon incorporation of 1/2 $H_2$ into the $SrTiO_3$ crystal, a full electron must be accounted for. Since H in itself only accounts for 44 % of the electron density, the rest must be associated with other atoms. The oxygen bound to the hydrogen is the main carrier of the missing charge. The charge of this oxygen is increased from -1.17 to -1.23. The hydroxyl species is thus formally written $OH_O^{0.50\bullet}$ and the formation of the defect occur through

$$H_2O(g) + 2O_O^x \rightarrow 2OH_O^{0.50\bullet} + e^- + 1/2O_2(g). \qquad (2)$$

Comparing this to reaction (1) we see that the main difference is the number of electrons formed.

Searching for the remaining 0.50 electron, a general increase in electronic density with decreasing distance to the hydrogen was noticeable, but large variations were found as a consequence of lattice deformation shielding or exposing a given atom to the proton and hence extra charge. These effects are real and will be present in a real material, but in order to illuminate further on the distribution of the remaining charge, we performed similar calculations without relaxing the lattice upon insertion of the H atom. The Bader charge analysis on this undistorted cubic system showed that the increased electronic charge decays exponentially with distance to H as illustrated in FIG. 1. Not until ca. 8 Å have all charges converged.

We conclude that half the electron induced by the hydrogen is directly associated with the hydroxyl defect. The remaining electronic density is not evenly smeared, but decrease with distance to the H defect. The decrease can be viewed as an exponential decay from the hydrogen perturbed by a lattice distortion. While only the 2 closest Sr atoms are noticeably affected by the extra charge, the Ti and O atoms are affected at distances up to ca. 8 Å.

It is generally assumed that the proton diffuses via the Grotthuss mechanism wherein proton diffusion consist of H jumps and OH reorientations.[43,44] These were both investigated using the NEB algorithm (see FIG. 2). The barriers were found to be consistent with previous studies at 0.16 and 0.28 eV for the rotation and jump respectively.[4] A charge analysis was hereafter conducted

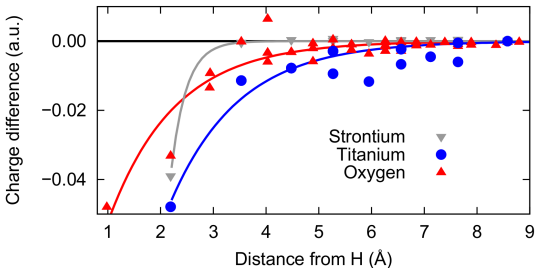


FIG. 1. *Change of charge on Sr, Ti and O atoms from perfect to singly hydrogenated undistorted cubic 3×3×3 $SrTiO_3$. Lines are fitted exponentials. Same trends are apparent in the relaxed system, but with larger scattering.*

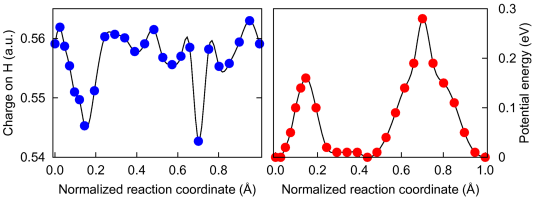


FIG. 2. *Charge and energy profile of a diffusing hydrogen in $SrTiO_3$. Diffusion is modeled as an OH rotation followed by a H jump.*

on all intermediate configurations to follow the charge during diffusion.

The 0.56 equilibrium charge is, at the transition states only reduced to ca. 0.54 regardless of the mechanism, i.e. the H charge is virtually constant, even during jumps between different oxygen atoms. During an OH rotation, the charge dependence is smooth, while the charge dependence during H jump is more abrupt. This is caused by geometrical changes during the reactions. While the OH distance slowly decreases until the transition state is reached during a rotation, the shortest OH distance of the jump increases more abruptly exactly when the H is being transferred from one O to another. From these results it is evident that the hydrogen defect remains partially charged during the dynamical transport processes. LDA+U calculations were also performed on the transition states, but did not yield significantly different results.

FIG. 3 shows the change in electronic density imposed by a proton diffusing one perovskite unit cell length, corresponding to two OH rotations and two H jumps, in a 3×3×3 supercell. For clarity, the lattice has been kept fixed. As the proton moves from left to right it is clear that electronic density disappear at the former protonic site and appear at the new protonic site. It is also obvious that the changes in electron density on the remaining atoms strongly depend on the distance to the H

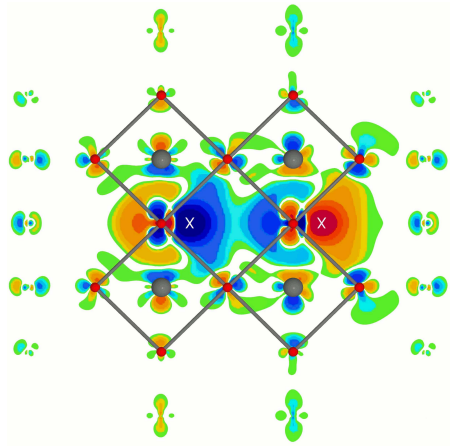


FIG. 3. *Change in electronic densities from a proton diffusing one perovskite unit cell (left to right) through a rigid lattice in a 3×3×3 supercell. The proton positions are indicated by "X". The nearest oxygen atoms (red spheres) and titanium atoms (grey spheres) are indicated.*

atom. This is consistent with the results from FIG. 1. Combined with FIG. 2 this signifies that the "protonic" transport effectively carries a near neutral, but partially delocalized charge. The electronic and protonic conductivities should therefore not be considered as separate properties.

## IV. CONCLUSIONS

We have investigated hydrogen charges in $SrTiO_3$ using the Bader charge analysis method based on density functional theory electronic structure calculations. We determine the hydrogen charge to ca. 0.56 $e$, but best described as $OH_O^{0.50\bullet}$ due to increased charge on the host oxygen atom. These H charges are in agreement with results from other perovskites and in molecular systems, and we conclude that the OH bond is the main descriptor for H charge.

The remaining half of the electron is not evenly smeared on the surrounding atoms, but distributed mainly on the oxygen and titanium and decaying exponentially from the hydrogen. Variations caused by lattice deformation are however significant.

The diffusional paths of a Grotthuss diffusional mechanism have been determined and the charge development during the diffusion has been investigated. We find the charge decreasing ca. 0.015 $e$ (2-3 %) at the transition states for both H jumps and OH reorientations. We conclude that hydrogen permeation in this model perovskite should not be viewed simply as decoupled protonic and electronic conductivities, since the hydrogen defect carries a semi-localized net charge close to neutral.

## ACKNOWLEDGMENTS

This work have been funded by Risø DTU as part of the "Initiative for Hydrogen Separation Membranes". The authors would like to acknowledge the Danish Center for Scientific Computing for supercomputer access. The Center for Atomic Scale Material Design is supported by the Lundbeck foundation and the Catalysis for Sustainable Energy initiative is funded by the Danish Ministry of Science, Technology and Innovation.

[1]S.C.A. Kluiters, *Energy Center of the Netherlands, Petten, The Netherlands*, (2004).
[2]K.D. Kreuer, S.J. Paddison, E. Spohr, and M. Schuster, *Chem. Rev* **104**, 10 (2004).
[3]K.D. Kreuer, *Ann. Rev. Mater. Res.* **33**, 333 (2003).
[4]N. Bork, N. Bonanos, J. Rossmeisl, and T. Vegge, *unpublished*.
[5]T. Norby, M. Viderøe, R. Glöckner, and Y. Larring, *Dalton T.* p. 3012 (2004).
[6]J.-H. Yu, J.-S. Lee, J. Maier, *Solid State Ionics* **181**, (2010).
[7]J.A. Enterkin, A.K. Subramanian, B.C. Russell, M.R. Castell,K.R. Poeppelmeier, L.D. Marks, *Nat. Mater.* **9** (2010)
[8]P.G. Sundell, M.E. Björketun, and G.Wahnström, *Phys. Rev. B* **73**, 10 (2006).
[9]M.E. Björketun, P.G. Sundell, and G. Wahnström, *Faraday Discuss.* **134**, (2007).
[10]K. Hayashi, M. Hirano, and H. Hosono, *B. Chem. Soc. Jpn.* **80**, 5 (2007).
[11]A. Yokozawa and Y. Miyamoto, *Phys. Rev. B* **55**, 20 (1997).
[12]C.G. Van de Walle, *J. Alloy. Compd.* **446**, 48 (2007).
[13]M. Widerøe, N. Kochetova, and T. Norby, *Dalton T.* **19**, 3147 (2004).
[14]M. Widerøe, R. Waser, and T. Norby, *Solid State Ionics* **177**, 17-18 (2006).
[15]S. Steinsvik, Y. Larring, and T. Norby, *Solid State Ionics*, **143**, 103 (2001).
[16]T. Norby and Y. Larring, *Solid State Ionics*, **136-137**, 139 (2000).
[17]R.F.W. Bader, *Can. J. Chem.* **76**, 7 (1998).
[18]K.B. Lipkowitz and D.B. Boyd, VCH Publishers, Inc., (1994).
[19]P.E. Blochl, *Phys. Rev. B* **50**, 24 (1994).
[20]G. Kresse and D. Joubert, *Phys. Rev. B* **59**, 1758 (1999).
[21]J.P. Perdew, K. Burke, and M. Ernzerhof, *Phys. Rev. Lett.* **77**, 3865 (1996).
[22]R. Wahl, D. Vogtenhuber, and G. Kresse, *Phys. Rev. B* **78**, 104116 (2008).
[23]S.L. Dudarev, G.A. Botton, S.Y. Savrasov, C.J. Humphreys, and A.P. Sutton *Phys. Rev. B* **57**, 1505 (1998).
[24]J. Lee and A.A. Demkov *Phys. Rev. B* **78**, 193104 (2008).
[25]M.S. Kim and C.H. Park *J. Korean Phys. Soc.*, **56** 490 (2010)
[26]K. van Benthem, C. Elsasser and R. H. French, *J. Appl. Phys.* **90**, 6156 (2001).
[27]H.J. Monkhorst and J.D. Pack, *Phys. Rev. B* **13**, 5188 (1976).
[28]G. Henkelman, A. Arnaldsson, and H. Jónsson, *Comp. Mater. Sci.* **36**, 3 (2006).
[29]E. Sanville, S.D. Kenny, R. Smith, and G. Henkelman, *J. Comput. Chem.* **28**, 5 (2007).
[30]W. Tang, E. Sanville, and G. Henkelman, *J. Phys.-Condens. Mat.* **21**, 084204 (2009).
[31]G. Mills, H. Jónsson, and G. Schenter, *Surf. Sci.* **324**, 305 (1995).
[32]H. Jónsson, G. Mills, and K. W. Jacobsen, World Scientific Singapore, (1998).
[33]G. Henkelman, B.P. Uberuaga, and H. Jónsson, *J. Chem. Phys.* **113**, 9901 (2000).
[34]T. Yamanaka, N. Hirai, and Y. Komatsu, *Am. Mineral.* **87**, 1183 (2002).
[35]N. Bork, N. Bonanos, J. Rossmeisl, and T. Vegge, *unpublished*.
[36]F. De Proft, C. Van Alsenoy, A. Peeters, W. Langenaeker, and P. Geerlings, *J. Comput. Chem.* **23**, 12 (2002).
[37]M. Zhang, C. Hu, H. Liu, Y. Xiong, and Z. Zhang, *Sensor Actuat. B- Chem.* **136**, 1 (2009).
[38]W. Münch, K.D. Kreuer, G. Seifert, and J. Majer, *Solid State Ionics* **125**, 1-4 (1999).
[39]K.D. Kreuer, S. Adams, W. Münch, A. Fuchs, U. Klock, and J. Maier, *Solid State Ionics* **145**, 1-4 (2001).
[40]Y. Grin, H. Mueller-Buschbaum, and H.G. Von Schnering, *Z. Naturforsch. Pt. B* 153 (1997).
[41]M. Ahtee, A.M. Glazer, and A.W. Hewat, *Acta Crystall. B-Stru.* **34**, 3 (1978).
[42]T. Barth, *Norsk Geol. Tidsskr.* **8**, 201 (1925).
[43]T. Norby and P. Kofstad, *Solid State Ionics* **20**, 169 (1986).
[44]K.D. Kreuer, *Chem. Mater.* **8**, 610 (1996).